Emil Josef Parth, Bsc

Angle-resolved Photoemission of Molecules and Two-dimensional Materials from a Tight-binding Perspective

Master's Thesis

Supervisor
Puschnig Peter, Assoz.-Prof., Dipl.-Ing., Dr. rer. nat

Institute of Physics
University of Graz

September 2021

Abstract

Angle-resolved photoemission spectroscopy (ARPES) offers the most direct access to investigate the electronic bandstructure of surfaces and solids. Nevertheless, the interpretation of ARPES data is often a complex task and simulations of bandstructures and ARPES intensity distributions are desirable. With the knowledge of the electronic eigenstates of a given system, it is possible to make predictions of the corresponding intensity distribution of an ARPES experiment. This can be achieved within the so called one-step model of photoemission which describes the photoexcitation from an initial state to a final, unbound state as a single coherent process. Thus, the photoemission matrix element not only depends on the initial and final state, but additionally on the polarization of the incident light beam. In this work, we focus on the differences in the angular distribution of the photoemission intensity arising from excitation with right and left handed circularly polarized light, respectively. This effect is referred to as circular dichroism in the angular distribution (CDAD)[1].

A common [2; 3] way of evaluating the photoemission matrix element appearing in the one-step model, if the final state is approximated as a plane wave, is the so called velocity gauge, which can be interpreted as Fourier transform of the initial state. Within this formalism the CDAD vanishes.

Another way of evaluating the photoemission matrix element is the so called length-gauge. Here, the interaction Hamiltonian in the matrix element contains the position operator in place of the momentum operator in the velocity gauge. By specializing on planar hydrocarbons a general analytic expression of the photoemission matrix element and its polarization dependence is found. To this end, a tight-binding (TB) model, based on density functional theory (DFT) results, is constructed in order to calculate the electronic eigenstates of any planar hydrocarbon systems. This way a method to calculate the ARPES intensity distribution for arbitrary planar hydrocarbon molecules is derived. Using this model, the photoemission matrix element in length-gauge predicts a non-vanishing CDAD.

As an alternative and potentially more accurate approach to simulate ARPES intensity maps, also time-dependent density functional theory (TDDFT) calculations are performed. We utilize the so-called surface flux method, which produces ARPES intensities without the need to approximate the final state, and which serves as an ideal reference for benchmarking the TB-model. When comparing ARPES simulations of the TDDFT and the TB-model for graphene, significant differences in the CDAD intensity distributions are observed.
Finally, we also compare experimental photoemission momentum maps for the organic molecule tetracene [4] with the momentum maps obtained by the TB-model and observe reasonable agreement. Whether the evaluation of the matrix element in the length-gauge shows the correct CDAD effect for molecular systems in general, however is not evaluated and further testing is needed.

Kurzzusammenfassung

Winkelaufgelöste Photoemissionsspektroskopie (ARPES) ist eine Methode, um die elektronische Bandstruktur einer Oberfläche oder eines Festkörpers möglichst detailliert zu untersuchen. Die Interpretation der Ergebnisse von ARPES Experimenten ist oft schwierig, weshalb Simulationen von Bandstrukturen und ARPES Intensitäten hilfreich sind. Bei Kenntnis der elektronischen Eigenzustände des Systems ist es möglich, Vorhersagen zur Intentsitätsverteilung des ARPES Experiments zu treffen. Dies ist mit Hilfe des sogenannten ”one-step model” der Photoemission möglich. Darin wird die Photoemission als ein Übergang von einem Anfangs- in einen freien Endzustand, durch einen kohärenten Prozess beschrieben. Das Photoemissionsmatrixelement hängt, neben dem Anfangs- und Endzustand, auch von der Polarisationsrichtung des einfallenden Lichtstrahls ab. Diese Arbeit beschäftigt sich vor allem mit den unterschiedlichen Ergebnissen der Intensitätsverteilung des Photoemissionsmatrixelement für links und rechts händig zirkular polarisiertes Licht. Dieser Effekt wird als ”circular dichroism in the angular distribution” (CDAD)[1] genannt.

Üblicherweise [2; 3] wird das Photoemissionsmatrixelement des ”one-step model”, im Falle eines ebene-Welle-Endzustands, in der sogenannten Geschwindigkeits-Eichung berechnet. Im Zuge dessen kann das Photoemissionsmatrixelement als Fouriertransformation des Anfangszustandes aufgefasst werden. In dieser Beschreibung verschwindet der CDAD Effekt allerdings.

Die sogenannte Längeneichung bietet eine weitere Möglichkeit, das Photoemissionsmatrixelement auszuwerten. Darin wird der Wechselwirkungsanteil des Hamiltonoperators im Photoemissionsmatrixelement durch den Ortsoperator, anstelle des Impulsoperators in der Geschwindikeitseichung, dargestellt. Durch eine Spezialisierung auf planare Kohlenwasserstoffmoleküle wird ein Ausdruck für das Photoemissionsmatrixelement und dessen Polarisationsabhängigkeit gefunden. Ein tight-binding (TB) Modell, basierend auf Ergebnissen der Dichtefunktionaltheorie (DFT), wird konstruiert, um die elektronischen Eigenzustände von beliebigen planaren Kohlenwasserstoffmolekülen zu berechnen. Auf diese Weise wird eine Methode zur Berechnung der Intensitätsverteilung eines ARPES Experiments von beliebigen Kohlenwasserstoff Molekülen konstruiert. Mithilfe dieses Modells wird gezeigt, dass das Photoemissionsmatrixelement in der Längeneichung einen nicht verschwindenden CDAD Effekt aufweist.

Einen alternativen und potentiell genaueren Zugang, um ARPES Intensitätsverteilungen zu simulieren, bildet die zeitanbängige Dichtefunktionaltheorie (TDDFT). Die darin implementierte ”surface flux” Methode, welche ARPES Intensitäten ohne zustätzliche Näherung für den Endzustand ermöglicht, dient als Referenz für das TB Modell. Es wird gezeigt, dass die simulierten ARPES Intensitätsverteilung der TDDFT und der TB Methode für Graphen bei zirkular polarisiertem Licht erhebliche Unterschiede aufweisen.

Anschließend werden experimentelle Intensitätsverteilungen von [4] für das Molekül Tetracene mit einer entsprechneden TB-Simulation verglichen. Dabei wird eine signifikante Übereinstimmung beobachtet. Ob die Auswertung des Photoemissionsmatrixelements in der Längeneichung den CDAD Effekt für Moleküle generell richtig beschreibt, muss jedoch in zukünftigen Untersuchungen getestet werden.

Contents

1 Introduction 7

2 Methodological Background 9
2.1 Fermi's Golden Rule Expression . . . 9
2.2 ARPES-Experiment . . . 10
2.3 Graphene . . . 13
2.4 Tight-Binding-Approximation . . . 17
  2.4.1 Tight Binding Basics . . . 17
  2.4.2 The Hückel Model . . . 18
  2.4.3 Slater Koster formalism . . . 20
  2.4.4 The Löwdin Method . . . 22
  2.4.5 The TB-Model for Graphene . . . 24
2.5 Matrix Element in Velocity Gauge . . . 26
2.6 Density Functional Theory (DFT) . . . 28
2.7 Time-Dependent Density Functional Theory (TDDFT) . . . 31
  2.7.1 The Surface Flux Method . . . 34
  2.7.2 Vectorfield as External Potential . . . 36

3 Photoemission Matrix Element of Planar Hydrocarbons 39
3.1 Dichrosim of the $2p_z$ Orbitals . . . 39
  3.1.1 x-Polarization . . . 40
  3.1.2 y-polarization . . . 41
  3.1.3 z-polarization . . . 41
  3.1.4 Circular Dichroism of the $2p_z$ Orbital . . . 43
  3.1.5 Introduction of an l-Dependent Phase Factor . . . 44
3.2 Photoemission Matrix Element within an LCAO Ansatz . . . 46

4 Implementation 48
4.1 Application of the Hückel Model . . . 48
4.2 Overlap of Hückel- and DFT Molecular Orbitals . . . 54
4.3 TB Simulation with Chinook . . . 59
  4.3.1 ARPES-Simulations in *Chinook* . . . 64
  4.3.2 Interpolating Cuts on the Band Maps . . . 68
4.4 TDDFT Calculation with Octopus . . . 74

5 Comparison and Analysis 83
5.1 Conclusions of the Chinook Simulations . . . 83
5.2 Comparison of the Linear Dichroism . . . 87
5.3 Application of the LCAO Method . . . 90
5.4 The LCAO Method for a Graphene like System . . . 93

6 Conclusion 103

7 Appendix **106**

1 Introduction

Angle-resolved photoemission spectroscopy (ARPES) is an experimental technique to investigate the electronic structure of surfaces and interfaces. Over the past decades it has helped to improve our understanding of the electronic structure of various materials systems, and in particular, of organic-metal interfaces. From a first-principles perspective, such an interface between an organic molecule and a metallic surface can be considered as a many-particle quantum mechanical system treated using the Schrödinger equation. Practically solving this coupled many particle differential equation is only possible numerically within appropriate approximations.

Density functional theory (DFT)[5] is a widely used method to calculate the electronic ground state of a quantum mechanical many body system. In principle, it allows one to calculate the exact ground state of the system from scratch without any empirical knowledge, making it a so called ab-initio method. A semiempirical approach is the so called tight binding (TB) method. Within this model it is possible to calculate the electronic eigenstates of a given system with less computational afford than other popular methods such as DFT or Hartree-Fock, and thus even very large systems can be treated. However the tight binding method presupposes information of the system and is therefore not an ab-initio-method. The molecules forming metal-organic interfaces often are hydrocarbons solely made up of carbon and hydrogen atoms. Within this limitation a model can be setup which calculates the electronic eigenstates of an arbitrary planar hydrocarbon molecule from scratch within the TB-model.

With the knowledge of the electronic eigenstates of a given quantum mechanical system it is possible to make predictions of the corresponding intensity distribution of an ARPES experiment. In the so called one-step model of photoemission [6] the photocurrent, obtained from a photoexcitation from an initial state to a final unbound state, is treated as a single coherent process. The photoemission matrix element is proportional to the photocurrent. Within the one-step model the final state of the photoelectron is often chosen to be a free electron and thus as a plane wave [2; 3]. This photoemission matrix element with a plane wave final state can, in the so called velocity gauge, be interpreted as Fourier transform of the initial state [2]. The absolute value of the expression depends not only on the initial and final state but additionally on the polarization of the incident light beam.

One particular effect regards the influence of the photocurrent on the handedness of the incoming circularly polarized light. In particular, the photoemission matrix element of circularly polarized light is of interest. The difference in the angular distribution of the photocurrent of the right and left handed circularly polarized light is called circular dichroism in the angular distribution (CDAD) [1]. However, when using the velocity gauge and approximating the final state by a plane wave, it can be shown that no circular dichroism effect is to be expected.

In this work the photoemission matrix element of the one step model will be evaluated in the so called length gauge. The difference of the two formalisms is the operator in the expectation value sandwiched by the initial and final states of the photoemission matrix element. The velocity gauge uses the momentum operator, while the length gauge expression features the position operator, respectively. In principle both approaches should be equivalent, however while the CDAD effect vanishes in the velocity gauge, it can be shown that this is not the case in length-gauge.

In the so called Hückel model [7], the molecular orbitals of planar hydrocarbons are assumed to be linear combinations of $2p_z$ orbitals only. It can be shown that the CDAD effect vanishes for a single $2p_z$ orbital also in the length gauge expression for a plane wave final state. Schönhense stated in [1] that altering the final state reintroduces the CDAD effect in this case. Following this idea, it is of interest, if this modified final state can improve ARPES simulations of planar hydrocarbons obtained by the photoemission matrix element in length gauge, in the context of the CDAD effect.

If reasonable, the so obtained technique could provide an ansatz to simulate CDAD effects within the one-step model of photoemission.

2 Methodological Background

2.1 Fermi's Golden Rule Expression

The famous Fermi's golden rule expression [8], named after Enrico Fermi, describes the transition rate from an initial state to a final state of a quantum mechanical system as response of a weak periodic perturbation. It is widely used to describe photoemission experiments such as ARPES [9; 10] which will also be done in this work. In order to derive Fermi's golden rule, we assume a perturbed system given by the Hamilton operator $\mathbf{H}$ to be described as a sum of an unperturbed system, denoted as $\mathbf{H}_0$ and the perturbation defined as $\mathbf{H}_1$. The Hamiltonian of an electron in the valence band under the influence of an external vector potential is given by

$$\mathbf{H} = \mathbf{H}_0 + \mathbf{H}_1 = \mathbf{H}_0 + \left[\frac{e}{2m_e}(\mathbf{p}\cdot\mathbf{A} + \mathbf{A}\cdot\mathbf{p})\right] + \frac{e^2}{2m_e c^2}\mathbf{A}^2, \tag{2.1}$$

where $\mathbf{A}$ denotes the external vector potential. In the following, the quadratic term is assumed to be small and is neglected. With the commutation relation $[\mathbf{p}, \mathbf{A}] = i\hbar\nabla\mathbf{A}$ one can rewrite $\mathbf{Ap} + \mathbf{pA}{=}2\mathbf{Ap}$. The time dependent vector potential is written in the form

$$\mathbf{A}(t) = -\mathbf{A}_d \cdot \alpha e^{-i(\omega t - \mathbf{k}\cdot\mathbf{r})} \tag{2.2}$$

and assuming the long wave limit ($k \longmapsto 0$) simplifies to

$$\mathbf{A}(t) = -\mathbf{A}_d \cdot \alpha e^{-i\omega t}, \tag{2.3}$$

where α denotes the amplitude and $\mathbf{A}_d = \frac{\mathbf{A}}{|\mathbf{A}|}$ the polarization direction.

The initial state of a time dependent quantum mechanical system can be written as

$$|\psi_i(t)\rangle = \sum_n a_n(t)e^{it\omega_n}|\psi_n(t_0)\rangle \tag{2.4}$$

By the use of the time dependent Schrödinger equation

$$\mathbf{H}\psi = i\hbar\frac{\partial\psi}{\partial t} \tag{2.5}$$

,the orthogonality of the ψ_n and by sandwiching with $< \psi_f|$, the time dependence of the coefficients $a_f(t)$ can be written down as

$$i\hbar\partial_t a_f(t) = \sum_{n=0}^{\infty}\langle\psi_n|\mathbf{H}_1|\psi_f\rangle a_n(t)e^{i\omega_{f,n}t} = \langle\psi_i|\mathbf{H}_1|\psi_f\rangle a_i(t)e^{i\omega_{f,i}t}, \tag{2.6}$$

where $\omega_{f,n} = \frac{E_f - E_n}{\hbar}$ and by assuming in the last step a perturbation series where for small time intervals only the term $n = i$ contributes. The above equation can therefore be integrated to

$$i\hbar a_f^{(1)}(t) \approx \int_{-\infty}^{t} dt'\,\langle\psi_n|\mathbf{H}_1|\psi_f\rangle\, e^{i\omega_{i,f}t'} \tag{2.7}$$

with $\omega_{i,f} = \omega_i - \omega_f$. To evaluate the transition rate $R_{ef}(T)$ from an initial state ψ_i to a final state ψ_f, one needs to calculate the transition probability which is calculated by $|a_f(t)|^2$. The transition rate $R_{ef}(T)$ is thus given by

$$\begin{aligned} R_{ef}(T) = \frac{|a_f(t)|^2}{T\hbar^2} = -\frac{1}{T\hbar^2}\left|\int_{-\infty}^{t} \langle\psi_f|\,\mathbf{H}_1\,|\psi_i\rangle\, e^{i\omega_{i,f}t'}dt'\right|^2 = \\ \frac{1}{T\hbar^2}\,|\alpha|^2\left|\int_{-\infty}^{t} e^{it'(-\omega-\omega_f+\omega_i)}dt'\right|^2 |\langle\psi_f|\,\mathbf{A}_d\cdot\mathbf{p}\,|\psi_i\rangle|^2 = \\ \frac{1}{T}\,|\alpha|^2\left|\int_{-\infty}^{t} e^{it'(-E-E_f+E_i)}dt'\right|^2 |\langle\psi_f|\,\mathbf{A}_d\cdot\mathbf{p}\,|\psi_i\rangle|^2 \end{aligned} \tag{2.8}$$

For $t \longmapsto \infty$ this becomes:

$$R_{ef}(T) = \frac{2\pi}{T}\,|\alpha|^2\,|\langle\psi_f|\,\mathbf{A}_d\cdot\mathbf{p}\,|\psi_i\rangle|^2\,\delta(E_{fi}-E) \tag{2.9}$$

where E_{fi} describes the energy quantum needed for the transition from ψ_i to ψ_f with $E_{fi} = \hbar\omega_{fi}$. So $\omega = \omega_{fi}$ is equivalent to $E_f = E_i + \hbar\omega$ and the final expression is known as Fermi's golden rule expression

$$R_{ef}(T) = \frac{2\pi}{T}\,|\alpha|^2\,|\langle\psi_f|\,\mathbf{A}_d\cdot\mathbf{p}\,|\psi_i\rangle|^2\,\delta(E_f - E_i - \hbar\omega). \tag{2.10}$$

This expression can thus be used to describe optical transitions, where both initial and final states are bound states, as well as transitions from a bound initial to a free final state. Therefore photoemission processes can be treated with Fermi's golden rule expression. The evaluation of the matrix element $|\langle\psi_f|\,\mathbf{A}_d\cdot\mathbf{p}\,|\psi_i\rangle|$ will be discussed in more detail later.

2.2 ARPES-Experiment

Angle-resolved photoemission spectroscopy (ARPES) offers the most direct access to measure the electronic bandstructure of surfaces. In ARPES experiments the sample is illuminated with monochromatic light of the energy $h\nu$. By energy conservation, the kinetic energy of an electron escaping the surface after absorbing a photon is given by [9]

$$E_{kin} = h\nu - \Phi - E_B. \tag{2.11}$$

Here, E_{kin} is the kinetic energy of the emitted electron, Φ is the workfunction and E_B denotes the binding energy. The energy of the free electron approximated by a plane wave, in the non-relativistic regime ($v << c$), is given by:

$$E_{kin} = \frac{\hbar^2 k^2}{2m_e} \tag{2.12}$$

where m_e is the electron mass.

In ARPES experiments, the emitted electrons are detected in terms of their kinetic energy as well as their emission angle [9]. The parallel momenta components are obtained by

$$k_x = \sqrt{\frac{2m_e E_{kin}}{\hbar}} \sin(\vartheta)\cos(\varphi) \tag{2.13}$$

$$k_y = \sqrt{\frac{2m_e E_{kin}}{\hbar}} \sin(\vartheta)\sin(\varphi) \tag{2.14}$$

where ϑ and φ are the polar and azimuthal emission angles as indicated in Figure 2.1.

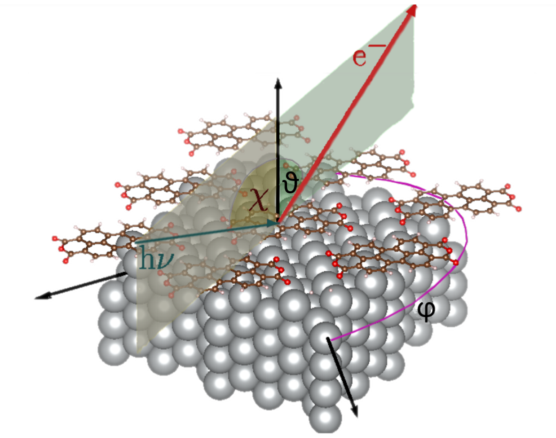

Figure 2.1: Schematic of the geometry of an ARPES experiment with angles as defined above. χ denotes the angle of the incoming photons of the energy $h\nu$ in respect to the surface. The emitted electron is detected as a function of the polar angle ϑ and it's kinetic energy. By rotation of the surface around the azimuthal angle φ, one can measure the entire subspace above the sample surface.

The outcome of an ARPES experiment is the intensity of emitted electrons as a function of the binding energy E_B and parallel momenta components k_x and k_y. When assuming a dipole transition, the intensity distribution $I(E, k_x, k_y)$ of the photoemitted electrons can be analytically calculated with Fermi's golden rule expression [8] which is discussed in Section 2.1. Thus, within the one-step-model of photoemission, the photo-excitation is treated as a single coherent process, from bound state $|\psi_i\rangle$ with energy E_i, to the free state $|\psi_f\rangle$ with energy E_f and parallel momentum components k_x and k_y [10]. The definition of the momentum operator $\mathbf{p}$ evaluated in position representation gives $\mathbf{p} = -i\hbar\nabla$. Together with Equation 2.10, this gives

$$I(E, k_x, k_y) \propto \sum_i |\langle\psi_f(E, k_x, k_y)|\, \mathbf{A}\cdot\nabla\, |\psi_i\rangle|^2 \times \delta(E_i + \Phi + E - \hbar\omega), \tag{2.15}$$

where $\mathbf{A}$ is the polarization vector of the incoming photon. By assuming a plane with wave vector $\mathbf{k}$ as the final state $|\psi_f\rangle$ the photocurrent I_i becomes proportional to the Fourier transform of the initial wave function $\tilde{\psi}_i$ modulated by a polarization factor [10]

$$I(E, k_x, k_y) \propto |\mathbf{A} \cdot \mathbf{k}|^2 \times \left| \tilde{\psi}_i(k_x, k_y) \right| . \tag{2.16}$$

For a certain constant binding energy E_B, $|\mathbf{k}|$ is a constant. Therefore the Fourier transformed wavefunction $\tilde{\psi}_i$ is evaluated on a sphere with radius $|\mathbf{k}|$. This can be visualized as a cut of a sphere through momentum space representation of the initial state orbital (see Figure 2.2).

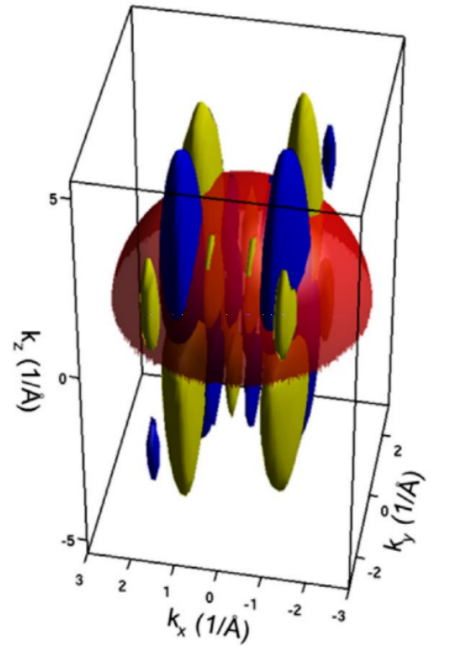

Figure 2.2: This Figure, taken from [10], shows the Fourier transformed initial state (blue and yellow) in 3d k space. The energy of the final state is given by Equation 2.12 and is thus a function of the absolute value of the wave vector $\mathbf{k}$. A constant energy is thus a sphere in 3d k-space here displayed in red. The ARPES intensity of a constant energy evaluated with Equation 2.16 is the cut of the Fourier transformed initial state with the corresponding constant energy sphere.

2.3 Graphene

Graphene is an allotrope of carbon, in which the carbon atoms arrange in a two-dimensional hexagonal lattice. Graphene has become famous for its interesting electronic properties an is described as a zero-gap semi-conductor. Thus, the valence- and conduction band "touch" at the Dirac points (or K points) of the first Brillouin zone. In this work, we will focus on the so called dichroism effect. In general dichroism refers to the optical absorption-properties of a material for different polarizations of light. In particular, this work investigates how different polarization states of the incoming photon affect the photoemission current. This effect can be studied on graphene very well. Its simple two dimensional structure as well as its small unit cell containing only 2 atoms makes it possible to do very expensive numerical calculations (such as with TDDFT, which we will deal with in Section 2.7) relatively fast. Moreover properties can even be calculated analytically. But let us start at the very beginning by defining the geometry of graphene.

Graphene has a hexagonal structure which originates from a triangular lattice with a basis of two atoms per unit cell. A possible choice for lattice vectors would be:

$$\mathbf{a}_1 = a\,(1,0,0)\ ,\ \mathbf{a}_2 = a\left(-\tfrac{1}{2},\tfrac{\sqrt{3}}{2},0\right) \tag{2.17}$$

with a CC-bond length $a_L \approx 1.42$ Å and a lattice vector length of $a = 2.47$ Å. In reduced coordinates the two atoms are located at

$$\mathbf{C}_1 = (0,0,0)\ ,\ \mathbf{C}_2 = (\tfrac{1}{3},\tfrac{2}{3},0). \tag{2.18}$$

With this information one can visualize the lattice graphene in real space.

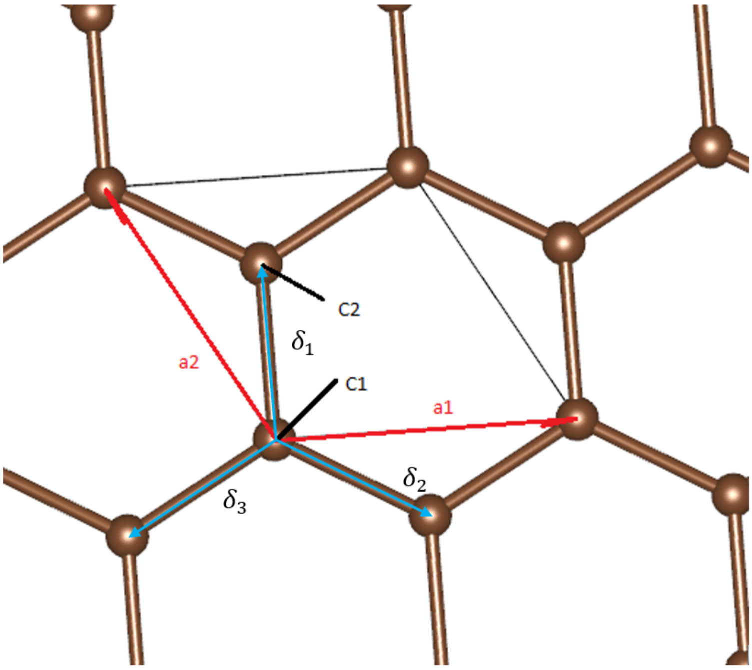

Figure 2.3: Atomic structure of graphene with lattice vectors $\mathbf{a}_1$, $\mathbf{a}_2$ (See Equation 2.17) and atom basis at position $\mathbf{C}_1$ and $\mathbf{C}_2$ (see Equation 2.18). The nearest neighbor vectors $\boldsymbol{\delta}_n$ of $\mathbf{C}_1$ are displayed in blue.

The nearest neighbors of atom $\mathbf{C}_1$ are defined as

$$\boldsymbol{\delta}_1 = a\left(0, \tfrac{1}{\sqrt{3}}, 0\right), \boldsymbol{\delta}_2 = a\left(\tfrac{1}{2}, \tfrac{-1}{2\sqrt{3}}, 0\right), \boldsymbol{\delta}_3 = a\left(-\tfrac{1}{2}, \tfrac{-1}{2\sqrt{3}}, 0\right). \tag{2.19}$$

In a solid like graphene one can make use of the translational symmetries and thus of Bloch's theorem [11]. The eigenvalues E_n of the Schrödinger equation depend on the wave vector $E_n(\mathbf{k})$. They are periodic in k-space which is spanned by the reciprocal lattice vectors.

Let us now take a look at the Brillouin zone of graphene. The reciprocal lattice can be constructed with the relation $\mathbf{a}_i \cdot \mathbf{b}_j = 2\pi\delta_{i,j}$ where $\mathbf{b}_j$ denotes a reciprocal lattice vector, one can construct the $\mathbf{b}_j$ with the use of the lattice vectors from Equation 2.17 to be

$$\mathbf{b}_1 = \tfrac{2\pi}{a}\left(\tfrac{\sqrt{3}}{2}, \tfrac{1}{2}, 0\right), \mathbf{b}_2 = \tfrac{2\pi}{3a}(0, 1, 0). \tag{2.20}$$

Taking a look at the first Brillouin-zone one can again see a hexagonal structure. The Dirac cones defining the zero-band gap are located at the corners of the Brillouin zone, denoted as $\mathbf{K}$-points, and are given by

$$\mathbf{K} = \tfrac{2\pi}{a}\left(\tfrac{1}{2\sqrt{3}}, \tfrac{1}{2}, 0\right), \mathbf{K}' = \tfrac{2\pi}{a}\left(-\tfrac{1}{2\sqrt{3}}, \tfrac{1}{2}, 0\right), \tag{2.21}$$

which in reduced coordinates are given by

$$\mathbf{K} = \left(\tfrac{1}{3}, \tfrac{1}{3}, 0\right)\ , \mathbf{K}' = \left(-\tfrac{1}{3}, \tfrac{2}{3}, 0\right). \tag{2.22}$$

An image of the Brillouin zone is displayed below.

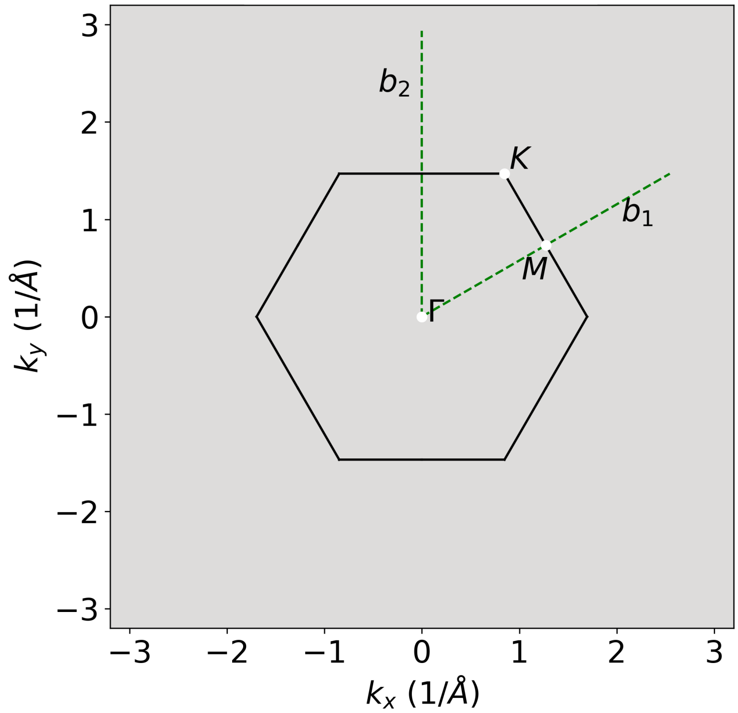

Figure 2.4: The first Brillouin zone of graphene with Γ, M and K points. $\mathbf{b}_1$ and $\mathbf{b}_2$ denote the reciprocal lattice vectors (see Eq: 2.20))

To describe the optical properties of a material the electronic properties are needed. There are various methods to determine these such as the tight-binding method and the DFT method which will be discussed in Section 2.4 and 2.6. For graphene the two-dimensional dispersion relation is shown below for a DFT calculation performed via the *Octopus* code (see [12]) using a LDA functional and the pseudopotential set *hgh-lda*.

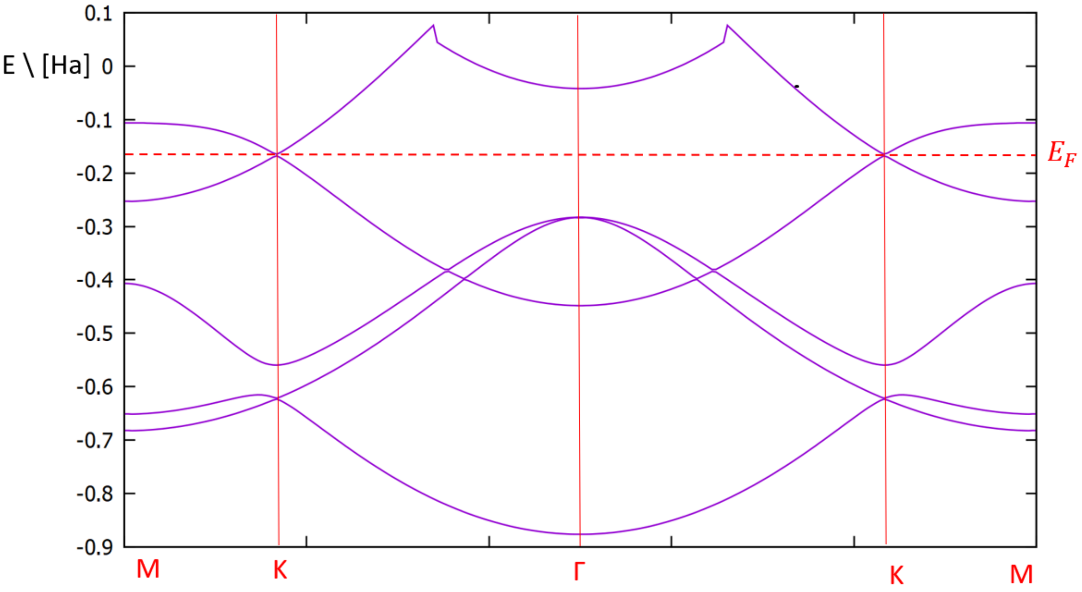

Figure 2.5: Bandstructure of graphene with a k-point path $M - K - \Gamma - K - M$ see Figure 2.4.

One can see that at the **K**-points the topmost valence band and lowest conduction band form Dirac cones. The Dirac points are degenerated points in the band structure due to the point group of graphene. The fact that the valence and the conduction band are touching each other at the **K** point results in the description of graphene as a ”zero-gap semi-conductor”. Although graphene offers a lot of interesting properties it will be used here mainly to provide a test material for the dichroism effect. The idea is to simulate an ARPES experiment of graphene (see Section 2.2) with the use of Fermi’s golden rule expression (see Section 2.1). Therefore one needs an initial state the electron of the photoemission process emerges from. The following sections will deal with this problem in detail.

2.4 Tight-Binding-Approximation

The tight binding model is a quantum mechanical model to calculate the electronic band structure. Within the tight-binding approximation, electrons are assumed to be "tightly bound" to the atom which they belong to. This means that they only have limited interaction with states and potentials of neighboring atoms. As a consequence this method allows for fast computations in comparison to other methods such as DFT which will be discussed in the later Section 2.6. Many papers such as Refs.[13; 14] covering properties of graphene start out with a tight binding ansatz delivering realistic models for a various set of problems.

2.4.1 Tight Binding Basics

Here, some of the basic concepts of the tight binding approach will be discussed very briefly. As a starting point one needs eigenfunctions Ψ of the Hamiltonian eigenvalue equation of the form

$$H\Psi(\mathbf{k},\mathbf{r}) = E(\mathbf{k})\Psi(\mathbf{k},\mathbf{r}). \tag{2.23}$$

In the tight binding approach these eigenfunctions are constructed as a linear combination from valence orbitals of the contributing atoms of the unit cell of a crystal. It should be noted that atomic orbitals on different sites are in principle not orthogonal. This problem will be dealt with later. In Section 2.4.4 a construction method for orthogonal atomic orbitals introduced by Löwdin [15] is presented. Solid state physics deals with periodic systems. Here the Hamiltonian operator H has certain invariances referring to the translational symmetry of the solid. Thus the eigenfunctions of Equation 2.23 are for a periodic system set up as so called Bloch functions which are classified by the wave vector $\mathbf{k}$ as

$$\Psi(\mathbf{r},\mathbf{k})_{m,a} = N^{-\frac{1}{2}} \sum_n e^{i\mathbf{k}\cdot\mathbf{R}_n} \phi_{m,a}(\mathbf{r} - \mathbf{R}_n - b_m) \tag{2.24}$$

where $\phi_{m,a}$ are orthogonal atomic orbitals with the unit cell index n, m being the atom index of the unit cell and a the index of the associated orbital. The Bloch basis functions given by Equation 2.24 incorporate the translational symmetry properties of the Hamiltonian. They are eigenfunctions of the translational operator and fulfill the equation

$$\Psi(\mathbf{k},\mathbf{r}+\mathbf{R}) = e^{i\mathbf{k}\mathbf{R}}\Psi(\mathbf{k},\mathbf{r}). \tag{2.25}$$

On the other hand, taking a look at a finite molecular system, a so called LCAO (linear combination of atomic orbitals) ansatz is often made. Here the basis functions of the corresponding Schrödinger equation are in position representation setup as

$$\Psi_i(\mathbf{r}) = \sum_{n,a} c_n^i \phi_{a,n}(\mathbf{r} - \mathbf{R}_n), \tag{2.26}$$

where $\phi_{a,n}(\mathbf{r})$ are the atomic orbitals with the atom index n, the quantum number a of the associated orbital and i the index of the eigenfunction of the Hamiltonian also referred to as molecular orbital. The eigenenergies of a molecular system are not a function of $\mathbf{k}$ but discrete. In the following calculation we will deal with a Bloch-type basis function. The calculation would be similar however for an LCAO ansatz. Without any further discussion about the Hamiltonian H, the energy eigenvalues can be calculated with the use of the Schrödinger equation as

$$H\left|\Psi_k\right\rangle = E_k\left|\Psi_k\right\rangle \tag{2.27}$$

and by sandwiching this expression from the left by a single basis orbital $< \phi_n|$

$$\left\langle\phi_n\right| H\left|\Psi_k\right\rangle = E_k\left\langle\phi_n|\Psi_k\right\rangle \tag{2.28}$$

which can be decoupled. By using Equation 2.24 in the above expression one ends up with

$$\sum_m c_m(\mathbf{k})\left\langle\phi_n|H|\phi_m\right\rangle = E(\mathbf{k})\sum_m c_m(\mathbf{k})\left\langle\phi_n|\phi_m\right\rangle \tag{2.29}$$

which can be rearranged as a matrix equation:

$$H_{n,m}c_m(\mathbf{k}) = S_{n,m}c_mE(\mathbf{k}) \tag{2.30}$$

With the corresponding matrix elements:

$$H_{n,m} = \int \phi_n^* H(\mathbf{r})\phi_m d\mathbf{r} \tag{2.31}$$

and

$$S_{n,m} = \int \phi_n^*\phi_m d\mathbf{r} \tag{2.32}$$

Usually not all of these matrix elements are evaluated. For the case of a *orthogonal tight binding theory* the overlap matrix $S_{m,n}$ is approximated by $\delta_{m,n}$. This leads to a simple eigenvalue problem. To some extent really crude approximations are made such as for the Hückel-model (see Section: 2.4.2) which still yields reasonable results. A widely used TB-application is the Slater-Koster formalism which will also be used in this work via the *chinook* package described by [16]. It should also noted that the parameters used in the tight-binding (TB) theory are often taken empirically making it a semi-empirical method. As discussed in [17]: "If the tight binding approximation contains enough of the physics of the system we are studying then any reasonably chosen set of parameters will provide us with a useful model". Or in the words of Slater and Koster [18]: "Instead of computing the various integrals analytically, we shall use them as disposable constants, to be chosen so that we shall fit the results of more accurate calculation made by other methods".

2.4.2 The Hückel Model

Erich Hückel [7] introduced a simplified model in order to describe aromatic π conjugated systems. Due to its simplicity, the Hückel model is a commonly used method. It can be used to describe π conjugated hydrocarbon systems. With the refined extended Hückel model also other orbitals can be included, this however will not be needed here but can be looked up in [19]. For the Hückel-model we start out with a molecular orbital Hamiltonian H_{mol} and a LACO ansatz.

$$\Psi = \sum_i c_i \phi_i \tag{2.33}$$

with ϕ_i being normalized atomic orbitals. In principle atomic orbitals at different atomic sites are not orthogonal, one can however orthogonalize them by the method of Löwdin [15] described in Section 2.4.4. Here we will simply assume that the atomic orbitals are orthogonal as part of the Hückel model. With the stationary Schrödinger equation

$$H\psi = E\psi \tag{2.34}$$

and by substituting Equation (2.33) into this expression, we end up with:

$$\sum_i c_i \phi_i H = E \sum_i c_i \phi_i. \tag{2.35}$$

With applying $\int d^3 r \phi_j$ to right side ,which is the same operation as in Equation 2.28, we obtain

$$\sum_{j=1}^{n} (H_{ij} - ES_{ij}) c_j = 0 \tag{2.36}$$

with

$$H_{ij} = \int_{\Re^3} \phi_i^* \hat{H} \phi_j dV \tag{2.37}$$

refereed to as the Hamilton matrix and

$$S_{ij} = \int_{\Re^3} \phi_i^* \phi_j dV \tag{2.38}$$

referred to as the overlap matrix, with $(i, j = 1, .., n)$. This problem has a solution if $[H_{ij} - ES_{ij}]$ is singular. Hence E must satisfy:

$$\det([H_{ij} - ES_{ij}]) = 0 \tag{2.39}$$

known as the secular equation. For the Hückel-model further simplifications are performed:

- Only nearest neighbors are taken into account, so $H_{ij} \neq 0$ only for atom i being a neighbor of atom j.
- For aromatic planar C-H molecules it is assumed that the energy of an electron is in an isolated C($2p_z$) orbital.

- The energy of all bonds of the molecule are reduced to the bonds between the C($2p_z$) orbitals (The C-H interactions are not taken into account).
- The overlap integral given by Equation 2.38 is approximated by the identity matrix.

By assuming a spherically symmetric potential around each nucleus and taking advantage of the rotational symmetry of the $2p_z$ orbital around z-axis, one can easily see the corresponding matrix element of Equation 2.37 becomes a function of the distance of the two orbitals only. In other words the carbon-carbon matrix element of $2p_z$ orbitals, called the hopping parameter $\beta(r)$, can be expressed as a function of the C-C bond length r.

For example lets take a look at benzene. With exactly the same distances between the C atoms, the Hamilton matrix elements in the Hückel approximation of Equation 2.37 can take exactly 2 different values. α for H_{ii} and β for H_{ij} for $i \neq j$ with R_i,R_j being neighbor atoms:

$$H = \begin{pmatrix} \alpha & \beta & 0 & 0 & 0 & \beta \\ \beta & \alpha & \beta & 0 & 0 & 0 \\ 0 & \beta & \alpha & \beta & 0 & 0 \\ 0 & 0 & \beta & \alpha & \beta & 0 \\ 0 & 0 & 0 & \beta & \alpha & \beta \\ \beta & 0 & 0 & 0 & \beta & \alpha \end{pmatrix} \tag{2.40}$$

The parameters of this matrix are then fitted to experimental energies or more accurate methods. The eigenvectors of the Hamilton matrix are the coefficients c_n forming the eigenfunctions of the Hamiltonian as given in Equation 2.33. These eigenfunctions are remarkably close to the molecular orbitals obtained with more accurate methods such as the DFT method described in Section 2.6. In this work we will fit this model to the DFT method, and find that it is justified to use the Hückel model for such systems. In more involved numerical calculations, this method therefore can be used to make a fast approximation of the molecular orbitals and the energies of a planar carbohydrate system. The computational effort is reduced to the diagonalization of a $n \times n$ matrix, where n is the number of carbon atoms of the system.

2.4.3 Slater Koster formalism

In 1954 Slater and Koster formulated a new tight binding based method [18]. The methods starts off with an LCAO ansatz for n different atomic orbitals $\phi_n(\mathbf{r} - \mathbf{R}_i)$ with $\mathbf{R}_i$ being the atomic origin of atom i. The so called Bloch sums $B_{n,k}(\mathbf{r})$ defined by

$$B_n(\mathbf{k}, \mathbf{r}) = \sum_j e^{i\mathbf{k}\mathbf{R}_j} \phi_n(\mathbf{r} - \mathbf{R}_j) \tag{2.41}$$

are used to construct the wave function, as a linear combination

$$\Psi_{\mathbf{k}}(\mathbf{r}) = \sum_n B_n(\mathbf{k}, \mathbf{r}) c_n. \tag{2.42}$$

"In general, except at special **k** values, there will be matrix components of energy between all these Bloch sums, so that we shall have a secular problem whose order equals that of the total number of atomic orbitals" [18]. They also make a statement about the symmetry of the wavefunction: "a wave function of a given k value must be made up as a linear combination of functions having the symmetry properties of s, p_x, p_y, p_z ,.. orbitals, and will not have the characteristics of any one of these types of orbitals."[18]

"if we start with the atomic orbitals ϕ_n located on the various atoms of a unit cell, and make Bloch sums from them, then we shall find that these Bloch sums are not orthogonal to each other. The reason is that the ϕ_n's connected with orbitals on different atoms and are thus not orthogonal to each other. We can remove this difficulty by immediately setting up new atomic orbitals, linear combinations of the original ones, which are orthogonal to each other. This can be done most symmetrically by the method of Löwdin." [18]

Starting off with atomic orbitals ϕ_j at the origin of each atom site, orthogonal atomic orbitals ψ_j are obtained by the use of Löwdins method described in the Section 2.4.4. So $\psi_{j,\alpha}(\mathbf{r}-\mathbf{R}_n-\mathbf{b}_j)$ is the orthonormal atomic orbital of atom j with quantum numbers α in the unit cell denoted by $\mathbf{R}_n$.

Bloch functions of the form

$$\Psi_{\mathbf{k}}(\mathbf{r})_{j,\alpha} = N^{-\frac{1}{2}} \sum_n e^{i\mathbf{k}\cdot\mathbf{R}_n} \psi_{j,\alpha}(\mathbf{r}-\mathbf{R}_n-\mathbf{b}_j) \tag{2.43}$$

where **k** is the Bloch-wavevector, N the number of unit cells in the sum, lattice vectors are denoted as $\mathbf{R}_n$, with a set of atoms j located at positions $\mathbf{b}_j$ in each unit cell.

Since the Hamiltonian H has lattice periodicity, by the use of Equation 2.43, the Hamiltonian can be block-diagonalized with each block corresponding to a specific **k**.
For a chosen **k** value (looking at the corresponding block) one can describe the matrix elements by:

$$H_{h\alpha,j\beta}(\mathbf{k}) = \sum_n e^{(i\mathbf{k}\cdot\mathbf{R}_n)} \int \psi^*_{h\alpha}(\mathbf{r}-\mathbf{R}_n-\mathbf{b}_h)\hat{H}\psi_{j\beta}(\mathbf{r}-\mathbf{b}_j)d^3r \tag{2.44}$$

where the translational symmetry is used to remove one of the sums over **R** (can be seen in [20]). The single particle potential of H can be separated into potentials $V_m(\mathbf{r})$ centered at site $\mathbf{b}_m$ (atomic potentials $V_m(\mathbf{r})$) as

$$V(\mathbf{r}) = \sum_{nm} V_m(\mathbf{r}-\mathbf{R}_n-\mathbf{b}_m), \tag{2.45}$$

In the following steps only *on-site* integrals and *two-center* integrals are taken into account. *On-site* integrals refer to both atomic-like functions $\psi_{h\alpha}$ and $\psi_{j\beta}$ having the same atom site as the potential at $\mathbf{b}_k$. *Two-center* integrals refer to one of the wavefunctions having the same atom site as $\mathbf{b}_k$.

When assuming spherically symmetric potentials $V_m(\mathbf{r})$, the *on-site* matrix elements are diagonal elements, the off-diagonal elements in the *two-center* approximation only depend on the displacement $\mathbf{u}$ [20] given by

$$H_{\alpha\beta}^{ij}(\mathbf{u}) = \int d^3r \psi_{i\alpha}^*(\mathbf{r} - \mathbf{u}) H \psi_{j\beta}(\mathbf{r}). \tag{2.46}$$

Here i, j denote the atomic positions and the angular momenta contained in α and β. Assuming the atomic orbitals ϕ_i being s,p or d angular momenta only, each term of Equation 2.46 can be expressed in 14 Slater-Koster parameters denoted as $H_{ab\gamma}(\mathbf{u})$ where a and b specify the angular momenta of the orbitals (s,p,d) and $\gamma = \sigma, \pi, \delta$ specifies the component of the angular momentum relative to the direction $\mathbf{u}$ [20].

2.4.4 The Löwdin Method

In Section 2.4.1 it was already mentioned that atomic orbitals of distant atoms are in principle not orthogonal. Their overlap may be small but neglecting it should be well justified. In his paper Löwdin [15] showed that the secular equation problem of including a non diagonal overlap matrix can be reduced to the same form as for a diagonal overlap matrix with a transformed Hamilton matrix. These orthogonal atomic orbitals can be set up as a linear combination of the original non-orthogonal ones. Löwdin started off by defining the molecular wavefunctions as linear combinations of atomic orbitals of the form

$$\Psi_i = \sum_{\mu=1}^{n} \phi_\mu \chi_{\mu,i} \tag{2.47}$$

The problem of this ansatz is that the Bloch-sums of Equation (2.41) are not orthogonal to each other. This is due to a non-vanishing overlap of orbitals of different atoms as already mentioned.

Therefore the secular equation is constructed in a different way than in Equation (2.39) for the original tight binding approach. By defining the overlap matrix as

$$S_{m,n} = \int \phi_m^* \phi_n d\tau - \delta_{m,n} \tag{2.48}$$

and not using any simplifications on the overlap matrix, one ends up with the secular equation of the form:

$$\sum_{\nu=1}^{n} H_{\mu,\nu} \chi_\nu = \sum_{\nu=1}^{n} \left(\delta_{\mu,\nu} + S_{\mu,\nu}\right) \chi_\nu E. \tag{2.49}$$

Here $H_{\mu,\nu}$ are the matrix elements of the Hamilton-matrix, χ_ν is the coefficient of atomic orbital ν for a specific eigenfunction of the Hamilton matrix with the corresponding eigenvalue E. In matrix form this can be written as:

$$\hat{\mathbf{H}}\mathbf{x} = (\hat{\mathbf{1}} + \hat{\mathbf{S}})\hat{\mathbf{x}}\hat{\mathbf{E}} \tag{2.50}$$

with $\hat{\mathbf{E}}$ now being a diagonal matrix with $E_i = E_{i,i}$. Equation 2.48 implies the normalization condition:

$$\sum_{\mu,i} \chi_{\mu,i}(\delta_{\mu,\nu} + S_{\mu,\nu})\,\chi_{\nu,i} = 1. \tag{2.51}$$

Now a new matrix $\hat{\mathbf{C}}$ of the form:

$$\chi_{\mu,k} = (\delta_{\mu,j} + S_{\mu,j})^{-\frac{1}{2}} C_{j,k} \tag{2.52}$$

is introduced. It can be written in matrixform as:

$$\hat{\mathbf{x}} = (\hat{\mathbf{1}} + \hat{\mathbf{S}})^{-\frac{1}{2}}\hat{\mathbf{C}} \tag{2.53}$$

where the matrix $(\mathbf{S}{+}\mathbf{1})^{-\frac{1}{2}}$ is formally given by a series expansion. With eq: (2.52) the secular equation (2.49) can be expressed as:

$$\hat{\mathbf{H}}'\hat{\mathbf{C}} = \hat{\mathbf{C}}\hat{\mathbf{E}} \tag{2.54}$$

with the expressions $\widehat{\mathbf{H}}' = (\hat{\mathbf{1}}+\hat{\mathbf{S}})^{-\frac{1}{2}}\mathbf{H}(\hat{\mathbf{1}}+\hat{\mathbf{S}})^{-\frac{1}{2}}$ and $\hat{\mathbf{C}}^{+}\hat{\mathbf{C}} = \hat{\mathbf{1}}$. So the secular equation problem of including a non diagonal overlap matrix can be reduced to the same form as for a diagonal overlap matrix with a transformed Hamilton matrix $\hat{\mathbf{H}}$' which is again self adjoint.

One can construct a set of fully orthogonal atomic wavefunctions ψ from the overlapping atomic orbitals ϕ forming the molecular orbitals Ψ. With the construction of

$$\phi = \psi(\hat{\mathbf{1}} + \hat{\mathbf{S}})^{-\frac{1}{2}} \tag{2.55}$$

forming orthogonal wavefunctions

$$\int \psi^*\psi d\tau = \int \phi^*(\hat{\mathbf{1}} + \hat{\mathbf{S}})^{-1}\phi d\tau \overset{2.48}{\overbrace{=}} \int \phi^*(\int \phi^*\phi d\tau')^{-1}\phi d\tau = \int \phi^*\phi d\tau(\int \phi^*\phi d\tau')^{-1} = \delta. \tag{2.56}$$

The molecular orbitals thus are calculated by

$$\Psi_j = \sum_{\mu}^{n} \psi_\mu C_{\mu,j} \tag{2.57}$$

This section only sketches the method of Löwdin. In his paper [15] he talks about the treatment of $\mathbf{H}'$, the calculation of the $\mathbf{C}$ matrix, appliance to certain systems and simplifications. We will however stop here since this method is not explicitly implemented in this work but rather implicitly used by the Slater-Koster formalism [18] from Section 2.4.3 of the Chinook package [16] later.

2.4.5 The TB-Model for Graphene

To evaluate Fermi's golden rule expression of Section 2.1 for graphene, one needs an initial state. Here the TB-model of Section 2.4.1 will be used to calculate the highest valence- and lowest conduction band. Therefore we will assume that only the $2p_z$ orbitals of the carbon atoms are involved. We will also suppose that the $\psi_{2p_z}(\mathbf{r}+\mathbf{R}_n-\mathbf{R}_j)$ are orthonormal. It describes the $2p_z$ orbital of atom at site $\mathbf{R}_j$ in the unit cell of $\mathbf{R}_n$.

First, Bloch functions of the form

$$\phi^j_{\mathbf{k}}(\mathbf{r}) = N^{-\frac{1}{2}} \sum_n e^{i\mathbf{k}\cdot(\mathbf{R}_n+\mathbf{R}_j)} \psi_{2p_z}(\mathbf{r}-\mathbf{R}_n-\mathbf{R}_j) \tag{2.58}$$

are setup, where $\mathbf{k}$ is the Bloch-wavevector, n the index of the sum over the lattice vectors. Lattice vectors are denoted as $\mathbf{R}_n$, with a set of atoms j located at positions $\mathbf{b}_j$ in each unit cell. So the two basis functions of graphene take the form

$$\phi^1_{\mathbf{k}}(\mathbf{r}) = N^{-\frac{1}{2}} \sum_n e^{i\mathbf{k}\cdot(\mathbf{R}_n+\mathbf{R}_1)} \psi_{2p_z}(\mathbf{r}-\mathbf{R}_n-\mathbf{R}_1) \tag{2.59}$$

and

$$\phi^2_{\mathbf{k}}(\mathbf{r}) = N^{-\frac{1}{2}} \sum_n e^{i\mathbf{k}\cdot(\mathbf{R}_n+\mathbf{R}_2)} \psi_{2p_z}(\mathbf{r}-\mathbf{R}_n-\mathbf{R}_2). \tag{2.60}$$

The matrix elements of the energy expectation values are given by the 2 × 2 matrix

$$H_{i,j}(\mathbf{k}) = \left\langle \phi^i_{\mathbf{k}}(\mathbf{r}) \right| \hat{H} \left| \phi^j_{\mathbf{k}}(\mathbf{r}) \right\rangle = \begin{pmatrix} H_{1,1} & H_{1,2} \\ H^*_{1,2} & H_{2,2} \end{pmatrix} \tag{2.61}$$

The diagonal elements are called onsite-energies and are calculated as:

$$H_{j,j}(\mathbf{k}) = \frac{1}{N} \sum_{\mathbf{R},\mathbf{R}'} e^{i\mathbf{k}(\mathbf{R}-\mathbf{R}')} \left\langle \psi_{2p_z}(\mathbf{r}-\mathbf{R}-\mathbf{R}_j) \right| \hat{H} \left| \psi_{2p_z}(\mathbf{r}-\mathbf{R}'-\mathbf{R}_j) \right\rangle \tag{2.62}$$

Only including nearest neighbor interactions for the onsite element restricts ($\mathbf{R}=\mathbf{R}'$) and leads to

$$= \frac{1}{N} \sum_{\mathbf{R}} \left\langle \psi_{2p_z}(\mathbf{r}-\mathbf{R}-\mathbf{R}_j) \right| \hat{H} \left| \psi_{2p_z}(\mathbf{r}-\mathbf{R}-\mathbf{R}_j) \right\rangle = \epsilon_{2p}. \tag{2.63}$$

The off-diagonal elements are parametrized by the so called hopping parameter and are calculated as:

$$H_{1,2}(\mathbf{k}) = \frac{1}{N} \sum_{\mathbf{R},\mathbf{R}'} e^{i\mathbf{k}(\mathbf{R}-\mathbf{R}'+\mathbf{R}_1-\mathbf{R}_2)} \left\langle \psi_{2p_z}(\mathbf{r}-\mathbf{R}-\mathbf{R}_1) \right| \hat{H} \left| \psi_{2p_z}(\mathbf{r}-\mathbf{R}-\mathbf{R}_2) \right\rangle \tag{2.64}$$

The vector $\mathbf{R}-\mathbf{R}'+\mathbf{R}_1-\mathbf{R}_2$ refers to the nearest neighbor positions (see Figure 2.3) denoted as $\boldsymbol{\delta}_1, \boldsymbol{\delta}_2, \boldsymbol{\delta}_3$.

$H_{1,2}$ can thus be written as

$$H_{1,2}(\mathbf{k}) = \frac{1}{N}\sum_{\mathbf{R}}\left(e^{i\mathbf{k}\boldsymbol{\delta}_1} + e^{i\mathbf{k}\boldsymbol{\delta}_2} + e^{i\mathbf{k}\boldsymbol{\delta}_3}\right)\cdot t = \underbrace{\left(e^{i\mathbf{k}\boldsymbol{\delta}_1} + e^{i\mathbf{k}\boldsymbol{\delta}_2} + e^{i\mathbf{k}\boldsymbol{\delta}_3}\right)}_{f(\mathbf{k})}\cdot t \tag{2.65}$$

where t is the hopping parameter.

Substituting Equation 2.58 into the Schrödinger equation

$$\hat{H}\left|\phi_{\mathbf{k}}^{j}\right\rangle = E(\mathbf{k})\left|\phi_{\mathbf{k}}^{j}\right\rangle \tag{2.66}$$

and sandwiching $\left\langle\phi_{\mathbf{k}}^{j}\right|$ from the left leads to the matrix equation

$$\sum_j H_{i,j}c_j = \sum_j ES_{i,j}c_j. \tag{2.67}$$

By assuming a diagonal overlap matrix $S_{i,j}$ the eigenvalue problem can be solved by

$$\det(\hat{H} - E\cdot\mathbf{1}) = 0. \tag{2.68}$$

Now inserting the elements of the Hamilton matrix $H_{1,1}$ and $H_{1,2}$ as

$$\begin{vmatrix} \epsilon_{2p} - E & tf(\mathbf{k}) \\ tf(\mathbf{k})^* & \epsilon_{2p} - E \end{vmatrix} = 0 \tag{2.69}$$

one identify the eigenenergies as

$$E_{\pm}(\mathbf{k}) = \epsilon_{2p} \pm t\cdot|f(\mathbf{k})| \tag{2.70}$$

where $t < 0$ and the ± sign refers to "+" being the valence and "-" being the conduction band. With the coefficients $\mathbf{c}$ from Equation 2.67 now given by

$$\mathbf{c}_{\pm} = \frac{1}{\sqrt{2}}\left(\pm\underbrace{e^{i\nu(\mathbf{k})}}_{\frac{f(\mathbf{k})}{|f(\mathbf{k})|}}, 1\right) \tag{2.71}$$

the corresponding eigenfunctions can be written as

$$\begin{aligned} \Psi_{+}(\mathbf{k}) &= \frac{1}{\sqrt{2}}\left[-e^{-i\nu(\mathbf{k})}\cdot\phi_{1,\mathbf{q}}(\mathbf{r}) + \phi_{2,\mathbf{k}}(\mathbf{r})\right] \\ \Psi_{-}(\mathbf{k}) &= \frac{1}{\sqrt{2}}\left[e^{i\nu(\mathbf{k})}\cdot\phi_{1,\mathbf{q}}(\mathbf{r}) + \phi_{2,\mathbf{k}}(\mathbf{r})\right]. \end{aligned} \tag{2.72}$$

The Equation 2.70 gives the bandstructure of graphene around the Fermi energy. The points where $E_{+}(\mathbf{k}) = E_{-}(\mathbf{k})$ define the tip of the Dirac cones of graphene and identify it as a zero-band gap semiconductor. The expressions 2.72 now describe the state forming the valence- and the conduction band. We will later refer to these expressions in order to evaluate the dichroism effect of an ARPES experiment and end this section here.

2.5 Matrix Element in Velocity Gauge

A theoretical description of ARPES experiments can be accomplished within the so called one-step model of photoemission [6]. Within this approach the ARPES intensity is in principle evaluated by the use of Fermi's golden rule expression [8][9][10] which is discussed in Section 2.1. The corresponding transition matrix element is called the photo emission matrix element. The external field is treated as perturbation and under the assumption of a weak field $A^2 \to 0$ one ends up with a perturbation of

$$H_1 = \frac{e}{m_e}\mathbf{A}(t)\mathbf{p}. \tag{2.73}$$

The momentum operator can be written in position representation as $\mathbf{p} = -i\hbar\nabla$. Fermi's golden rule expression in dipole approximation gives

$$M(\mathbf{k}) = \langle \psi_f \left| \mathbf{A} \cdot \mathbf{p} \right| \psi_i \rangle \tag{2.74}$$

which is the transition matrix element where $\langle \psi_f \,|$ is the final- and $|\psi_i\rangle$ the initial sate. This is called the velocity form since the operator used for the transition probability is the momentum operator. We will take a look at this formalism for graphene. The photoemission matrix element calculated in this way depends on the polarization of the light. For the TB model of graphene discussed in Section 2.4.5 the transition matrix element with a plane wave final state can be relatively easily evaluated in velocity gauge as

$$M(\mathbf{k}) = \left\langle \Psi_{\pm}(\mathbf{q}) \left| \mathbf{A} \cdot \mathbf{p} \right| e^{i\mathbf{kr}} \right\rangle = -i\hbar\mathbf{A} \int d^3r \Psi_{\pm}(\mathbf{q},\mathbf{r})^* \nabla e^{i\mathbf{kr}} \tag{2.75}$$

Where $\Psi_{\pm}(\mathbf{q})$ are the eigenstates from Equation 2.72 given in Section 2.4.5. This expression can be evaluated straight forward as

$$|M(\mathbf{k})|^2 = \hbar^2 |\mathbf{A} \cdot \mathbf{k}|^2 \left| \int d^3r \Psi_{\pm}(\mathbf{q},\mathbf{r})^* e^{i\mathbf{kr}} \right|^2 = \hbar^2 |\mathbf{A} \cdot \mathbf{k}|^2 \left| \mathcal{F}(\Psi_{\pm})(\mathbf{k}) \right|^2 \tag{2.76}$$

with $\mathcal{F}(\Psi_{\pm})(\mathbf{k})$ being the Fourier transformation of $\Psi_{\pm}(\mathbf{q},\mathbf{r})$. Without any further evaluations of this expression, some important statements can be made. The dependence on the polarization of the light in the photoemission matrix element can be reduced to a factor of $|\mathbf{A} \cdot \mathbf{k}|^2$. In this work we will take a look at different polarization directions and especially at circularly polarized light.

Circularly polarized light can be expressed with two perpendicular vectors $\mathbf{A}_1$ and $\mathbf{A}_2$ as $\mathbf{A}_1 \pm i\mathbf{A}_2$ where the ± sign defines the handedness of the light. The difference of the photoemission matrix element for left and right handed polarized light is called circular dichroism. The photo emission matrix element depends on the polarization by the factor $|\mathbf{A} \cdot \mathbf{k}|^2$. This factor gives the same value for right and left handed polarized light. So the corresponding circular dichroism angular distribution (CDAD) vanishes. This is, however, not the case generally. Methods beyond perturbation theory and a plane wave final state like TDDFT (discussed in Section 2.7) are able to simulate this effect.

The canonical commutation relation $[\mathbf{r}, \mathbf{H}_0] = -\frac{i\hbar}{m_e}\mathbf{p}$,where $\mathbf{H}_0$ is the unperturbed Hamiltonian from Section 2.1, can be used to transform expression 2.75 into the so called length form. Equation 2.75 thus changes to

$$M(\mathbf{k}) = \frac{mi}{\hbar}\mathbf{A} \cdot \left\langle e^{i\mathbf{kr}} | [\mathbf{r}, \mathbf{H}_0] | \Psi \right\rangle = \frac{mi}{\hbar}\mathbf{A} \cdot \left\langle e^{i\mathbf{kr}} | \mathbf{r}\mathbf{H}_0 - \mathbf{H}_0\mathbf{r} | \Psi \right\rangle . \tag{2.77}$$

Assuming $\left\langle e^{i\mathbf{kr}} \right|$ and $|\Psi\rangle$ to be eigenfunctions of $\mathbf{H}_0$ with eigenvalues E_{pw} and E_Ψ the above expression can be rewritten as

$$M(\mathbf{k}) = \frac{mi}{\hbar}\mathbf{A} \cdot (E_\Psi - E_{pw}) \left\langle e^{i\mathbf{kr}} | \mathbf{r} | \Psi \right\rangle \tag{2.78}$$

and thus

$$|M(\mathbf{k})|^2 = \left| \mathbf{A} \cdot \omega(\mathbf{k}) \left\langle e^{i\mathbf{kr}} | \mathbf{r} | \Psi \right\rangle \right|^2 , \tag{2.79}$$

where $\frac{(E_\Psi - E_{pw})m}{\hbar} = \omega(\mathbf{k})$. The corresponding transition matrix element is now obtained by the position operator which denotes it as the length form. In this form one can not immediately see the dependence of the matrix element on the polarization. Works such as [1][16][14] suggest that it is possible to see a CDAD in the length gauge or at least by making slight adjustments of the final state of the photoemission matrix element in length gauge. In the Chapter 5 we will compare the APRES simulation of graphene of a tight binding based program to TDDFT results. Subsequently there will be a detailed discussion of the analytical result of the photo emission matrix element for graphene in length-gauge.

2.6 Density Functional Theory (DFT)

Density functional theory, introduced by Hohenberg and Kohn [5], is a widely used method to calculate the electronic ground state of a quantum mechanical many body system. In principle it allows one to calculate the exact ground state of the system without having to solve the coupled many-body Schrödinger equation. This is done by mapping the system of interacting electrons on to an auxiliary system of non-interacting electrons in an effective potential. This potential includes the so called exchange-correlation contribution which needs to be approximated. The main object in DFT is the electron density. The auxiliary potential called the Kohn-Sham potential is a functional of the electronic density. By assuming an initial ground state density one can re-evaluate the Kohn-Sham potential and thus get to an improved ground state. The exact ground state is then obtained by iterating this procedure.

But let us start off at the very beginning with the many particle Hamiltonian (given in atomic units)

$$\hat{H} = -\frac{1}{2}\sum_{i=1}^{N}\nabla_i^2 + \sum_{i=1}^{N}\sum_{j>i}^{N}\frac{1}{|\mathbf{r}_i - \mathbf{r}_j|} - \sum_{i=1}^{N}\sum_{k=1}^{K}\frac{Z_k}{|\mathbf{r}_i - \mathbf{R}_j|} - \sum_{k=1}^{K}\frac{\nabla_k^2}{2M_k} + \sum_{k=1}^{K}\sum_{l>k}^{N}\frac{Z_k Z_l}{|\mathbf{R}_l - \mathbf{R}_k|}, \tag{2.80}$$

where $\mathbf{R}_k$ denotes the position of nucleus k with charge Z_k and mass M_k. $\mathbf{r}_i$ denotes the position of electron i. The first term describes the kinetic energy T of the electrons, the fourth one the kinetic energy of the nuclei. The third sum describes the Coulomb interaction of nuclei and electrons V_{ne}, the second the electron-electron and the fifth the nuclei-nuclei interaction V_{ee} and V_{nn}, respectively.
The fact that this is a coupled differential equation makes solving the Schrödinger equation a highly non trivial problem. Only very simple systems can be solved analytically. A first step in order to deal with bigger systems is to make a few assumptions. "Atomic nuclei are much heavier than individual electrons. Each proton or neutron in a nucleus has more than 1800 times the mass of an electron. This means, roughly speaking, that electrons respond much more rapidly to changes in their surroundings than nuclei can" [21].

By applying the so called Born-Oppenheimer approximation [22], which fixes the positions of the nuclei, one gets rid of the 4-th and 5-th term in Equation (2.80) and thus simplifies it to

$$H = -\frac{1}{2}\sum_{i=1}^{N}\nabla_i^2 + \sum_{i=1}^{N}\sum_{j>i}^{N}\frac{1}{|\mathbf{r}_i - \mathbf{r}_j|} + \sum_{i=1}^{N}v(\mathbf{r}_i) = T + V_{ee} + \sum_{i=1}^{N}v(\mathbf{r}_i) \tag{2.81}$$

where V_{ne} is rewritten as the external potential

$$v(\mathbf{r}) = -\sum_{k=1}^{K}\frac{Z_k}{|\mathbf{r} - \mathbf{R}_k|}. \tag{2.82}$$

It is shown by the Rayleigh-Ritz minimal principle that

$$E_g = \min_{\Psi} \langle\Psi|\, \hat{H}\, |\Psi\rangle \tag{2.83}$$

For simplicity the ground state energy E_g is from now on denoted as E. By variation of the normalized many-body wavefunction, such that it minimizes the matrix element, it matches the energy of the ground state.

At this point let us introduce the electron density, defined as

$$n(\mathbf{r}) = N \int \Psi^*(\mathbf{r}_1, ..., \mathbf{r}_N)\Psi(\mathbf{r}_i, ..., \mathbf{r}_N) d\mathbf{r}_1 ... d\mathbf{r}_N. \tag{2.84}$$

By fixing a trial density $n(\mathbf{r})$, where all wave functions resulting in this density are indicated by $\Psi \to n(\mathbf{r})$ one can write down the energy as a functional of the electronic density in the form

$$E[n(\mathbf{r})] = \min_{\Psi \mapsto n(\mathbf{r})} \langle\Psi|\, H\, |\Psi\rangle = \min_{\Psi \mapsto n(\mathbf{r})} \langle\Psi|\, T + V_{ee}\, |\Psi\rangle + \int d^3\mathbf{r} v(\mathbf{r}) n(\mathbf{r}) = F[n(\mathbf{r})] + \int d^3\mathbf{r} v(\mathbf{r}) n(\mathbf{r}) \tag{2.85}$$

with the universal functional $F[n(\mathbf{r})]$ defined as

$$F[n(\mathbf{r})] = \min_{\Psi \mapsto n(\mathbf{r})} \langle\Psi|\, T + V_{ee}\, |\Psi\rangle\,. \tag{2.86}$$

Now minimizing this energy by varying the electron density, this leads to the so called *Hohenberg and Kohn minimal principle*:

$$E = \min_{n(\mathbf{r})} E[n(\mathbf{r})] = \min_{n(\mathbf{r})} \left\{ F[n(\mathbf{r})] + \int d^3\mathbf{r} v(\mathbf{r}) n(\mathbf{r}) \right\}. \tag{2.87}$$

With the constraint of a fixed electron number implemented as Lagrangian multiplier ($N = \int d^3 r n(\mathbf{r})$) with the parameter μ, the variation $\frac{\delta}{\delta n(\mathbf{r})}$ yields

$$\delta \left\{ F[n(\mathbf{r})] + \int d^3 r v(\mathbf{r}) n(\mathbf{r}) - \mu \int d^3 r n(\mathbf{r}) \right\} = 0 \tag{2.88}$$

and thus follows that

$$\frac{\delta F[n(\mathbf{r})]}{\delta n(\mathbf{r})} + v(\mathbf{r}) = \mu. \tag{2.89}$$

This equation states that the external potential $v(\mathbf{r})$ is uniquely defines by the ground state density $n(\mathbf{r})$ up to an additive constant and is called the Hohenberg and Kohn theorem. Taking a look at Equation (2.81) it can be seen that H is determined by $v(\mathbf{r})$. The Hohenberg and Kohn theorem thus concludes that the ground state is a unique functional of $v(\mathbf{r})$.

Assuming the form of the universal functional $F[n(\mathbf{r})]$ is known, the Hohenberg and

Kohn theorem in principle enables us to determine the ground state density. Kohn and Sham, however, suggested a different technique in order to do so.

The Kohn-Sham method introduces an auxiliary external potential $v_s(\mathbf{r})$ of an independent many particle Hamiltonian, whose electron density matches the fully interacting one. By introducing the axillary Hamiltonian H_s

$$\hat{H}_s = -\frac{1}{2}\sum_{i=1}^{N}\nabla_i^2 + \sum_{i=1}^{N} v_s(\mathbf{r}_i) = \sum_{i=1}^{N} h_s(\mathbf{r}_i) \tag{2.90}$$

with the ground state wavefunction Φ of H_s defined by the Schrödinger equation

$$H_s \left|\Phi\right\rangle = E_s \left|\Phi\right\rangle . \tag{2.91}$$

The ground state wavefunction Φ can be constructed as single Slater determinant due to the Hamiltonian $\hat{H}_s$ being a sum of single particle operators. Now applying the Rayleigh-Ritz minimal principle as well a constrained minimization as above the energy of the system can be written as

$$E[n(\mathbf{r})] = \min_{\Phi\mapsto n(\mathbf{r})} \left\langle\Phi\right| H_s \left|\Phi\right\rangle = \min_{\Phi\mapsto n(\mathbf{r})} \left\langle\Phi\right| T \left|\Phi\right\rangle + \int d^3\mathbf{r} v_s(\mathbf{r}) n(\mathbf{r}) = T_s[n(\mathbf{r})] + \int d^3\mathbf{r} v_s(\mathbf{r}) n(\mathbf{r}) \tag{2.92}$$

where T_s is the kinetic energy functional of the non-interacting system. The ground state energy can then be obtained by the functional derivative as above leading to

$$\delta\left\{T_s[n(\mathbf{r})] + \int d^3r v_s(\mathbf{r}) n(\mathbf{r}) - \mu_s \int d^3r n(\mathbf{r})\right\} = 0 \tag{2.93}$$

and further

$$\frac{\delta T_s[n(\mathbf{r})]}{\delta n(\mathbf{r})} + v_s(\mathbf{r}) = \mu_s. \tag{2.94}$$

Now assuming that v_s reproduces the same density as v (is v-representable in both cases), one can combine it with Equation (2.89), absorb μ and μ_s in v_s and get

$$\frac{\delta F[n(\mathbf{r})]}{\delta n(\mathbf{r})} + v(\mathbf{r}) = \frac{\delta T_s[n(\mathbf{r})]}{\delta n(\mathbf{r})} + v_s(\mathbf{r}). \tag{2.95}$$

The universal functional $F[n(\mathbf{r})]$, as defined by Equation (2.86), can be split up into known parts (T_s the kinetic energy of the non interacting system and U the Hartree energy) and the unknown part (E_{xc} the exchange-correlation energy)

$$F[n(\mathbf{r})] = T_s[n(\mathbf{r})] + U[n(\mathbf{r})] + E_{xc}[n(\mathbf{r})] \tag{2.96}$$

absorbing the difficult physics. This directly leads to an expression for $v_s(\mathbf{r})$

$$v_s(\mathbf{r}) = v(\mathbf{r}) + \frac{\delta U[n(r)]}{\delta n(r)} + \frac{\delta E_{xc}[n(\mathbf{r})]}{\delta n(r)} = v(\mathbf{r}) + v_H([n],\mathbf{r}) + v_{xc}([n],\mathbf{r}). \tag{2.97}$$

The auxiliary external potential v_s, called the Kohn-Sham potential, reproduces the desired ground state electron density. It can be constructed from the single-particle orbitals $\phi_i(\mathbf{r})$ called the Kohn-Sham orbitals. These orbitals satisfy the eigenvalue equation

$$\left[-\frac{1}{2}\nabla^2 + v_s(\mathbf{r})\right]\phi_i(\mathbf{r}) = \epsilon_i\phi_i(\mathbf{r}) \tag{2.98}$$

known as the Kohn-Sham equations and are the foundation of the practical solution. They reproduce the full interacting ground state electron density $n(\mathbf{r})$ by:

$$n(\mathbf{r}) = \sum_{i=1}^{N} |\phi_i(\mathbf{r})|^2 \tag{2.99}$$

At the beginning of the calculation, we have in general no idea of how these Kohn-Sham orbitals look like. Thus, the Kohn-Sham potential of Equation 2.97 is also unknown.

By "guessing" an initial ground state density $n_{init}(\mathbf{r})$ and entering Equation (2.97) v_s is calculated. This is then used to determine the Kohn-Sham orbitals by Equation (2.98) and subsequently to update the ground state density by Equation (2.99). This procedure is repeated until convergence is reached meaning that $n(\mathbf{r})$ is as close as it can get to the full interacting ground state electron density. The ground state energy can than be computed with :

$$E[n] = T_s[n] + U[n] + E_{xc}[n] + \int d^3r v(\mathbf{r})n(\mathbf{r}) \tag{2.100}$$

The crucial part of this algorithm is finding an appropriate approximation for the exchange-correlation functional. With a known exact exchange-correlation functional DFT gives in principle an expression of the exact ground state density. However, this is in reality not the case. There is a number of different functionals which work better or worse for certain systems. Choosing the "right" functional is not trivial and the aim here is to give a crude overview of the method. DFT has a wide palette of applications in chemistry and physics. The accuracy and efficiency of the approximation of a a given physical system has made the KS procedure such a successful method.

2.7 Time-Dependent Density Functional Theory (TDDFT)

Where DFT tries to give a solution to the stationary Schrödinger equation, the so called time dependent density functional theory does the same for the time dependent Schrödinger equation. TDDFT provides a tool to calculate the time dependent electron density of a system in a time dependent external perturbation. It is thus possible to evaluate time dependent processes such as excitations. This extremely powerful method comes with the price of a high computational effort. Fundamentals are in principle similar to the DFT code. In the context of a time dependent many body problem we take a look at the time dependent Schrödinger equation (TDSE):

$$\widehat{H}(t)\Psi(t) = i\frac{\partial\Psi(t)}{\partial t} \tag{2.101}$$

with

$$\widehat{H}(t) = \widehat{T} + \widehat{V}_{ee} + \widehat{V}_{ext}(t) \tag{2.102}$$

where T denotes the kinetic energy, $\hat{V}_{ee}$ denotes the electron-electron repulsion and V_{ext} represents the combined potential the electrons experience due to the nuclear attraction and due to any field applied to the system [23].

Just like in ordinary (non time dependent) DFT, the main object is the electron-density $n(\mathbf{r}, t)$ of the interacting many body system. As the time-argument already implies, in TDDFT the electron density has a time dependence. The density $n(\mathbf{r}, t)$ is the probability (normalized to the particle number N) of finding any one electron, of any spin σ, at position $\mathbf{r}$ as described in [23] as

$$n(\mathbf{r}, t) = N \sum_{\sigma, \sigma_2 \ldots \sigma_N} \int d^3\mathbf{r}_2 \ldots \int d^3\mathbf{r}_N \left| \Psi(\mathbf{r}\sigma, \mathbf{r}_2\sigma_2 \ldots \mathbf{r}_N\sigma_N, t) \right|^2 . \tag{2.103}$$

Runge and Gross showed [24] that current densities $n_1(t, \mathbf{r})$ and $n_2(t, \mathbf{r})$ which evolve from the same initial state Ψ_0 in two physically distinct potentials $v_{ext}(\mathbf{r}, t)$ and $v'_{ext}(\mathbf{r}, t)$, will differ (proof can be seen in [23]). So with

$$v_{ext}(\mathbf{r}, t) \neq v'_{ext}(\mathbf{r}, t) + c(t) \tag{2.104}$$

follows that

$$\Psi_0(\mathbf{r}) : v_{ext}(\mathbf{r}, t) \rightharpoonup n(\mathbf{r}, t) \tag{2.105}$$

and

$$\Psi_0(\mathbf{r}) : v'_{ext}(\mathbf{r}, t) \rightharpoonup n'(\mathbf{r}, t) \tag{2.106}$$

with

$$n(\mathbf{r}, t) \neq n'(\mathbf{r}, t). \tag{2.107}$$

So a given time-dependent density points to a single time-dependent potential from a given initial state.
Due to the uniqueness of the solution of the TDSE, a given time dependent potential determines a unique time dependent wave function and thus a unique current density.

So there exists a one-to-one correspondence for a given initial state between the time-dependent density and the time-dependent potential up to a purely time-dependent constant.

$$\Psi_0(\mathbf{r}) : v_{ext}(\mathbf{r}, t) \longleftrightarrow n(\mathbf{r}, t) \tag{2.108}$$

This constant is the result of the gauge-freedom of the theory and appears as a pure phase factor in front of the wavefunction. For

$$V_{ext}(t) \longrightarrow V_{ext}(t) + c(t) \tag{2.109}$$

$$H(t) \longrightarrow H(t) + c(t) \tag{2.110}$$

And thus

$$\Psi(t) = e^{-iHt}\Psi_0 \rightharpoonup e^{-it(H+c(t))}\Psi_0 = e^{-itc(t)}\Psi(t) = \tilde{c}\Psi(t). \tag{2.111}$$

The wavefunction is, as discussed above, uniquely determined, up to a phase factor, as a functional of the density and the initial state

$$\Psi(t) = e^{-\alpha(t)}\Psi[n, \Psi_0](t). \tag{2.112}$$

To put all this to use, lets start with the time-dependent case of the DFT definition of the density. Via a non interacting single Slater-determinant of single-particle spin-orbitals $\phi_i(\mathbf{r}, 0)$ the density can be constructed as

$$n(\mathbf{r}, t) = \sum_{j=1}^{N} |\phi_j(\mathbf{r}, t)|^2 . \tag{2.113}$$

By assuming a non-interacting system with an auxiliary potential v_{KS} and the initial state Φ_0 to reproduce the given density uniquely of the fully interacting system,

$$i\frac{\partial}{\partial t}\phi_j(\mathbf{r}, t) = \left[-\frac{\nabla^2}{2} + v_{ext}[n; \Phi_0](\mathbf{r}, t) + v_{xc}[n; \Phi_0](\mathbf{r}, t) + v_H[n; \Phi_0](\mathbf{r}, t)\right]\phi_j(\mathbf{r}, t) \tag{2.114}$$

we obtain the time-dependent Kohn-Sham equations given by

$$i\frac{\partial}{\partial t}\phi_j(\mathbf{r}, t) = \left[-\frac{\nabla^2}{2} + v_{KS}[n; \Phi_0](\mathbf{r}, t)\right]\phi_j(\mathbf{r}, t). \tag{2.115}$$

This auxiliary potential should lead to the same energy in the TDSE as the interacting one and is thus defined as

$$v_{KS}[n; \Psi_0](\mathbf{r}, t) = v_{ext}[n; \Psi_0](\mathbf{r}, t) + \int d^3r' \frac{n(\mathbf{r}', t)}{|\mathbf{r} - \mathbf{r}'|} + v_{xc}[n; \Psi_0, \Phi_0](\mathbf{r}, t) \tag{2.116}$$

where v_{ext} is the external time-dependent field. The second term on the right-hand side is the time-dependent Hartree potential, describing the interaction of classical electronic charge distributions, while the third term is the exchange-correlation (xc) potential which, in practice, has to be approximated. [23]

By assuming an initial set of N orthonormal KS orbitals which must reproduce the exact density of the true initial state Ψ_0 and its first time derivative given as

$$\dot{n}(\mathbf{r}, t = 0) = -\nabla \cdot \Im m \sum_{i=1}^{N} \sum_{\sigma} \phi_i^*(\mathbf{r}, 0)\nabla\phi_i(\mathbf{r}, 0). \tag{2.117}$$

The TDKS equations (2.116) propagate these initial orbitals, under the external potential, together with the Hartree potential and an approximation for the exchange-correlation potential. As mentioned above, TDDFT calculations come with a high computational cost. In this work we will take a look at graphene in an adiabatically switched on external vector field with the aim to simulate the angle-resolved photoemission intensity distribution. For this purpose we will make use of the *octopus* code [12] which provides a TDDFT framework. In order to simulate an ARPES experiment *octopus* uses the T-SURF method which will be discussed in the next chapter.

2.7.1 The Surface Flux Method

To derive a suitable formalism which is capable of directly simulating the excitations and subsequent emission of electrons induced by an external photon field within TDDFT in semi-periodic systems, the surface flux or so called tSURFF method is employed [25]. This chapter should give an idea of how an ARPES experiment can be simulated in the *octopus* code [12] which is used in this work. In such a simulation one defines a volume (simulation box) where the system is in. Treating the entire simulation box in a full TDDFT formalism would be a very inefficient way. Electrons emitted in a photoemission process, will very soon not "see" the potential of the surface any more. Therefore the simulation region Ω is divided into 2 regions A and B. While in region A a fully interacting KS-Hamiltonian $\hat{H}_{KS}(t)$ is used, the electrons of region B are assumed to be free and non-interacting [25].

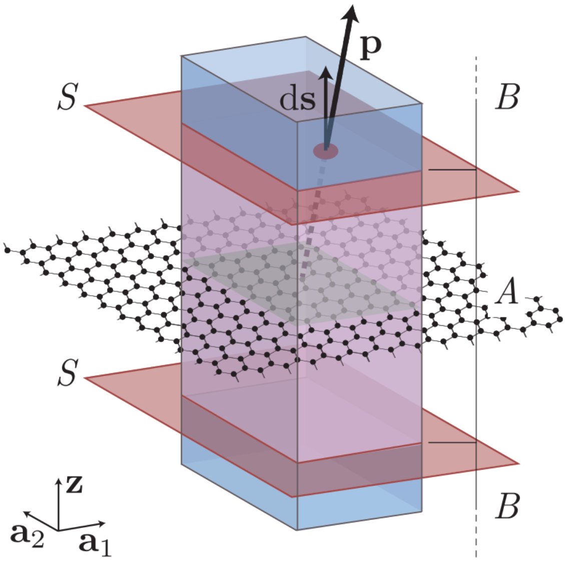

Figure 2.6: Simulation box for graphene taken from [25]. It shows the simulation regions A and B, the momentum of the emitted electron **p** and the interface **S** between regions A and B.

$$\hat{H}(t) = \begin{cases} \hat{H}_{KS}(t) & \text{for } \mathbf{r} \in \mathrm{A} \\ \hat{H}_V(t) & \text{for } \mathbf{r} \in \mathrm{B} \end{cases} \tag{2.118}$$

$\hat{H}_V(t)$ is the so called *Volkov Hamiltonian.* It describes a set of non interacting free electrons in an external vector field as

$$\hat{H}_V(t) = \frac{1}{2}\sum_{j=1}^{N}\left[-i\nabla_j - \frac{\mathbf{A}(t)}{c}\right]^2 \sigma_0. \tag{2.119}$$

It is diagonal in spin-space as denoted by σ_0 which is the identity. This can be solved as a set of single particle equations with the following plane wave spinors

$$\bar{\chi}_p(\mathbf{r}, t) = \sqrt{\frac{2\pi}{a_1 a_2}} e^{i\mathbf{pr}} e^{-i\phi(\mathbf{p},t)} \tag{2.120}$$

with the time dependent phase

$$\phi(\mathbf{p}, t) = \frac{1}{2} \int_0^\infty d\tau \left[\mathbf{p} - \frac{\mathbf{A}(\tau)}{c}\right]^2 \tag{2.121}$$

where a_1 and a_2 are defined by the volume via the normalization condition. Since these eigenstates also take into account the 2-dimensional periodicity of the system, they are denoted as Bloch-Volkov waves [25].

After switching off the external perturbation $\mathbf{A}(t > T) = 0$, the KS-spinors are assumed to be representable as a combination of scattered $\bar{\phi}_{j\mathbf{k},B}$ and bound component $\bar{\phi}_{j\mathbf{k},A}$ where these parts only "live" in their region.

$$\bar{\phi}_{j\mathbf{k}}(\mathbf{r}, t) = \bar{\phi}_{j\mathbf{k},A}(\mathbf{r}, t) + \bar{\phi}_{j\mathbf{k},B}(\mathbf{r}, t) \tag{2.122}$$

Under this assumption the number of electrons escaped per unit cell from region A at time T can be calculated as

$$N_{esc}(T) = \int_\Omega dr \int_{BZ} \sum_{j=1} \theta_j \left|\bar{\phi}_{j\mathbf{k},B}(\mathbf{r}, T)\right|^2 \tag{2.123}$$

where θ_j is a shorthand for $\theta(\mu - \epsilon_j)$ where ϵ_j are the eigenvalues of $\hat{H}_{KS}$.
With the KS-spinors expanded as Coulumb-Volkov waves of the form

$$\bar{\phi}_{j\mathbf{k},B}(\mathbf{r}, t) = \int dp(\bar{b}_j(\mathbf{p})\chi_{\mathbf{p}}(\mathbf{r}, t)) \tag{2.124}$$

with their coefficients $\bar{b}_j(\mathbf{p})$ where j denotes the spin. These coefficients can be calculated using the continuity equation

$$N_{esc}(T) = \int_0^T \oint_S d\mathbf{s}(\mathbf{J}(\mathbf{r}, \tau)) \tag{2.125}$$

where S is the surface of the simulation box as seen in Figure 2.6. With the single particle current density operator

$$\hat{\mathbf{j}}(t) = \frac{1}{2}\left[\left(-i\nabla - \frac{\mathbf{A}(t)}{c}\right) + cc.\right]\sigma_0 \tag{2.126}$$

the expectation value of the flux $\mathbf{J}(\mathbf{r}, t)$ from Equation 2.125 can be expressed as the expectation value of the single particle current density operator $\hat{\mathbf{j}}(t)$ from eq: 2.126 as:

$$\mathbf{J}(\mathbf{r}, t) = \sum_{j=1} \theta_j \int_{BZ} d\mathbf{k} \int d\mathbf{p}\bar{b}_j(\mathbf{p}) \langle\phi_{j\mathbf{k}}(t)|\,\hat{\mathbf{j}}(t)\,|\chi_{\mathbf{p}}(t)\rangle\,. \tag{2.127}$$

Inserting this expression into the continuity equation 2.125 and comparing it to Equation 2.123 leads to an expression for the coefficients

$$\bar{b}_j(\mathbf{p}) = -\int_0^T d\tau \oint_S d\mathbf{s}\, \langle \chi_{\mathbf{p}}(\tau) | \, \hat{\mathbf{j}}(\tau) \, |\phi_{j\mathbf{k}}(\tau)\rangle \, . \tag{2.128}$$

The spinless momentum-resolved photoelectron probability $P(\mathbf{p})$ is thus obtained as the derivative of the number of electrons escaped per unit cell with respect to $\mathbf{p}$ as

$$P(\mathbf{p}) = \frac{\partial N_{esc}(T)}{\partial \mathbf{p}} = \sum_{j=1} \theta_j \sum_{\alpha=-BZ}^{+} \int_{BZ} d\mathbf{k}\, |b_{j\alpha}(\mathbf{p})|^2 \, . \tag{2.129}$$

In order to use this method to simulate an ARPES experiment, one applies the external vector potential to the system. Since these simulations should resemble an experiment, the amplitude, intensity and frequency should match the ones of a realistic setup. How these parameters can be tuned by the vector field is described in the next chapter.

2.7.2 Vectorfield as External Potential

It is for example possible to include an external perturbation as in (Equation 2.102) via a time dependent external vector-potential. An adiabatically "switched on" external field is applied by multiplying the vector potential of the laser field (single frequency ω) with an envelope function $g(t)$ which increases and decreases slowly compared to the carrier frequency of the pulse.

$$V(t, \mathbf{r}) = f(\mathbf{r}) \cos(\omega t + \phi(t)) g(t) \tag{2.130}$$

where $f(\mathbf{r})$ describes a field type polarization or scalar potential. ω is defined by the photon-energy which is a parameter of the experiment.

$$E_{photo} = \hbar\omega \tag{2.131}$$

And $\phi(t)$ is the phase. The carrier frequency ω of the vector potential together with the amplitude of the envelope describes the intensity of the applied field as we will see now. For a linearly polarized laser pulse in $\mathbf{z}$ direction with a given $\sin^2$ envelope the vector filed would look like

$$\mathbf{A}(t, x) = A_0 \cdot \mathbf{z} \cdot \sin^2\left(\frac{\omega_{env} t}{2}\right) \cdot f(x) \cdot \cos(\omega t + \phi(t)). \tag{2.132}$$

One can think of it this way: The envelope function enables the adiabatic switch on process of the laser pulse. The maximum intensity of the signal is thus reached at the maximum of the envelope function. Since $\omega_{env} << \omega$ one can neglect the change of the envelope to calculate the maximum intensity. For a carrier frequency of $\omega = 46\ \frac{1}{fs}$, an envelope frequency of $\omega_{env} = 0.057\ \frac{1}{fs}$ and an amplitude of $A_0 = 1$ one can see this can be seen below.

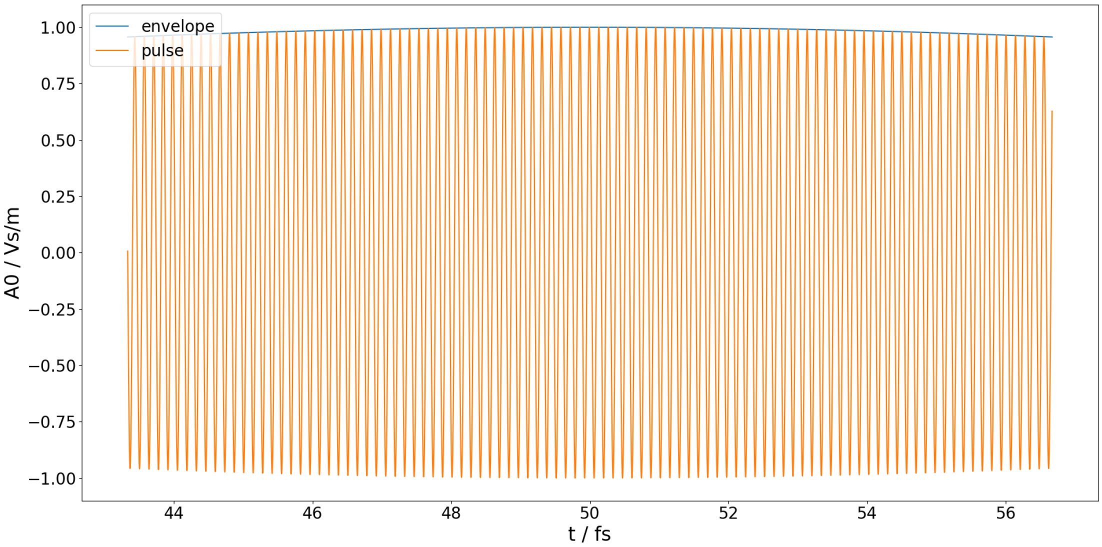

Figure 2.7: Example of an external vector field with envelope function g(t) being $\sin^2(\omega_{env}t)$ and a carrier frequency of ω with the frequencies described above.

The corresponding magnetic field of the Poynting vector would be

$$\mathbf{B} = \vec{\nabla} \times \mathbf{A} = \mathbf{y}A_0 \left(\frac{\partial f(x)}{\partial x}\right) \sin^2(\frac{\omega_{env}t}{2}) \cdot \cos(\omega t + \phi(t)) \tag{2.133}$$

with the assumption that $\omega_{env} << \omega$. Lets take a look at the intensity of the carrier wave

$$\mathbf{B} = \mathbf{y}A_0 \left(\frac{\partial f(x)}{\partial x}\right) \cdot \cos(\omega t + \phi(t)) \tag{2.134}$$

and the corresponding electric field

$$\mathbf{E} = -\frac{\partial \mathbf{A}}{\partial t} = \mathbf{z}A_0 \left(\frac{\partial f(x)}{\partial x}\right) \sin(\omega t + \phi(t)) \cdot \omega. \tag{2.135}$$

The intensity is defined as the time average of the energy flux $\mathbf{S}$ or Poynting vector. With the absolute value taken of the electric field and the magnetic field, the field type polarization $f(\mathbf{r})$ can be left aside and the absolute value of the Poynting vector is given by

$$|\mathbf{S}(t)| = |\mathbf{E}(t)|\,|\mathbf{B}(t)|\,\frac{1}{\mu_0} = \frac{A_0^2\omega}{\mu_0}\,|sin(\omega t + \phi(t))cos(\omega t + \phi(t))|\,. \tag{2.136}$$

This expression can then be integrated over a period T of the carrier frequency ω to get the intensity

$$I = \langle \mathbf{S} \rangle_t = \frac{1}{T\mu_0}\int_0^T |\mathbf{E}(t)|\,|\mathbf{B}(t)| = \frac{A_0^2\omega}{\pi\mu_0}. \tag{2.137}$$

A linearly polarized laser pulse in $\mathbf{z}$ direction with a given $\sin^2$ envelope dependent on intensity and photon-energy would be thus expressed as

$$\mathbf{A}(t) = \theta(T_{env} - t)\theta(t) \cdot \mathbf{z} \cdot \sqrt{\frac{I\pi}{\omega}} \cdot \sin^2\left(\frac{\omega_{env}t}{2}\right) \cdot f(x) \cdot \cos(\omega t + \phi(t)). \tag{2.138}$$

In the *octopus* code, the polarization of the vector potential $\mathbf{A}$ is set by the polarization vector

$$\mathbf{n} = [n_x, n_y, n_z]. \tag{2.139}$$

To make the connection to the statements above we again think of light as transverse wave consisting of the electric field $\mathbf{E}$ and the perpendicular magnetic field $\mathbf{B}$. These fields can be (here as an example for the $\mathbf{z}$-direction) setup as

$$\mathbf{E}_z(t, \mathbf{z}) = \Re\left([e_x, e_y, 0]e^{i(k\mathbf{z}-\omega t)}\right) \tag{2.140}$$

and

$$\mathbf{B}_z(t, \mathbf{z}) = \Re\left([b_x, b_y, 0]e^{i(k\mathbf{z}-\omega t)}\right). \tag{2.141}$$

where $[e_x, e_y, 0]$ and $[b_x, b_y, 0]$ are perpendicular and normalized. The polarization vector $\mathbf{n}$ used by the *octopus* code refers to the vector potential which translates directly into the $[e_x, e_y, e_z]$ indices of the electric field by Equation 2.135.

Note that n_x, n_y, n_z are possibly imaginary parameters. To get a linearly polarized vector field in the $\mathbf{z}$-direction one would use: $n_x = 1$ and $n_y = 0, n_z = 0$. A left handed circularly polarized vector field with a Poynting vector pointing to the z direction could, for example, be given by $n_x = 1, n_y = i, n_z = 0$. We will come back to this when actually simulating ARPES experiments with different light polarizations in the TDDFT *octopus* code for graphene in Section 4.4.

3 Photoemission Matrix Element of Planar Hydrocarbons

3.1 Dichrosim of the $2p_z$ Orbitals

As shown in Section 2.1, optical transition rates can be calculated via Fermi's golden rule expression using the transition matrix element. In order to evaluate the transition matrix element, one needs an initial state such a molecular orbital for a molecule. Molecular orbitals can, in an LACO ansatz, be described by a linear combination of atomic orbitals. For a planar hydrocarbon molecule the Hückel model, as described in Section 2.4, can provide a reasonable tool to do so. Within the Hückel model one sets up the molecular orbitals as linear combination of $2p_z$ orbitals. Later in Section 4.1 we will develop a Hückel model based on DFT results to setup molecular orbitals for an arbitrary hydrocarbon molecule. For the final state wavefunction let us assume a plane wave.

The ARPES intensity distribution, which is proportional to the transition matrix element, depends on the polarization of the incident light beam. In particular, we are interested in the circular dichroism in the angular distribution, that is the difference in photoemission intensity maps for left and right handed circularly polarized light [1], respectively. In his paper [1] Schönhense showed explicitly that with the ansatz of a plane-wave final state, the circular dichroism angular distribution (CDAD) of a single $2p_z$ orbital vanishes for a $\mathbf{A} = [0, \pm i, 1]$ polarization. Here we expand this result by showing that the CDAD of a single $2p_z$ orbital vanishes for any polarization. Schönhense also suggests to include an angular momentum dependent phase factor in the final state in order to recover the CDAD.

We start our analysis by taking a $2p_z$ orbital as initial state:

$$\psi_{p_z}(\mathbf{r}) = \frac{1}{2\sqrt{6}} \left(\frac{Z}{a_0}\right)^{\frac{3}{2}} \rho\, r\, e^{(-\frac{\rho r}{2})} \cdot \left(\frac{3}{4\pi}\right)^{\frac{1}{2}} \cos(\theta), \tag{3.1}$$

where the abbreviation $\rho = (\frac{2Z}{na_0})$ has been made. Also note that the $2p_z$ wavefunction has no ϕ dependence.

The final state can be expressed by a plane wave expanded in spherical harmonics as described in [26] in the following way

$$e^{i\mathbf{kr}} = 4\pi \sum_{l=0}^{\infty} \sum_{m=-l}^{l} i^l j_l(kr) Y^*_{lm}(\phi_k, \theta_k) Y_{lm}(\phi, \theta). \tag{3.2}$$

Here Y_{lm} are the spherical harmonics defined as

$$Y_{lm}(\phi, \theta) = \frac{1}{\sqrt{2\pi}} \sqrt{\frac{2l+1}{2} \cdot \frac{(l-m)!}{(l+m)!}} P_{lm}(\cos(\theta)) e^{im\phi}, \tag{3.3}$$

where $P_{ml}(x) = \frac{(-1)^m}{2^l l!}(1-x^2)^{\frac{m}{2}} \frac{d^{l+m}}{dx^{l+m}}(x^2-1)^l$ are the Legendre-polynomials. The radial part is determined by the spherical Bessel functions $j_l(kr)$ which are given by

$j_l(\rho) = (-\rho)^l \left(\frac{1}{\rho}\frac{d}{d\rho}\right)^l \left(\frac{\sin(\rho)}{\rho}\right)$.

Using spherical coordinates, we evaluate the matrix element for an arbitrary polarization $\mathbf{A} = (A_x, A_y, A_z)$ as

$$M_{if} = \langle \psi_f | \, \mathbf{A} \cdot \mathbf{r} \, | \psi_i \rangle = \int d\phi d\theta \; dr r^2 \sin(\theta) e^{-i\mathbf{kr}} (\mathbf{A} \cdot \mathbf{r}) \psi_{p_z}(\mathbf{r}). \tag{3.4}$$

By inserting 3.2 one can rewrite this as

$$M_{if} = 4\pi \int d^3r \sum_{l=0}^{\infty} \sum_{m=-l}^{l} (-i)^l j_l(kr) Y_{lm}(\phi_k, \theta_k) Y^*_{lm}(\phi, \theta) (\mathbf{A} \cdot \mathbf{r}) \psi_{2p_z}(\mathbf{r}). \tag{3.5}$$

Next we split the integral into a radial and a spherical part. For this purpose, the function ψ_{2p_z} will be written as

$$\psi_{2p_z}(\mathbf{r}) = \underbrace{\frac{1}{2\sqrt{6}} \left(\frac{Z}{a_0}\right)^{\frac{3}{2}} \rho r e^{\left(\frac{-\rho r}{2}\right)}}_{R_{21}(r)} \underbrace{\left(\frac{3}{4\pi}\right)^{\frac{1}{2}} \cos(\theta)}_{Y_{10}(\theta)} = R_{21}(r) Y_{1,0}(\theta). \tag{3.6}$$

For a specific polarization directions the integral can be split up as a sum of the directions of the polarization ($\mathbf{A} \cdot \mathbf{r} = A_x x + A_y y + A_z z$). in order to evaluate the entire expression we will treat each direction separately.

3.1.1 x-Polarization

For the x direction the corresponding integral is

$$4\pi \int d^3r \sum_{l=0}^{\infty} \sum_{m=-l}^{l} (-i)^l j_l(kr) Y_{lm}(\phi_k, \theta_k) Y^*_{lm}(\phi, \theta) \underbrace{A_x(r \sin(\theta)\cos(\phi))}_{A_x x} \underbrace{\cos(\theta) f(r)}_{\psi_{2p_z}(\mathbf{r})}. \tag{3.7}$$

By identifying $\sin(\theta)\cos(\theta)\cos(\phi)$ with

$$\sin(\theta)\cos(\theta)\cos(\phi) = \frac{1}{2}\sin(\theta)\cos(\theta)\left(e^{i\phi} + e^{-i\phi}\right) = \frac{1}{2}\sqrt{\frac{8}{15\pi}}\left(Y_{2,-1} - Y_{2,1}\right) \tag{3.8}$$

and with the use of the orthogonality relation of the spherical harmonics given by

$$\int d\Omega Y_{l,m} Y^*_{l',m'} = \delta_{l,l'}\delta_{m,m'}, \tag{3.9}$$

the angular integral of Equation 3.7 can be evaluated as

$$\sum_{l=0}^{\infty} \sum_{m=-l}^{l} \int d\Omega Y^*_{lm} \sin(\theta)\cos(\theta)\cos(\phi) = \sqrt{\frac{2\pi}{15}}\, \delta_{l,2}\left(\delta_{m,-1} - \delta_{m,1}\right). \tag{3.10}$$

with the help of the Kronecker deltas, the summations in Integral 3.7 drops and we are left with the integral over r. We are left with the integral over r. The radial part of the remaining element is

$$\int_0^\infty drr^3 j_{l=2}(kr)R_{2,1}(r) = f_2(k) \tag{3.11}$$

and can be evaluated analytically. In the later presented program (see Section 5.3) we will however solve it numerically for convenience. The full contribution of the x polarization to the matrix element is

$$M(k,\phi_k,\theta_k)_x = 4\pi f_2(k)\sqrt{\frac{1}{10}}(Y_{2,1}(\theta_k,\phi_k) - Y_{2,-1}(\theta_k,\phi_k)). \tag{3.12}$$

3.1.2 y-polarization

The y contribution of the matrix element can be derived in analogous manner as in Section 3.1.1. By identifying spherical harmonics one can reduce the y contribution of Equation 6.12 to

$$M(k,\phi_k,\theta_k)_y = 4i\pi R_2(k)\sqrt{\frac{1}{10}}(Y_{2,1}(\theta_k,\phi_k) + Y_{2,-1}(\theta_k,\phi_k)). \tag{3.13}$$

3.1.3 z-polarization

As in Section 3.1.1 we start out with the matrix element expression of the z-direction as polarization given by

$$4\pi \int dr^3 \sum_{l=0}^{\infty}\sum_{m=-l}^{l} i^l\, j_l(kr)Y_{lm}(\phi_k,\theta_k)Y^*_{lm}(\phi,\theta)\, \underbrace{A_z r\cos(\theta)}_{A_z z}\underbrace{\cos(\theta)f(r)}_{\psi_{2p_z}(\mathbf{r})}. \tag{3.14}$$

The function $\cos^2(\theta)$ can be expressed as

$$\cos^2(\theta) = \frac{1}{3}\left(\sqrt{\frac{16\pi}{5}}Y_{2,0} + \sqrt{4\pi}Y_{0,0}\right). \tag{3.15}$$

With the use of the orthogonality relation of Equation 3.10 of the spherical harmonics one can find that the spherical integral

$$\int d\Omega Y^*_{lm}\cos^2(\theta) = \delta_{m,0}\frac{1}{3}\left(\sqrt{\frac{16\pi}{5}}\delta_{l,2} + \sqrt{4\pi}\delta_{l,0}\right). \tag{3.16}$$

The radial part of the remaining element of the sum is

$$\int_0^\infty drr^3 j_{l=2}(kr)R_{2,1}(r) = f_2(k) \tag{3.17}$$

and

$$\int_0^\infty drr^3 j_{l=0}(kr)R_{2,1}(r) = f_0(k) \tag{3.18}$$

and can be evaluated analytically. For convenience it is later on evaluated numerically. The full contribution of the z polarization to the matrix element is

$$M_z(k,\phi_k,\theta_k) = 4\pi\left(Y_{0,0}(\theta_k,\phi_k)f_0 - \sqrt{\frac{4}{5}}Y_{2,0}(\theta_k,\phi_k)f_2\right) \tag{3.19}$$

3.1.4 Circular Dichroism of the $2p_z$ Orbital

The photoemission matrix element can be derived using the transition dipole moment as shown in [1] by

$$\frac{d\sigma}{d\Omega}(k, \theta_k, \phi_k) \propto \left|\langle \psi_f \left| \mu \right| \psi_i \rangle\right|^2 , \tag{3.20}$$

with $\mu = \mathbf{A}\cdot\mathbf{r}$. We evaluate this expression for circularly polarized light in the $x-y$-plane using the result of Equation 3.12 and 3.13

$$\left|\langle \psi_f \left| x + iy \right| \psi_i \rangle\right|^2 = 8\pi^2 f_2^2 \frac{2\pi}{15} \left|2Y_{2,-1}(\theta_k, \phi_k)\right|^2 , \tag{3.21}$$

and

$$\left|\langle \psi_f \left| x - iy \right| \psi_i \rangle\right|^2 = 8\pi^2 f_2^2 \frac{2\pi}{15} \left|2Y_{2,1}(\theta_k, \phi_k)\right|^2 . \tag{3.22}$$

When taking the property $Y_{l,m}(\theta, \phi) = (-1)^m Y^*_{l,-m}(\theta, \phi)$ into account, we see that the dichroism expression vanishes

$$\left|\langle \psi_f \left| x - iy \right| \psi_i \rangle\right|^2 - \left|\langle \psi_f \left| x + iy \right| \psi_i \rangle\right|^2 = 0. \tag{3.23}$$

investigating the general case of a circularly polarized vector field of the form $\mathbf{A} = \mathbf{A}_1 \pm i\mathbf{A}_2$, which can be expressed by the two vectors

$$\mathbf{A}_1 = (\cos(\chi)\sin(\eta), \sin(\chi)\sin(\eta), \cos(\eta)), \tag{3.24}$$

and

$$\mathbf{A}_2 = (\cos(\chi)\cos(\eta), \sin(\chi)\cos(\eta), -\sin(\eta)), \tag{3.25}$$

perpendicular to each other. With the results of the previous section summarized in Equations 3.12, 3.13 and 3.19, the corresponding general dichroism expression can be evaluated as follows:

$$\begin{aligned} &\langle \psi_f \left| \mathbf{A}_1 \cdot \mathbf{r} \pm i\mathbf{A}_2 \cdot \mathbf{r} \right| \psi_i \rangle = \\ M_x \, \cos\chi \underbrace{(\sin\eta \pm i\cos\eta)}_{(\pm i e^{\mp i\eta})} + M_y \, \sin\chi &\underbrace{(\sin\eta \pm i\cos\eta)}_{(\pm i e^{\mp i\eta})} + M_z \, \underbrace{(\cos(\eta) \mp i\sin\eta)}_{e^{\mp i\eta}} = \\ &= e^{\mp i\eta} \left(\pm i(M_x\cos(\chi) + M_y\sin(\chi)) + M_z\right) . \end{aligned} \tag{3.26}$$

When looking at the expressions M_x and M_y in Equations 3.12 and 3.13 one notices that

$$M_x\cos(\chi) + M_y\sin(\chi) = \underbrace{4\pi R_2\sqrt{\frac{2\pi}{15}}}_{\tilde{c}} \left(e^{i\chi}Y_{2,1} - e^{-i\chi}Y_{2,-1}\right) . \tag{3.27}$$

With $Y_{2,-1} = -Y_{2,1}e^{-2i\phi}$, it follows that

$$M_x\cos(\chi) + M_y\sin(\chi) = \tilde{c}Y_{2,1}\left(e^{i\chi} + e^{-2i\phi}e^{-i\chi}\right) = \tilde{c}Y_{2,1}e^{-i\phi}\left(e^{i\chi}e^{i\phi} + e^{-i\phi}e^{-i\chi}\right) . \tag{3.28}$$

Multiplying out the expression $\left(e^{i\chi}e^{i\phi} + e^{-i\phi}e^{-i\chi}\right)$ with use of the Euler formula leads to

$$M_x\cos(\chi) + M_y\sin(\chi) = \tilde{c}Y_{2,1}e^{-i\phi}\,2\left(\cos(\phi)\cos(\eta) - \sin(\phi)\sin(\eta)\right). \tag{3.29}$$

Since $\tilde{c} \in \Re$ the above expression is real. This means for Equation 3.26 that

$$\langle\psi_f\left|\mathbf{A}_1\cdot\mathbf{r} \pm i\mathbf{A}_2\cdot\mathbf{r}\right|\psi_i\rangle = e^{\mp i\eta}\left(\underbrace{\pm i(M_x\cos(\chi) + M_y\sin(\chi))}_{\in\Im} + \underbrace{M_z}_{\in\Re}\right). \tag{3.30}$$

Therefore the absolute value of Expression 3.30 is independent of the handedness (independent of ±). So one can conclude also for a general case of circularly polarized light the corresponding dichroism expression for a single atomic $2p_z$ orbital:

$$\left|\langle\psi_f\left|\mathbf{A}_1\cdot\mathbf{r} - i\mathbf{A}_2\cdot\mathbf{r}\right|\psi_i\rangle\right|^2 - \left|\langle\psi_f\left|\mathbf{A}_1\cdot\mathbf{r} + i\mathbf{A}_2\cdot\mathbf{r}\right|\psi_i\rangle\right|^2 = 0. \tag{3.31}$$

3.1.5 Introduction of an l-Dependent Phase Factor

In this subsection, we investigate whether the inclusion of a scattering phase for each partial wave channel in the final state may lead to the appearance of a circular dichroism. To this end, we insert a l-dependent phase factor $e^{-i\delta_l}$ in the plane wave expansion as already suggested by Schönhense [1]. thus the final state takes the form

$$\Psi_f(\mathbf{r},\mathbf{k}) = 4\pi\sum_{l=0}^{\infty}\sum_{m=-l}^{l} i^l j_l(kr)e^{-i\delta_l}Y^*_{lm}(\phi_k,\theta_k)Y_{lm}(\phi,\theta) \tag{3.32}$$

the results of the expression $\langle\psi_f\left|\mathbf{A}\cdot\mathbf{r}\right|\psi_i\rangle$ for the primitive polarizations along $\mathbf{x},\mathbf{y},\mathbf{z}$ as given in Equations 3.12, 3.13 and 3.19 are modified by this phase factor as

$$\tilde{M}(k,\theta_k,\phi_k)_{\mathbf{r}} = \begin{cases} 4\pi\left(Y_{0,0}f_0e^{-i\delta_0} - \sqrt{\frac{4}{5}}Y_{2,0}f_2e^{-i\delta_2}\right) & \mathbf{z} \\ 4\pi i f_2\sqrt{\frac{1}{10}}\left(Y_{2,1}e^{-i\delta_2} + Y_{2,-1}e^{-i\delta_2}\right) & \mathbf{y} \\ 4\pi f_2\sqrt{\frac{1}{10}}\left(Y_{2,1}e^{-i\delta_2} - Y_{2,-1}e^{-i\delta_2}\right) & \mathbf{x} \end{cases} \tag{3.33}$$

By the use of the vectors $\mathbf{A}_1$ and $\mathbf{A}_2$ from Equation (3.24) and (3.25) the expression $\langle\psi_f\left|\mathbf{A}_1\cdot\mathbf{r} \pm i\mathbf{A}_2\cdot\mathbf{r}\right|\psi_i\rangle$ can be calculated as before and gives

$$\langle\psi_f\left|\mathbf{r}\mathbf{A}_1 \pm i\mathbf{r}\mathbf{A}_2\right|\psi_i\rangle = e^{\mp i\eta}\left(\pm ie^{-i\delta_2}(M_x\cos(\chi) + M_y\sin(\chi)) + \tilde{M_z}\right). \tag{3.34}$$

Notice that M_x and M_y are the expressions found in Section 3.1.4 without the phase factor. The absolute squared of this can be evaluated using that

$$|x+y|^2 = |x|^2 + |y|^2 + 2\Re(x\bar{y}). \tag{3.35}$$

When calculating

$$I_{CDAD} = \left|\langle\psi_f\left|\mathbf{A}\mathbf{r}_1 - i\mathbf{A}\mathbf{r}_2\right|\psi_i\rangle\right|^2 - \left|\langle\psi_f\left|\mathbf{A}\mathbf{r}_1 + i\mathbf{r}\mathbf{A}_2\right|\psi_i\rangle\right|^2 \tag{3.36}$$

one can identify $y = \left(\pm i e^{-i\delta_2}(M_x \cos(\chi) + M_y \sin(\chi))\right)$ and $x = \tilde{M_z}$ of Equation 3.34 with Equation 3.35 and immediately see that only the $2\Re(x\bar{y})$ terms of each of the expectation values of the expression 3.36 does not vanish. When taking a look at the $2\Re(x\bar{y})$ expression of

$$\Re\left(\mp i e^{\delta_2}(M_x \cos(\chi) + M_y \sin(\chi))\tilde{M_z}\right) = \tag{3.37}$$

we already know from Section 3.1.4 that $(M_x \cos(\chi) + M_y \sin(\chi)) = M_{xy} \in \Re$. Also $Y_{l,0}$ and $R_n \in \Re$. By inserting the corresponding expression of Equation 3.33 for $\tilde{M_z}$ one can rewrite the above described term as

$$= \Re\left(\mp i e^{\delta_2} M_{xy} \frac{(4\pi)^{\frac{3}{2}}}{3}\left(Y_{0,0}R_0 e^{-i\delta_0} - \sqrt{\frac{4}{5}} Y_{2,0} R_2 e^{-i\delta_2}\right)\right) \tag{3.38}$$

which can be brought in the form

$$= \Re\left(\mp i\, M_{xy} \frac{(4\pi)^{\frac{3}{2}}}{3}\left(Y_{0,0}R_0 e^{i(\delta_2-\delta_0)} - \sqrt{\frac{4}{5}} Y_{2,0} R_2\right)\right). \tag{3.39}$$

Here the right term cancels directly due to the real part statement and the i factor in front to

$$= \frac{(4\pi)^{\frac{3}{2}}}{3} M_{xy} Y_{0,0} R_0 \Re\left(\mp i\, e^{i(\delta_2-\delta_0)}\right). \tag{3.40}$$

The absolute difference of the photoemission matrix elements of the right- and left handed polarized vectorfields this leads to

$$I_{CDAD} = \frac{(8\pi)^2}{3} R_0 R_2 \,\sin(\theta_k)\cos(\theta_k)\sin(\delta_2 - \delta_0)(\cos(\chi)\cos(\phi_k) - \sin(\chi)\sin(\phi_k)). \tag{3.41}$$

This result is consistent with Equation (13) from the paper by Schönhense [1] who gives a circular dichroism expression for

$$I_{CDAD} = \left(\frac{d\sigma}{d\Omega}\right)_{RCP} - \left(\frac{d\sigma}{d\Omega}\right)_{LCP} \propto R_0 R_2 \sin(\delta_s - \delta_d)\sin(2\theta_k)\sin(\phi_k). \tag{3.42}$$

When specifying the polarization to $\chi = \frac{\pi}{2}$ and $\eta = 0$, that is the $x \pm iy$ used in in Ref. [1], we obtain from Equation 3.41 the identical result:

$$|\langle \psi_f \left| z + iy \right| \psi_i \rangle|^2 - |\langle \psi_f \left| z - iy \right| \psi_i \rangle|^2 \propto R_0 R_2 \sin(\delta_0 - \delta_2)\sin(2\theta_k)\sin(\phi_k). \tag{3.43}$$

Thus, the introduction of the l-dependent phase factor indeed leads to a CDAD signal. If this is enough to also see the correct CDAD in the intensity distribution of a solid, however, is a different question. An analytic treatment of this problem is not trivial. To test this one could ,however, take an LCAO or Bloch wave ansatz to approximate an initial state, include the phase factor in the final state and evaluate the matrix element. This procedure is described in the next section.

3.2 Photoemission Matrix Element within an LCAO Ansatz

In Section 3.1 an expression for the photoemission matrix element in length gauge of a single $2p_z$ orbital was derived. As shown in Section 3 the circular dichroism effect vanishes for a single $2p_z$ orbital. As discussed in Section 2.5, the CDAD vanishes in velocity gauge for any given system. But does the CDAD effect also vanishes in length gauge for any given system? And if so, can it be reintroduced by the use of the l-dependent phase factors discussed in Section 3?

In this section the photoemission matrix element of a system described by an LCAO initial state will be analyzed. We will later on limit the basis set to $2p_z$ orbitals and stay in the tight binding formalism. In the LCAO ansatz a general molecular orbital can be constructed as

$$\Phi_j(\mathbf{r}) = \sum_{n,\alpha} c^j_{n,\alpha} \phi_{n,\alpha}(\mathbf{r} - \mathbf{R}_n) \tag{3.44}$$

where n is the atom number, α the quantum numbers and j the index of the molecular orbital. Evaluating the photoemission matrix element in length gauge and assuming a plane wave final state one gets:

$$M(\mathbf{k}) = \left\langle e^{i\mathbf{kr}} \left| \mathbf{A} \cdot \mathbf{r} \right| \Phi_j \right\rangle = \sum_{n,\alpha} c^j_{n,\alpha} \int dr^3 e^{-i\mathbf{kr}} \phi_{n,\alpha}(\mathbf{r} - \mathbf{R}_n)(\mathbf{r} \cdot \mathbf{A}). \tag{3.45}$$

By substitution of $\mathbf{r}' = \mathbf{r} - \mathbf{R}_n$ one can split this up to

$$M(\mathbf{k}) = \sum_{n,\alpha} c^j_{n,\alpha} e^{i\mathbf{kR}_n} \left(\underbrace{\int d^3r' e^{-i\mathbf{kr}'} \phi_{n,\alpha}(\mathbf{r}')(\mathbf{r}' \cdot \mathbf{A})}_{\Lambda} + (\mathbf{R}_n \cdot \mathbf{A}) \underbrace{\int dr'^3 e^{-i\mathbf{kr}'} \phi_{n,\alpha}(\mathbf{r}')}_{\mathcal{F}(\phi_{n,\alpha})(\mathbf{k})} \right) \tag{3.46}$$

where $\mathcal{F}(\phi_{n,\alpha})(\mathbf{k})$ is the Fourier transformed $\phi_{n,\alpha}(\mathbf{r}')$ α-atomic orbital of atom n. The expression Λ can be evaluated using the plane wave expansion of Equation 6.12 which can be used to rewrite it as

$$\Lambda(\mathbf{k}) = \sum_{n,\alpha} c^j_{n,\alpha} \sum_{l=0}^{\infty} \sum_{m=-l}^{l} (-i)^l \int d^3r Y^*_{l,m}(\phi, \theta) Y_{l,m}(\phi_k, \theta_k) j_l(kr) \phi_{n,\alpha}(\mathbf{r})(A_x x + A_y y + A_z z) \tag{3.47}$$

Where $Y_{l,m}$ are the spherical harmonics A_n are the components of the polarization vectorfield and x,y,z are Cartesian coordinates which have to be rewritten into spherical coordinates.

Note that this very general expression includes as approximation only an LCAO ansatz so far. By further assuming only $2p_z$ orbitals as a basis of the LCAO, one can make use of the results of 3 and rewrite Equation 3.46 to

$$M(\mathbf{k}) = \sum_{n} c^j_n e^{i\mathbf{kR}_n} \left(\Lambda(\mathbf{k,A}) + (\mathbf{R}_n \cdot \mathbf{A}) \mathcal{F}(\phi_{n,\alpha})(\mathbf{k}) \right) \tag{3.48}$$

where the index α vanished because there is only one type of orbital for each atom. The function *lambda* is given by

$$\Lambda(\mathbf{k},\mathbf{A}) = A_x\lambda_x(\mathbf{k}) + A_y\lambda_y(\mathbf{k}) + A_z\lambda_z(\mathbf{k}) \tag{3.49}$$

and

$$\lambda_x(\mathbf{k}) = 4\pi f_2(k)\sqrt{\frac{1}{10}}(Y_{2,1}(\theta_k,\phi_k) - Y_{2,-1}(\theta_k,\phi_k)) \tag{3.50}$$

$$\lambda_y(\mathbf{k}) = 4\pi i\, f_2(k)\sqrt{\frac{1}{10}}(Y_{2,1}(\theta_k,\phi_k) + Y_{2,-1}(\theta_k,\phi_k)). \tag{3.51}$$

$$\lambda_z(\mathbf{k}) = 4\pi\left(Y_{(0,0)}(\theta_k,\phi_k)f_0(k) - \sqrt{\frac{4}{5}}Y_{(2,0)}(\theta_k,\phi_k)f_2(k)\right). \tag{3.52}$$

Equation 3.48 can be easily modified to include the l-dependent phase factor by simply multiplying $e^{i\delta_l}$ to the radial integral $R_l(k)$. With the use of a tight binding method such as the Hückel model one can calculate the coefficients c_n^j of a specific molecular orbital Φ_j and directly evaluate Equation 3.48. The photoemission matrix element of Equation 3.48 corresponds to the intensity distribution of a photoemission process involving electrons of the molecular orbital Φ_j.

In the next chapter we are going to take a look at a Hückel model based on DFT calculations.Together with Equation 3.48 this model will be used later on to simulate intensity distributions of photoemission processes.

4 Implementation

4.1 Application of the Hückel Model

To implement the ansatz from Chapter 2.4, it is necessary to find values for the hopping parameter introduced in Equation (2.31). The idea of the approach is to fit these values to more accurate results from other methods like DFT (see Section 2.6). For a simple planar hydrocarbon molecule in the Hückel-method the $2p_z$ orbitals are taken into account. These atomic orbitals have a rotational invariance with respect to the z-axis. Assuming spherically symmetric potentials around each nucleus, and planar molecules, (all atoms are aligned in the x-y plane), the hopping parameters from the matrix element of Equation 2.31 are functions of the absolute distance between two C atoms only.

For a molecule consisting of n-carbon atoms, the Hückel matrix is an $n \times n$ matrix. the diagonal elements, the onsite energies, are taken as a parameter, and the off-diagonal elements, the hopping parameters, are parametrized as a polynomial function $t_k(r) = b_0 + b_1 r + b_2 r^2 + ... + b_k r^k$ of order k with respect to the corresponding carbon-carbon bond length. The coefficients of the polynomial are now referred to as $\{b_n\}$. To illustrate how a corresponding Hückel matrix would look like, an example for the benzene molecule is given below.

$$H = \begin{pmatrix} \alpha & t(r_1) & 0 & 0 & 0 & t(r_6) \\ t(r_1) & \alpha & t(r_2) & 0 & 0 & 0 \\ 0 & t(r_2) & \alpha & t(r_3) & 0 & 0 \\ 0 & 0 & t(r_3) & \alpha & p(r_4) & 0 \\ 0 & 0 & 0 & t(r_4) & \alpha & t(r_5) \\ t(r_6) & 0 & 0 & 0 & t(r_5) & \alpha \end{pmatrix} \tag{4.1}$$

While for benzene actually the $r_i = r_j \forall i, j$. The eigenvalues of this matrix correspond to the orbital energies and the corresponding eigenvectors c_i^p are the coefficients for the molecular orbitals as defined in Equation 2.33:

$$\psi_p = \sum_i c_i^p \phi_i. \tag{4.2}$$

Since the onsite elements α are the same in any kind of molecule and always located on the main diagonal of the matrix, they correspond to an energy offset of each eigenvalue and do not influence the eigenvectors. A single fit of the benzene molecule with treating α and t as coefficients was performed and α was fitted to value of -3.459 eV.

This will be a short digression on how such a Hückel matrix can be setup via python. Provided a list of atomic positions this could be implemented as follows:

1. Find the closest neighbor r_{nn} of each atom.
2. Search for all atoms in a radius of $r \in [r_{nn}, r_{nn} \cdot d_f]$ where d_f is a parameter in the below displayed example code refereed to as the ***disanceFactor***.

3. Setup a **1** $n \times n$ matrix and set the diagonal elements as α.

4. Go through each row (row n corresponds to atom n) and add hopping parameters at indices (atoms are numbered by the way they are listed in the atomic position list) of nearest neighbor atoms (found in 2). So if an atom with index 1 has nearest neighbors of $\{3, 48\}$ the first row has hopping parameters t at $H[1,3] = t$,$H[1,4] = t$ and $H[1,5] = t$. Since the matrix has to be symmetric one does the same for the columns.

   Note that when using this scheme to perform fits, the coefficients are parameters or functions of parameters. The python code to setup a Hückel matrix as indicated by Equation 4.1 using a polynomial type function for the hopping parameters is shown below.

```python
#setup a Huckl matrix of the C-atoms given by the atomPos-list ([x,y,z]) with :coeffs beeing the coefficients of the polynomial used as hopping parameter (dependent on bondlength)and distanceFactor beeing the factor in order to determine the nearest neigbors of each atom (between 1 and 1.5 usually).
def setupMatrixByBondDistance(atomPos,distanceFactor,coeffs):
    matrix=np.zeros((len(atomPos),len(atomPos)))
#get distances of nearest neighbor
    radii=getDistancesOfCloseneigbours(atomPos,distanceFactor)

#get indices of nearest neighbor
    connections=getNeigboursInRadius(atomPos,[1,distanceFactor])

    for atom in range(0,len(atomPos)):

  #filling diagonal entries
        matrix[atom,atom]=-3.459

  #filling off-diagonal elements
        for bondType in range(0,len(connections[atom])):
            for i in range(0,len(connections[atom][bondType])):
                matrix[atom,connections[atom][bondType][i]]=-poly5(
radii[atom][i],coeffs[0],coeffs[1],coeffs[2],coeffs[3],coeffs[4],coeffs[5])

    return matrix
```

The function ***getNeigboursInRadius*** in principle returns a list of indices referring to the argument ***atomPos*** where ***atomPos*** is a list of atomic positions as $[[n_{x1}, n_{y1}, n_{z1}], [n_{x2}, n_{y2}, n_{z2}], ...]$.

The function ***getDistancesOfCloseneigbours*** does something very similar, but returns the distances of the nearest neighbor atoms.

Each C-atom contributes 1 p_z-electron to the molecule. There are in total N_C p_z-electrons in the system. with N_C carbon atoms there are N_C $2p_z$ atomic orbitals forming the $n \times n$ Hückel matrix which has exactly N_C eigenfunctions leading to

N_C molecular orbitals. Each molecular orbital can be occupied by 2 electrons. Thus the HOMO orbital (highest occupied orbital) can be found at the $\frac{N_C}{2}$ index of the molecular orbitals (ordered by its eigenvalues from lowest to highest).
The eigenvalues of this matrix $E_i(\{b_n\})$ are then fitted to DFT based results as a least square fit. This is done by minimization of

$$\underbrace{\min}_{\{b_n\}} \left[\sum_i \left(E_i(\{b_n\}) - E_i^{DFT} \right)^2 \right]. \tag{4.3}$$

Since the bond distances of the atoms differ strongly between different molecules, this fit was extended to several molecules in the form of

$$E_{err}(\{E_{i,j}^{DFT}\}) = \sum_{mol,j} \sum_{orbital,i} (E_{i,j}(\{b_n\}) - E_{i,j}^{DFT})^2. \tag{4.4}$$

This error function takes molecules (j) and their molecular orbitals (i) and compares the energies calculated as eigenvalues of the Hückel-matrix $E_{i,j}(\{b_n\})$ to the energies of DFT calculations $E_{i,j}^{DFT}$.

Equation (4.4) is then minimized with a least square fit function. Scipy provides a very efficient routine called ***scipy.optimize.curve-fit***, which was used here.

```
scipy.optimize.curve_fit(f, xdata, ydata)
```

f is here the model function $f(xdata, *params)$ with $xdata$ beeing the argument and the parameter modeling the function. This in the $E_{i,j}(\{b_n\})$ from Equation (4.4) where the x parameter is i, j. Getting this in the format needed, the following was implemented:

```
def combinedModel(x,*xs):
    coeff=[]
    s=[]
    for c in xs:
       coeff.append(c)
    for mol in range(0,len(moleculeIndices)):
        mat=setupMatrixByBondDistance(moleculeCarbs[mol],
   radiusFactos,coeff)
        eW,eV= np.linalg.eigh(mat)
        for i in range(0,numberOfEnergies):
            s.append(eW[int(x[i+numberOfEnergies*mol])])
    return np.array(s)
```

where *xs symbolizes an arbitrary number of coefficients b_n and ***moleculeCarbs*** is a list (of lists) of carbon atom positions
$[\underbrace{[[n_{x1}, n_{y1}, n_{z1}], ..]}_{Mol-1}, \underbrace{[[n_{x1}, n_{y1}, n_{z1}], ..]}_{Mol-2}, ..]$ which is defined outside the function. ***numberOfEnergies*** is also defined outside the function defining the number of orbitals

included for each molecule.

Now making use of the ***scipy.optimize.curve-fit*** routine with the statement

```
best_vals , covar = curve_fit(combinedModel , molEigNumber ,
    molDFTEnergys)
```

, the variables ***best-vals*** contains the optimized parameters of the polynomial for the hopping parameter and ***covar*** the corresponding covariance matrix.

By assuming a quadratic polynomial $t(r) = b_0 + b_1 r + b_2 r^2$ for the hopping parameter, a fit including 38 molecules was performed. The DFT-energies are imported with the *ASE database-environment* [27] from the *Organic Molecule Database* [28] mentioned in Ref. [2] and the included molecules are listed in Table 1 in the appendix. For each molecule 6 molecular energies (HOMO-2,HOMO-1,HOMO, LUMO,LUMO+1,LUMO+2) were incorporated into the fit. The resulting parameters are:

$$\{b_n\} = \{-114.66, +146.73, -48.03\} \tag{4.5}$$

with the corresponding standard deviation of the fit for each parameter

$$\{\sigma_n\} = \{17.63, 25.10, 8.94\} . \tag{4.6}$$

The resulting hopping parameter function with the interpolated bond distances are shown below:

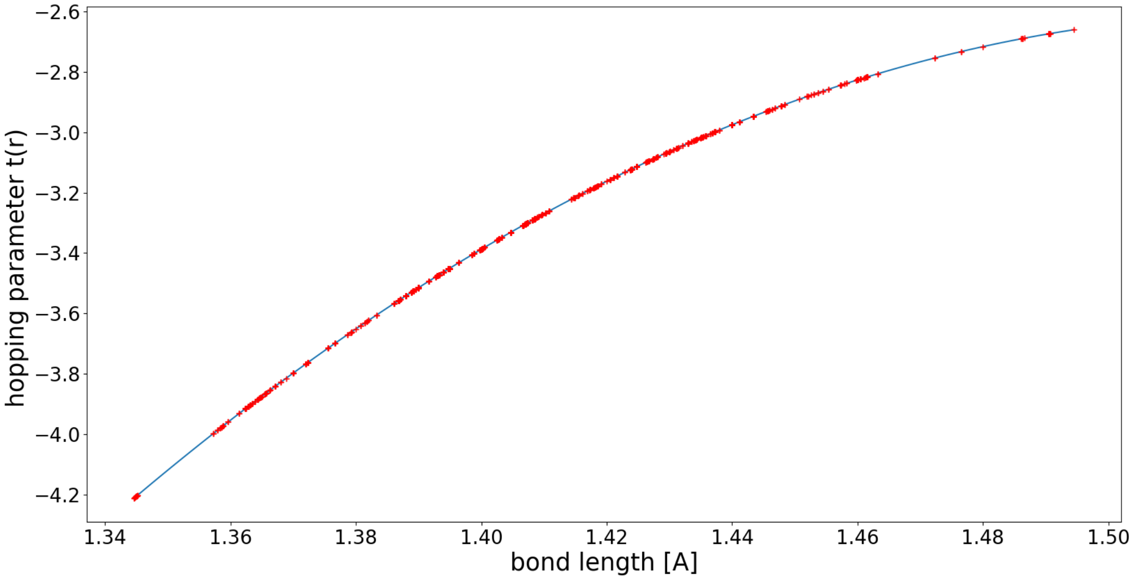

Figure 4.1: The quadratic fit of the hopping parameter of the $2p_z$-$2p_z$ orbitals for distances of the corresponding atoms of $r \in [1.35, 1.50]$Å. The red dots in the plot show the bond distances accounted in the fitting process. (these are not exact values of the hopping parameter but only indicate which bond lengths are taken into account for the fit)

A quadratic fit however cannot resemble a possibly more complex function. Therefore a higher order polynomial is fitted $f(r) = b_1r^5 + b_2r^4 + b_3r^3 + b_4r^2 + b_5r + b_6$. The resulting hopping parameter function in the vicinity of $r \in [1.35, 1.50]$ Å however does not change and a high standard deviation indicates over-fitting. For completeness these results are displayed below.

$$\{b_n\} = \{233.7, -971.0, 959.4, 920.8, -2038.9, 887.0\} \tag{4.7}$$

with the corresponding standard deviation of the fit for each parameter

$$\{\sigma_n\} = \{11300, 84180, 251078, 374472, 279107, 83130\}\,. \tag{4.8}$$

the 5-th order hopping parameter looks like

$$t(r)_{2pz,2pz} = 233.70{\cdot}r^5 - 971.00{\cdot}r^4 + 959.40{\cdot}r^3 + 920.85{\cdot}r^2 - 2038.95{\cdot}r + 886.96. \tag{4.9}$$

One can say that in the vicinity of 1.4 Å the hopping parameter can be approximated as a quadratic function.

To get an idea of the quality of the fit in context of the compared DFT energies and thus the reproduced eigenvalues, the subsequent figure shows the eigenvalues of the Hückel-model together with the hopping parameter of Figure 4.2 and the corresponding DFT-energies.

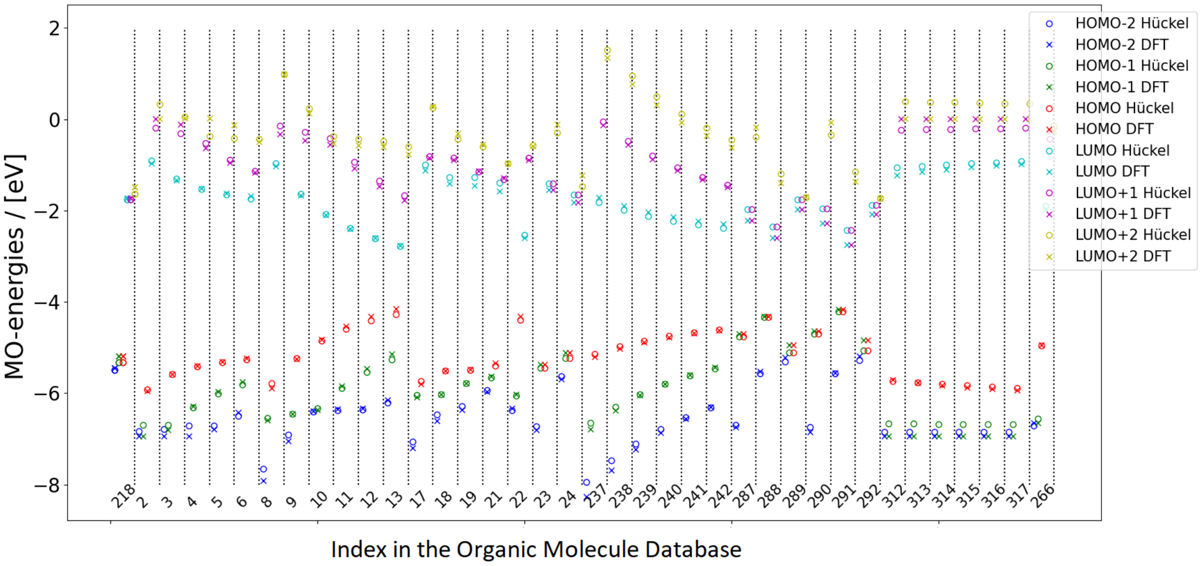

Figure 4.2: Energies of the associated molecular orbital calculated with the Hückel method. The 'o' marker account for the Hückel- and the 'x' marker for DFT-energies imported by the Organic Molecule Database [28]. All markers between two dashed lines are orbital energies of the same molecule ordered from HOMO-2 to LUMO+2. The x-axis labels the molecules by their index in the organic molecule database [28] which can be looked up in Table 1.

The absolute errors of the fitted energies in reference to the DFT-energies from Figure 4.2 are given in the plot below.

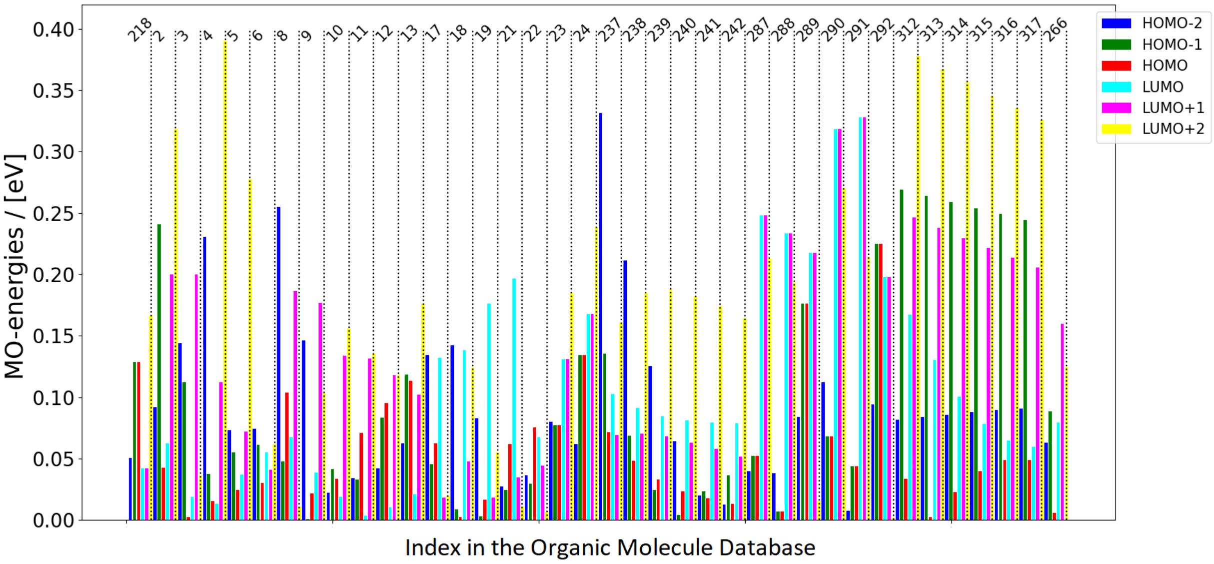

Figure 4.3: Absolute difference of the Hückel energies in comparison to the DFT results shown in Figure 4.2. All bars between two dashed lines are orbital energies of the same molecule ordered from HOMO-2 to LUMO+2. The x-axis labels the molecules by their index in the organic molecule database [28] which can be looked up in Table 1.

The energy eigenvalues of the Hückel method resembles the DFT energies relatively well considering the simplicity of the method. There are ways of improving on the energy eigenvalues such as including a non-diagonal overlap matrix or including next nearest neighbor-interaction. Since it is fitted to another method, it's accuracy can in principle not improve beyond the underlying method. Due to the simple shape of the Hamilton-matrix the Hückel will always do worse in approximating energies. One can say that predicting molecular orbital energies is not a strength of the Hückel model. The approximation of the molecular orbitals however comes really close to the ones calculated by DFT. This will be discussed in the subsequent section.

4.2 Overlap of Hückel- and DFT Molecular Orbitals

From the fit described above, the eigenvectors of the matrix of Equation 4.1 describe the coefficients of the molecular orbitals. The molecular orbitals obtained by the Hückel-method are, as already shown in Equation 4.2, given by

$$|\Psi_j\rangle = \sum_i c_i^j \, |\phi_i\rangle. \tag{4.10}$$

As atomic orbitals here the $2p_z$ hydrogen orbitals with an atomic charge corresponding to the effective nuclei charge (Slater's rule) of carbon has been taken to be $Z_{\text{eff}} = 3.28$.

The program setting up the Hückel matrix shown in Section 4.1 is now used together with the fitted hopping parameters of Equation 4.5 to construct Hückel molecular orbitals for arbitrary planar hydrocarbon molecule molecules from scratch. The orbitals are saved in the cube-format and can be visualized via VESTA [29]. An example of the LUMO and HOMO orbitals of bisanthene simulated with this method is given below:

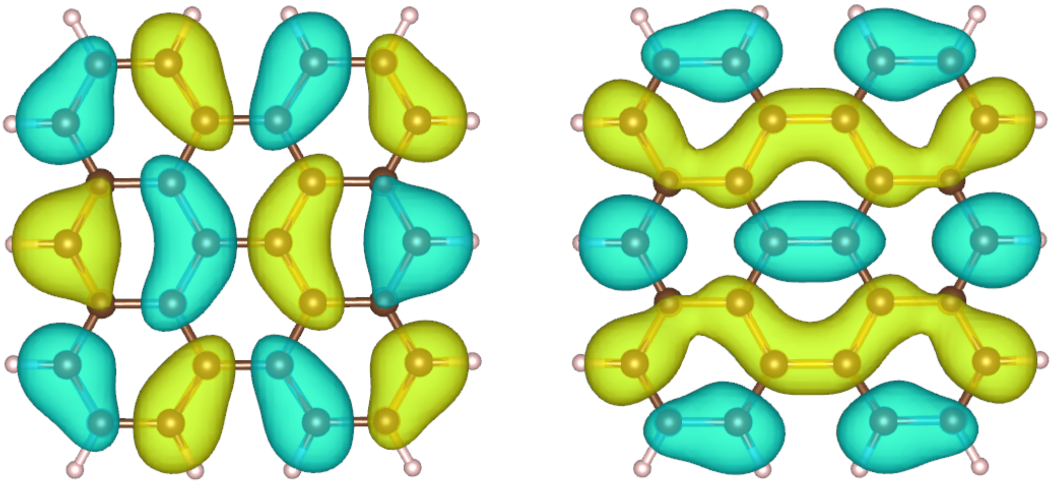

Figure 4.4: HOMO (left) and LUMO (right) of bisanthene simulated with the Hückel model of the fitted hopping parameters given in Equation 4.5.

To give a quantitative analysis of the so obtained wavefunctions, the molecular orbitals of the Hückel-model are compared with the ones obtained by DTF with the B3LYP xc-functional calculations. To this end, an overlap integral is performed by

$$I[\phi_1, \phi_2] = \int_V \phi_1(\vec{r})\phi_2(\vec{r}) \tag{4.11}$$

where V is the volume of the simulated region, ϕ_1 refers to the Hückel molecular orbital and ϕ_2 to the DFT molecular orbital. Since both wavefunctions are normalized, the corresponding overlap integral $I[\phi_1, \phi_2] \leq 1$. Therefore both wavefunctions have to be exactly on the grid/location of the simulated area. The closer this overlap is to 1, the more alike these two wavefunctions are, while an overlap of 0 would conclude an orthogonal setting.

One way to visualize the orbitals is to make a cut in the x,y plane. The subsequent image (Figure 4.5) gives an example for this and shows a cut in the z axis at about 0.9 Å above the x,y symmetry plane for the HOMO orbital of benzene.

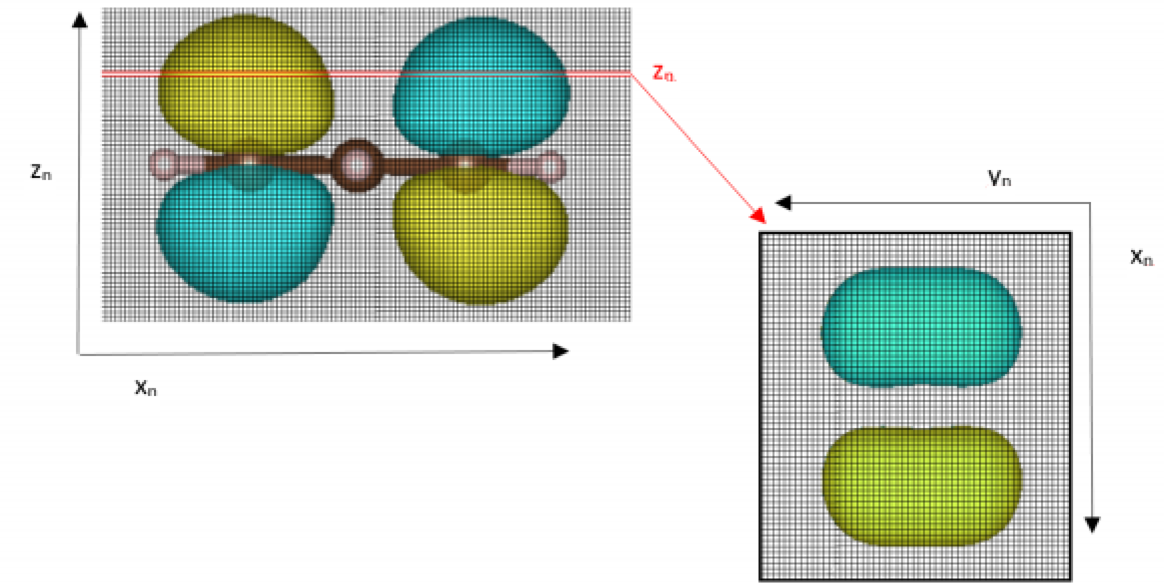

Figure 4.5: Example cut of the HOMO orbital in the x/y-plane of benzene at 0.9 Å above the x,y symmetry plane

The following figures show cuts in this plane for the molecular HOMO orbital of sexiphenyl from DFT and Hückel methods.

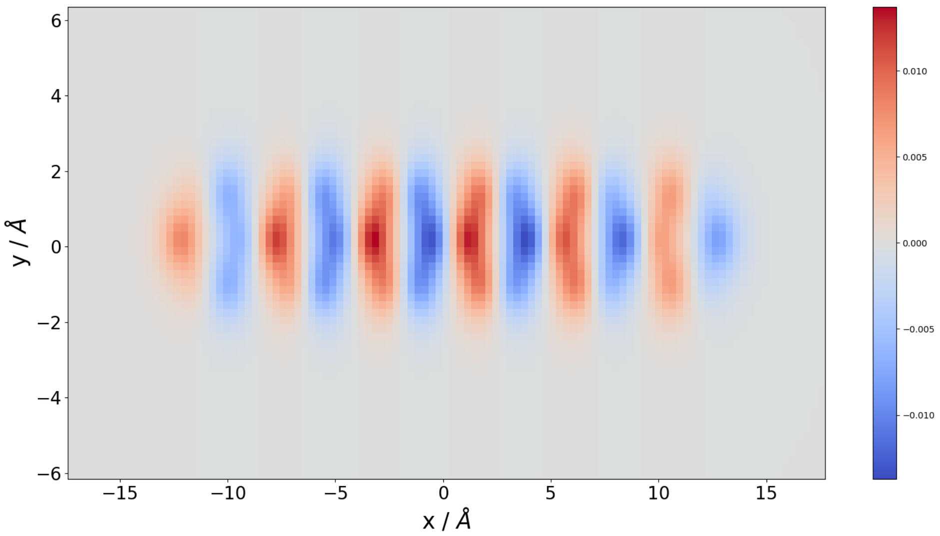

Figure 4.6: Molecular HOMO orbital of sexiphenyl from DFT/B3LYP calculations at 1 Å above the x,y symmetry plane

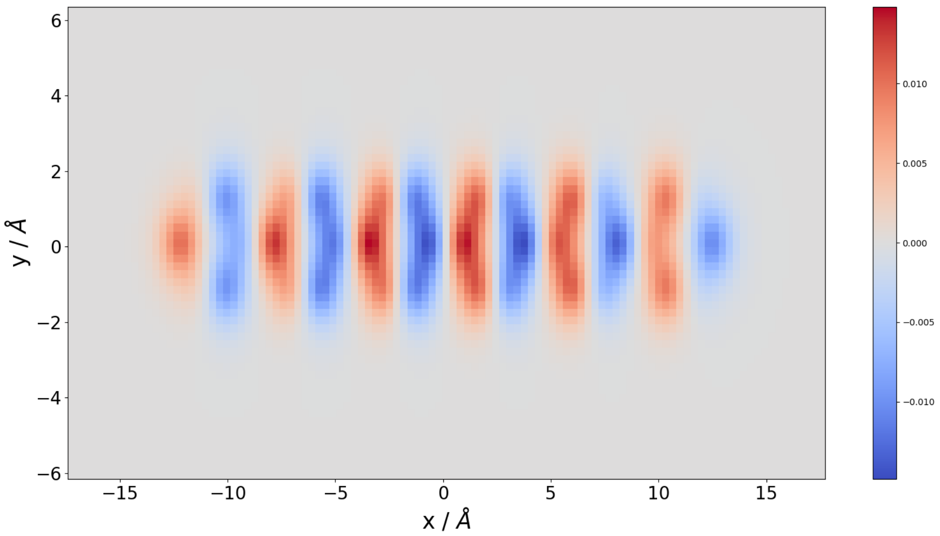

Figure 4.7: Molecular HOMO orbital of sexiphenyl from TB calculations at 1 Å above the x,y symmetry plane

The corresponding integrand of the overlap $(\phi_1 \cdot \phi_2)$ is shown below in the exact same plane. The overlap strongly depends on the effective charge Z_{eff} chosen. The one determined by Slater's rule $Z_{\text{eff}} = 3.26$ provides a starting point for an optimization of this parameter. The maximum of the overlap of the HOMO orbital of the DFT and Hückel model is reached for an effective charge of $Z_{\text{eff}} = 1.48$.

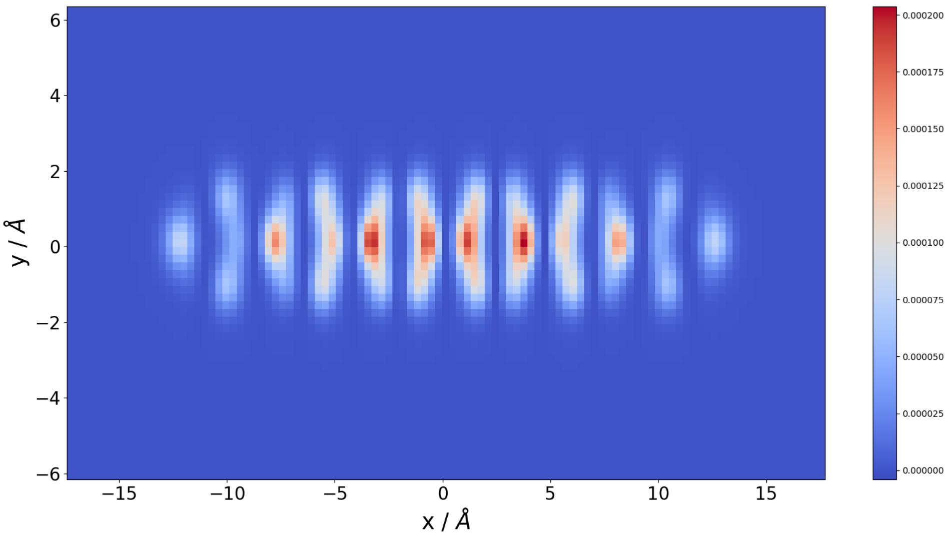

Figure 4.8: Molecular HOMO orbital overlap of sexiphenyl at at 1 Å above the x,y symmetry plane

The corresponding overlap integral gives $I[\phi_1, \phi_2] = 0.944$ which signifies a noticeable similarity. Different overlap integrals are displayed below. The LUMO+2 orbital is excluded here because the Hückel model shows the LUMO+3 instead.

DFT: Hückel:	LUMO+1	LUMO	HOMO	HOMO-1	HOMO-2
$LUMO+1$	0.929	0.049	-0.014	-0.075	-0.082
$LUMO$	-0.071	0.924	0.105	-0.082	-0.006
$HOMO$	0.004	-0.129	0.944	-0.034	-0.041
$HOMO-1$	0.089	0.073	0.072	0.940	0.052
$HOMO-2$	-0.063	-0.007	-0.034	0.084	0.937

Some ideally orthogonal orbitals ,like $\langle HOMO_{\text{Hückel}}|LUMO_{DFT}\rangle$ or $\langle HOMO_{DFT}|LUMO_{\text{Hückel}}\rangle$ show a noticeable overlap. One can however clearly distinguish orthogonality of different orbitals of the different methods. The DFT and Hückel molecular orbitals fulfill among themselves the relation $I[\phi_i, \phi_j] = \delta_{i,j}$

In conclusion one can say that the Hückel model gives a reasonable approximation of the molecular orbitals. Its fast setup allows for very efficient calculation of even big molecules or systems. Using Hückel molecular orbitals as initial states could also be used to evaluate photoemission matrix elements of the Fermi's golden rule expression discussed in Section 2.1. Thus one could relatively easy obtain an ARPES simulation. We will come back to this idea later in Section 3.2.

An already existing code using the Slater-Koster formalism discussed in Section 2.4 is *chinook* [16]. In the next Chapter we will take a look at photoemission simulations of graphene using this package.

4.3 TB Simulation with Chinook

Chinook [16] is a python package, which employs a tight binding ansatz to calculate the band structure for periodic materials and simulates ARPES intensities within the one step model of photoemission. One can model a system using multiple orbitals per atom in a very efficient manner. It is also possible to include different polarizations for the ARPES simulation. In principle it uses Fermi's golden rule expression of Section 2.1 to do so. We will take a look at the π-band of graphene for different polarizations here. This chapter only shows some example scripts demonstrating how to run chinook. The corresponding results are presented in the next Section 4.3.1.

To start off, one defines the lattice vectors and the positions of the atoms in the primitive unit cell as described in Section 2.3.

```
#lattice vectors
a = 2.47 #in bhor
avec = np.array([[a,0.0,0.0],
                 [-a*0.5,a*(3**0.5)/2,0.0],
                 [0.0          ,  0.0    ,10.0]])

#atomic positions
p1 = np.array([0.0,0.0,0.0])
p2 = np.array([a*(1/3),a*2/3,0.0 ])
```

Next the *basis-args* are defined, specifying the type of atoms, which atom belongs to which positions, the orbitals included for each atom of the calculation and whether or not to include spin polarization. In this case only $2p_z$ orbitals are included for the calculation which are denoted as '21z'.

```
spin_args = {'bool':False}

basis_args = { 'atoms':[0,0],
            'Z':{0:6},
            'pos':[p1,p2],
            'orbs':[['21z'],['21z']],
            'spin':spin_args}
```

Using these settings, the Hamiltonian can be constructed by defining the onsite-energies `ep` and the hopping parameter `HP`. The object `H-list` below defines the Hamilton matrix. The first two elements of each list account for the basis indices of the orbitals. This means the i, j indices of $H_{i,j} = \langle \phi_i | H | \phi_j \rangle$. The remaining elements contain the vector connecting the atoms the two orbitals belong to in (x,y,z) form. These are nothing else than the nearest neighbor vectors from Equation (2.19). For the nearest neighbor hopping parameter `t`, we make use of the parametrization discussed in Section 4.1 leading to a value of $t = -3.164eV$ when setting the C-C distance to $r = 1.42$ Å.

Let us take a look at the example [0,0, 0,0,0 ,`ep`]. The first two elements of the list (orange) indicate the orbital index. In the `basis-args` instance of the script shown above, two orbitals were included, both of $2p_z$ type. In this example this refers to $H_{0,0} = \langle \phi_0 | H | \phi_0 \rangle$. The next 3 elements (marked yellow) denote the Cartesian coordinates of the vector connecting the two respective orbitals. In the example this is $(x = 0, y = 0, z = 0)$ since it is the same orbital and there is no spatial difference. The last quantity (`ep`) is the associated value which is the onsite energy in this case.

For two included orbitals and three nearest neighbors of each atom, The Hamilton-matrix can be setup with five parameters. There are two onsite elements and three nearest neighbor hopping parameters. In principle two parameters would be sufficient here, but the onsite elements as well as the nearest neighbor hopping parameter for each orbital have to be included explicitly.

```
#Hamilton
ep   =  0      #onsite energy
HP   =  -3.164 #hopping parameter in eV

H_list=[[0,0,0,0,0,ep],
        [1,1,0,0,0,ep],
        [0,1, 0.0 ,  a/(3**0.5)   , 0.0  ,HP],
        [0,1, a/2 , -a/(2*3**0.5) , 0.0  ,HP],
        [0,1,-a/2 , -a/(2*3**0.5) , 0.0  ,HP]]

hamiltonian_args = {'type':'list',
    'list':H_list,
    'cutoff':0.6*a,
    'renorm':1.0,
    'offset':0.0,
    'tol':1E-4,
    'avec':avec,
    'spin':spin_args}
```

The variable `cutoff` refers to the cutoff hopping distance (Which atoms to include as nearest neighbors).

To plot a band structure, a k-path has to be defined. This is done in reduced coordinates. One can later take a look at the band structure along this path. Of special interest is the region around the K-points. Therefore as k-path we defined a line through the K-point perpendicular to the vector pointing from Γ to the K-point. This is indicated with the blue line in the below figure.

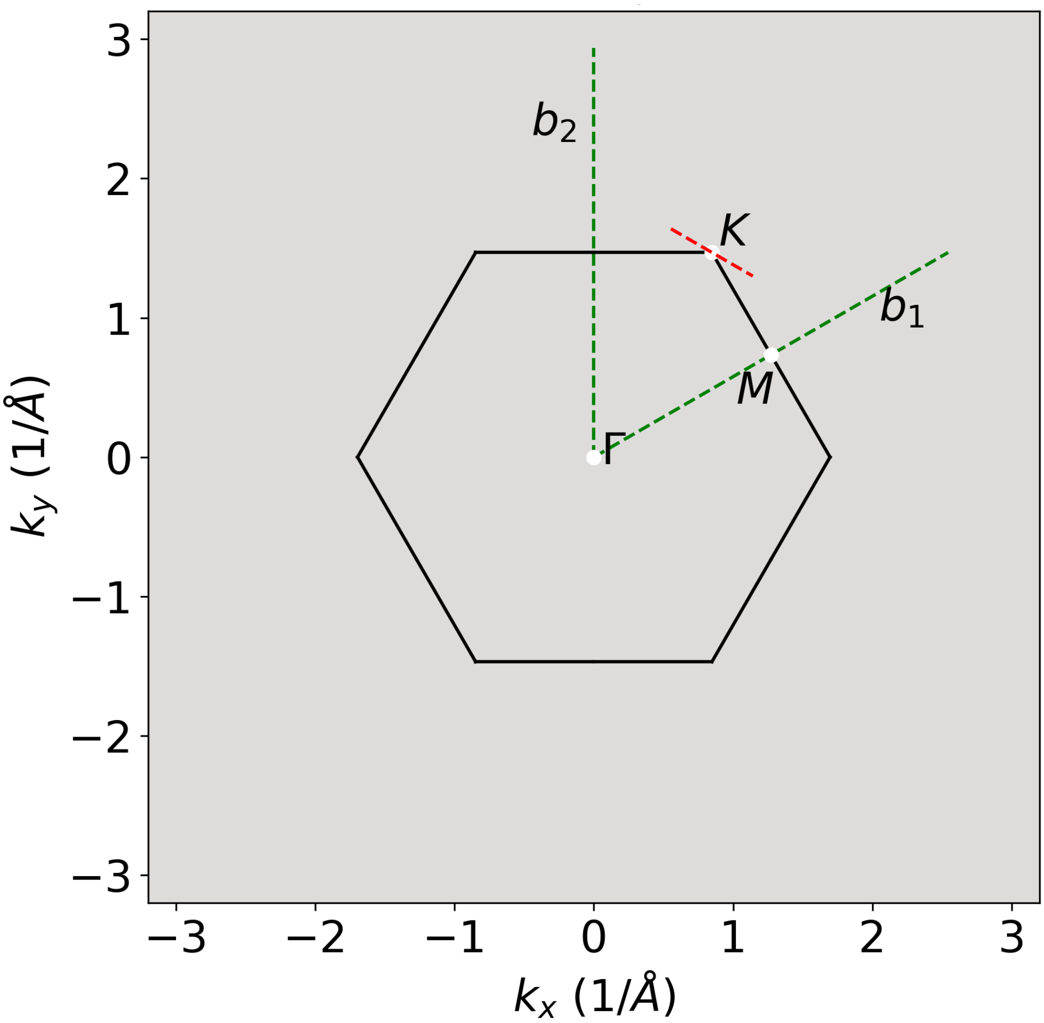

Figure 4.9: First Brillouin zone of graphene indicating the K,Γ and M point as well as the reciprocal lattice vectors $\mathbf{b}_1$ and $\mathbf{b}_2$ and the k_{path} spanned by the two points K_1 and K_2 indicated by the red dotted line.

```
#the points around the K-point from octopus
K1_oct_red=[0.21786328 , 0.44880339,0]
K2_oct_red=[0.44880339 , 0.21786328,0]
```

With `k1-oct-red` and `k2-oct-red` defining the k-path indicated in Figure 4.9 as K_1 and K_2, given in reduced coordinates. They are later also used in the TDDFT-code called *Octopus*.

```
#define Path for bandstructure plot
momentum_args = {'type':'F',
    'avec':avec,
    'grain':100,
    'pts':[K1_oct_red,K2_oct_red],
    'labels':['K1','K2']}
```

To work with this now a few objects have to be initialized

```
###create necessary objects and solve TB for given Momenta and plot
    bandstructure
basis = build_lib.gen_basis(basis_args)
kpath = build_lib.gen_K(momentum_args)
TB = build_lib.gen_TB(basis,hamiltonian_args,kpath)
TB.solve_H()
```

Implementing this, one can take a look at the band structure of the k-path defined above. The Subsequent plot shows the Dirac-cone of graphene.

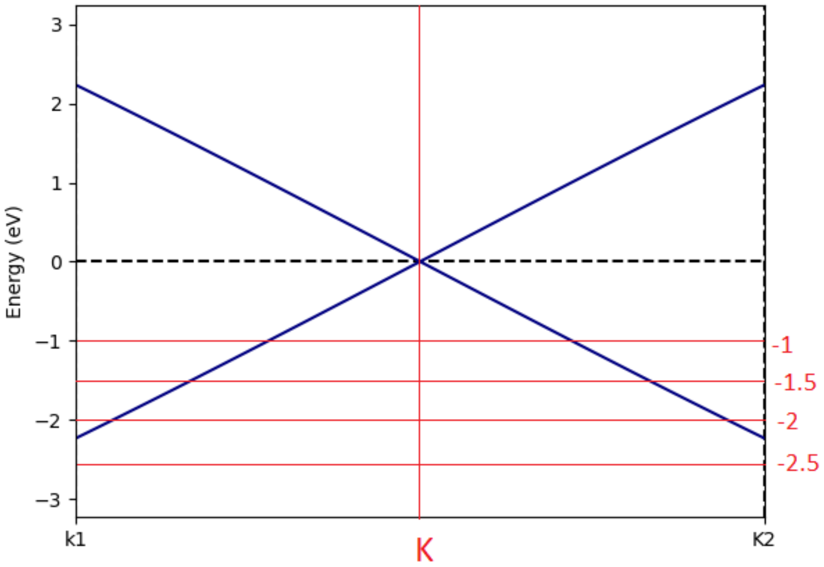

Figure 4.10: Band structure of graphene including $2p_z$ orbitals for a k-path between the points $[0.218, 0.449, 0]$ and $[0.449, 0.218, 0]$ (given in reduced coordinates) with the dashed line indicating the Fermi energy. Energies from -1 to -2.5 eV are indicated for comparisons in Section 4.3.1.

In the above plot the Fermi energy is $E_F = 0$ eV. In comparison to this, one can take a look at Figure 4.11 showing the bandstructure of graphene for a k-point path $M - K - \Gamma - K - M$ simulated in a DFT calculation performed via the *Octopus* code (see [12]) using a LDA functional and the pseudopotential set *hgh-lda*.

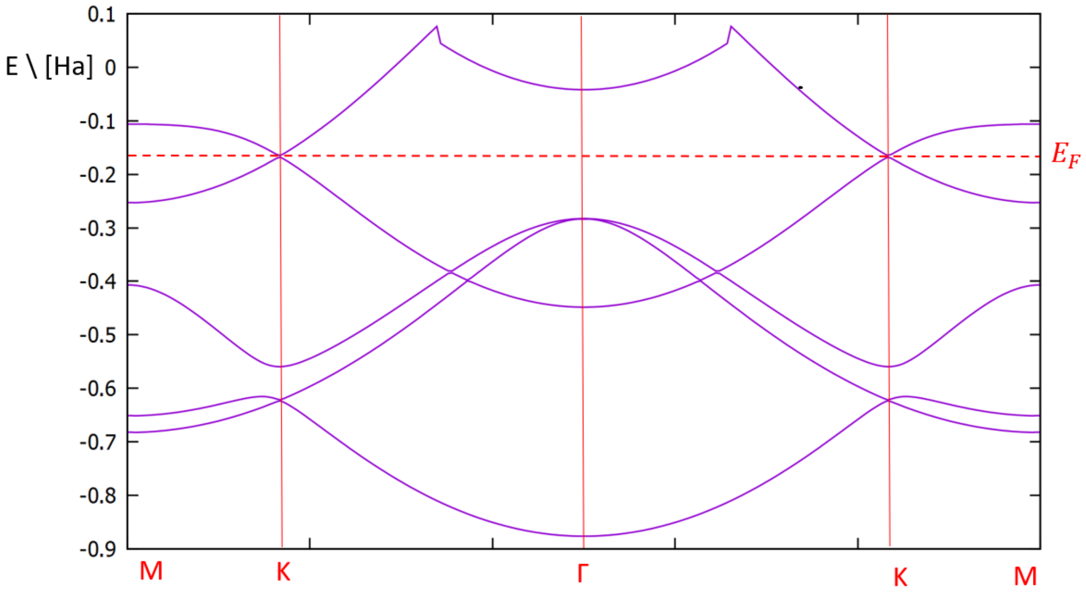

Figure 4.11: Bandstructure of graphene along a k-point path $M - K - \Gamma - K - M$ see figure: 2.4

4.3.1 ARPES-Simulations in Chinook

Based on the tight-binding description of a single-layer graphene introduced in the previous section, we will now demonstrate how ARPES intensity maps can be obtained from *chinook*.To this end *chinook* provides an object called *arpes-lib.experiment* to evaluate the given structure in terms of the ARPES cross section. In principle *chinook* calculates Fermi's golden rule expression (see Section 2.1) in the real space representation with a plane wave final state which is expanded in spherical-harmonics (see Section 3 later).

The *arpes-lib.experiment* object does take care of this. It is defined the following way:

```
arpes_args_rh={'cube':{'X':[xmin,xmax,dk],'Y':[ymin,ymax,dk],'kz':0.0,'E':[Eb[0],Eb[nE-1],nE]},     #domain of interest to solve TB
            'SE':['constant',0.1],    #self energy -> broadening of bands
            'hv': hnu,    #photon energy
            'pol':np.array([np.sqrt(1/2),np.sqrt(1/2),0]),  # polariation vector of ligth for ARPES-setting
            'resolution':{'E':0.08,'k':0.04},  # 'k':0.045
            'T':-1.0, # don't involve themperature
```

```
            'rad_type':'slater'}   # radial part of the wave
    function

experiment_rh = arpes_lib.experiment(TB,arpes_args_rh)
#evaluate the cross section
experiment_rh.datacube()

#generate an image of the band structure at energy Eb[i]
Imap_rh,Imap_resolution_rh,axes_rh = experiment_rh.spectral(
    ARPES_dict=arpes_args_rh,slice_select=('E', Eb[i]),plot_bands=
    False);
```

The script above generates an intensity distribution of a constant binding energy momentum map based on the tight-binding model defined in the previous section. The variable `'pol':` defines the polarization of the incident light beam. The polarization direction is indicated in the upper right corner as a little arrow. Retrospectively a few lines and labels to indicate the Brillouin zone, some important points and the reciprocal lattice vectors were added. Of interest are simulations of the same energy for different polarizations of the incident light.

The polarization of the subsequent plots was chosen as $\mathbf{A} = [\frac{1}{\sqrt{2}}, \frac{1}{\sqrt{2}}, 0]$ which specifies a linear polarization in the xy plane. Alternatively any other polarization direction could have been used. The subsequent content should explain the process as well as some general properties of the one step model of photoemission process. Some constant binding energy momentum maps are shown for different binding energies. These energies are indicated in 4.10.

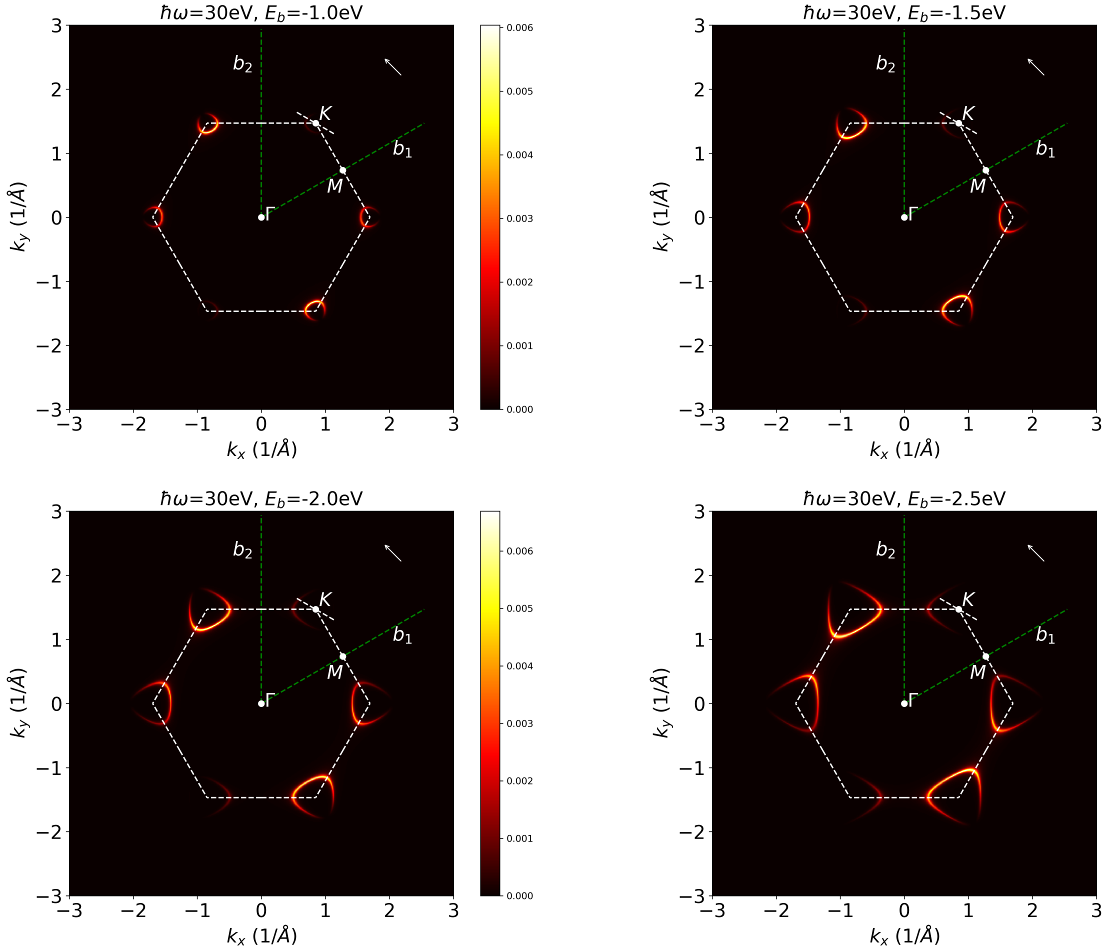

Figure 4.12: Photoemission intensity maps of single layer graphene at various constant initial energies -1.0, -1.5, -2.0 and -2.5 eV below the Fermi edge for polarized light of $\mathbf{A} = [-\frac{1}{\sqrt{2}}, \frac{1}{\sqrt{2}}, 0]$.

When taking a look at a different polarization $\mathbf{A} = [\frac{1}{\sqrt{2}}, \frac{1}{\sqrt{2}}, 0]$ in the xy plane, perpendicular to the one before one gets different intensities for the band-maps. In Section 2.5 an expression for the photoemission intensity has been derived (Equation 2.76) which states that in velocity gauge the expectation value is proportional to the factor $|\mathbf{A} \cdot \mathbf{k}|^2$. As a consequence the intensity is expected to vanish in the directions perpendicular to the polarization direction $\mathbf{A}$. This can indeed be seen in the Figures 4.13 .

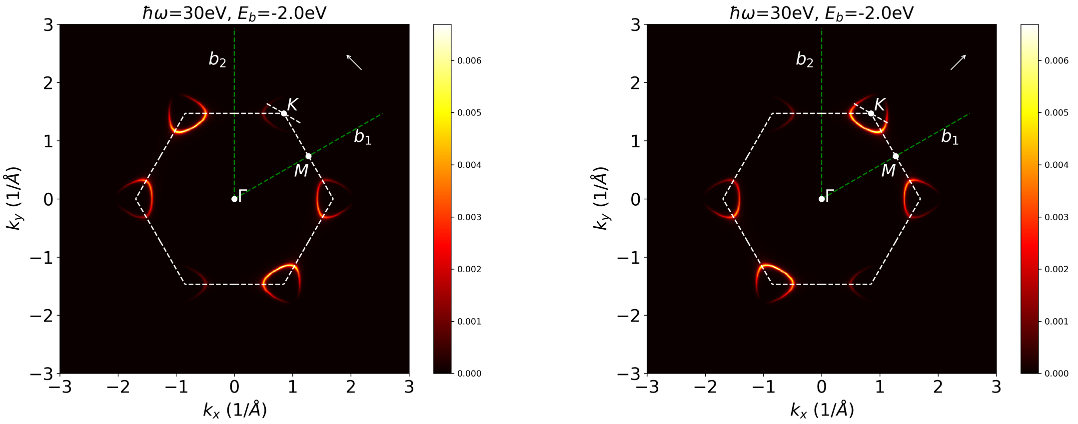

Figure 4.13: Constant binding energy momentum map for single-layer graphene at energy -2.0 eV below the Fermi edge, for light polarized as $\mathbf{A}_1 = [-\frac{1}{\sqrt{2}}, \frac{1}{\sqrt{2}}, 0]$ (left) and $\mathbf{A}_2 = [\frac{1}{\sqrt{2}}, \frac{1}{\sqrt{2}}, 0]$ (right).

The difference of the simulations with perpendicular polarization directions is known as linear dichroism map. Such a plot for the two different polarization directions $\mathbf{A} = [-\frac{1}{\sqrt{2}}, \frac{1}{\sqrt{2}}, 0]$ and $\mathbf{A} = [\frac{1}{\sqrt{2}}, \frac{1}{\sqrt{2}}, 0]$ is shown below.

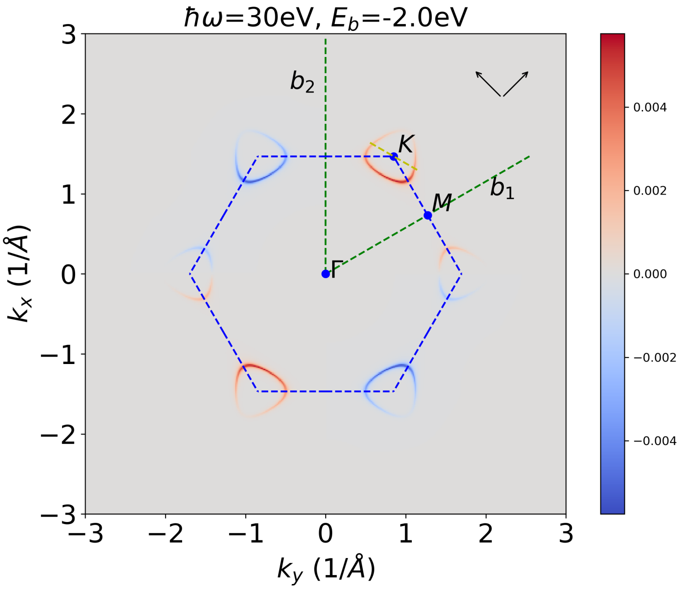

Figure 4.14: Linear dichroism map of single layer graphene for $\mathbf{A}_1 = [-\frac{1}{\sqrt{2}}, \frac{1}{\sqrt{2}}, 0]$ and $\mathbf{A}_2 = [\frac{1}{\sqrt{2}}, \frac{1}{\sqrt{2}}, 0]$ polarized light at an energy of 2.0eV below the Fermi edge.

Another form of dichroism maps discussed in the literature [14] are circular dichroism maps. They display the difference in ARPES intensity maps obtained from right-handed and left-handed circularly polarized light. This effect is also known as circular dichroism in the angular distribution (CDAD) [1]. In principle, chinook can also simulate such CDAD maps by specifying an appropriate polarization vector. This can for instance be polarization vectors $\mathbf{A}_L = [1, i, 0]$ for left-handed and $\mathbf{A}_R = [1, -i, 0]$ for right handed polarized light. As discussed in Section 2.5, with a plane-wave final state and a matrix element in the velocity gauge, the CDAD signal is expected to vanish $(|\mathbf{A}_L \cdot \mathbf{k}|^2 - |\mathbf{A}_R \cdot \mathbf{k}|^2) = 0$. However chinook calculates the matrix element in length gauge (as can be looked up in [16]). So an investigation on how chinook performs on this CDAD effect could tell us about the difference of the matrix element in length gauge in comparison to the velocity gauge. For later comparison with the TDDFT code *octopus*, we are particularly interested in the CDAD effect close to the Fermi-edge for a k-path through the K-point (indicated in Figure 4.9). To compare TDDFT results to TB-calculations in *Chinook* it is useful to make cuts along k-paths in these band-maps and compare them instead of the entire BZ. Unfortunately, *Chinook* has no implemented method for arbitrary cuts in the k-space. A method to overcome this limitation is explained in the subsequent section.

4.3.2 Interpolating Cuts on the Band Maps

The idea is very simple: *Chinook* calculates constant energy momentum maps in the first-BZ on a regular grid on the k-space. One uses an interpolation algorithm to calculate an arbitrary path in this 3-d intensity data cube $(I(k_x, k_y, E_b))$. This is shown in the subsequent code. The variable `Imap-rh` in the code is the 3-d array saving the band maps. The interpolation was done using the `RegularGridInterpolator` from scipy.

```python
from scipy.interpolate import RegularGridInterpolator as rgi
```

```python
#define slices of the dispersion, NOTE: energySlice[j] where j defines the index of the corresponding ernergy
energySlice_path=np.zeros((dE_int,nPath,3))
#do some transpose magic to make it work (interpolation somehow swaps x and y axis..?)
transposedImag=np.zeros((dk,dk,dE))
for i in range(0,dE):
    transposedImag[:,:,i]=np.transpose(Imap_rh[:,:,i])


sliceCutter_rh=rgi((kx,ky,Eb),transposedImag[:,:,:],method='linear')
#interpolate intensities from (data) on the grid (kx,ky) at energy E=energyGrid[j] , for the path (kx_path,ky_path)
interpolatedData=np.zeros((dE_int,nPath))
for j in range(0,dE_int):
```

```
    #make list of kx,ky path for certan energy
    k_path=np.array([[kx_path[i],ky_path[i],energyGrid[j]]for i in range(0,len(kx_path))])
    #save in array [[k-path energy j=1 ],[k-path energy j=2],....]
    energySlice_path[j]=(k_path)
    #print(j/dE_int) #print percent of done work

    interpolatedData[j]=sliceCutter_rh(energySlice_path[j])
```

As k-path, the cut along the following points

$$\mathbf{K}_1 = (0.2179, 0.4488, 0)\ ,\ \mathbf{K}_2 = (0.4488, 0.2179, 0) \tag{4.12}$$

was chosen (given in reduced coordinates). It is a cut trough the K-point shown in Figure 4.9. The band structure along this path is given below. The k-path is also indicated in the intensity map directly by a yellow dashed line.

We want to compare linear dichroism maps as well as circular dichroism maps later on. The K-point is located at $\mathbf{K} = [\cos(60°), \sin(60°), 0]$. Choosing the polarization vectors to be oriented ±45° to the K-point, one can expect the linear dichroism map to change sign along the chosen k-path. This should in theory be absolutely antisymmetric with the intensity difference at the K-point being exactly 0. Thus the chosen polarizations should provide a well comparable linear dichroism map. The polarization vectors where chosen as $\mathbf{A}_1 = [\cos(15°), \sin(15°), 0]$ and $\mathbf{A}_2 = [\cos(105°), \sin(105°), 0]$.

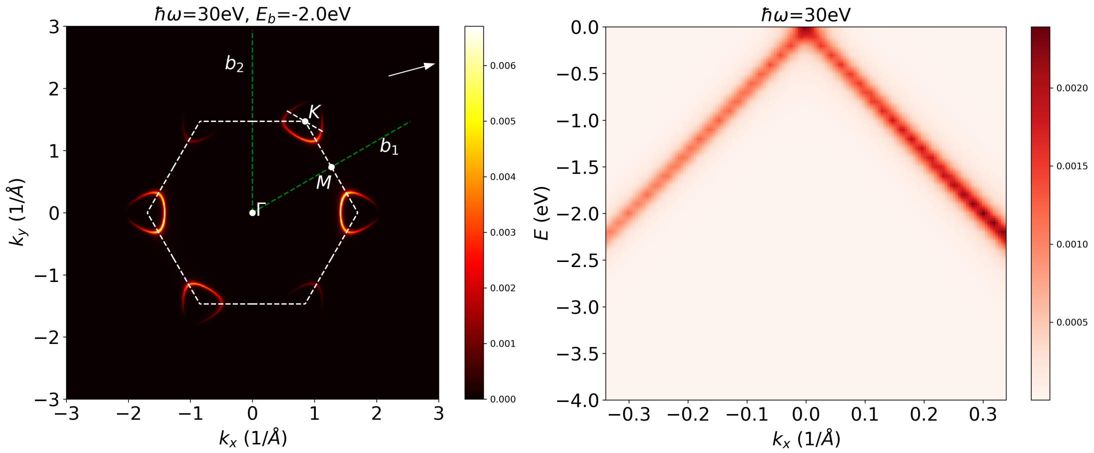

Figure 4.15: Left panel: Bandmap of graphene for E=-2.0 eV with dashed yellow line indicating the k-path of the band structure in the second plot. Right panel: Band structure of cut through the Dirac cone below the Fermi level. The polarization is $\mathbf{A} = [\cos(15°), \sin(15°), 0]$ which the little arrow on the upper right corner of the left figure indicates.

By taking a look at the perpendicular polarization of the same path, one can observe the following intensities:

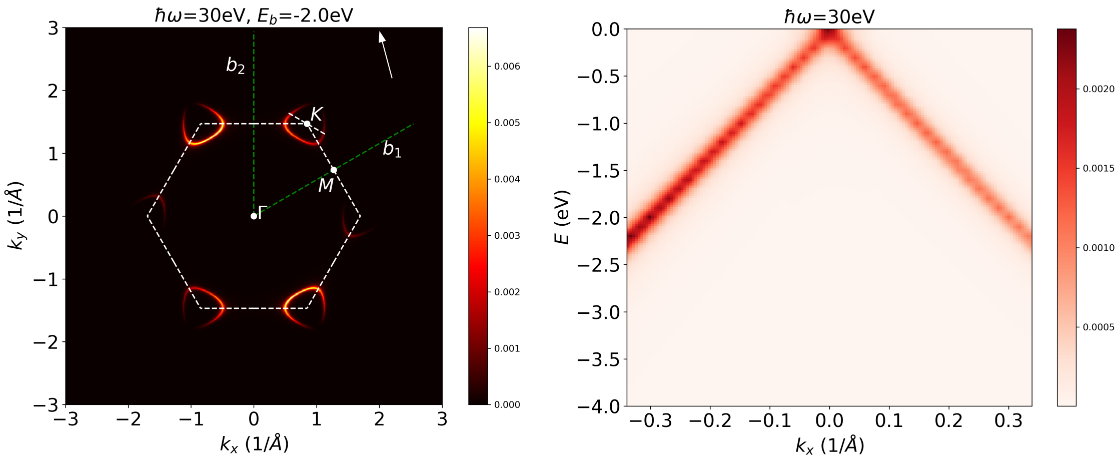

Figure 4.16: Left panel: Bandmap of graphene for E=-2.0 eV with dashed yellow line indicating the k-path of the band structure in the second plot. Right panel: Band structure of cut through the Dirac cone below the Fermi level. The polarization is $\mathbf{A} = [\cos(105°), \sin(105°), 0]$ which the little arrow on the upper right corner of the left figure indicates.

The difference can be visualized by making a linear dichroism map of the two polarizations.

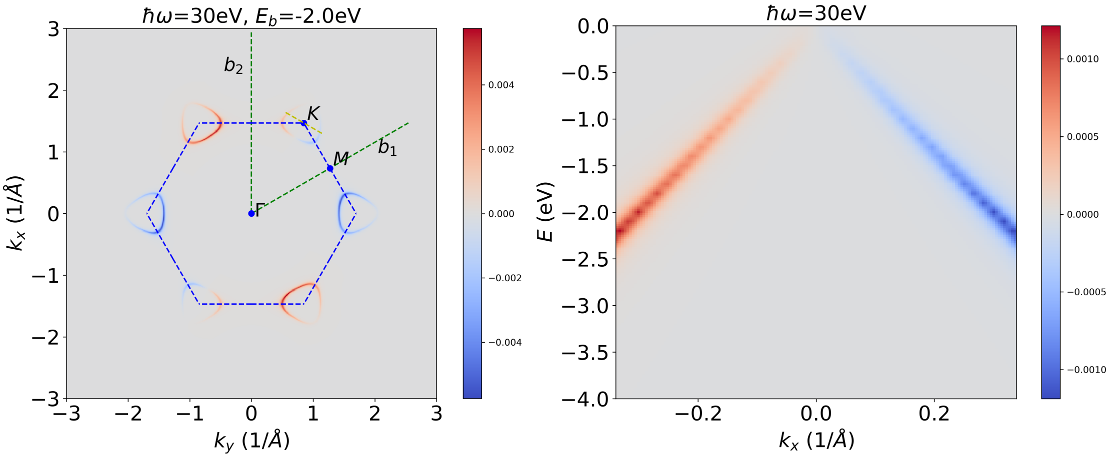

Figure 4.17: Left panel: Dichroism momentum map of graphene for E=-2.0 eV with dashed yellow line indicating the k-path of the band structure in the second plot. Right panel: Dichroism APRES momentum map of cut through the Dirac cone below the Fermi level. The polarization of the two simulations is at $\mathbf{A}_1 = [\cos(105°), \sin(105°), 0]$ and $\mathbf{A}_2 = [\cos(15°), \sin(15°), 0]$ .The little arrows on the upper right corner of the left figure indicate these.

Now we evaluate the circular dichroism in graphene as obtained from chinook. The region of interest will again be the one around the K-point. Circularly polarized light can be described by the use of imaginary numbers in the polarization vector, as described in Section 2.7.2. The following images show simulations of ARPES experiments for x-y circularly polarized light with different handedness and their dichroism map, the so called circular-dichroism map.

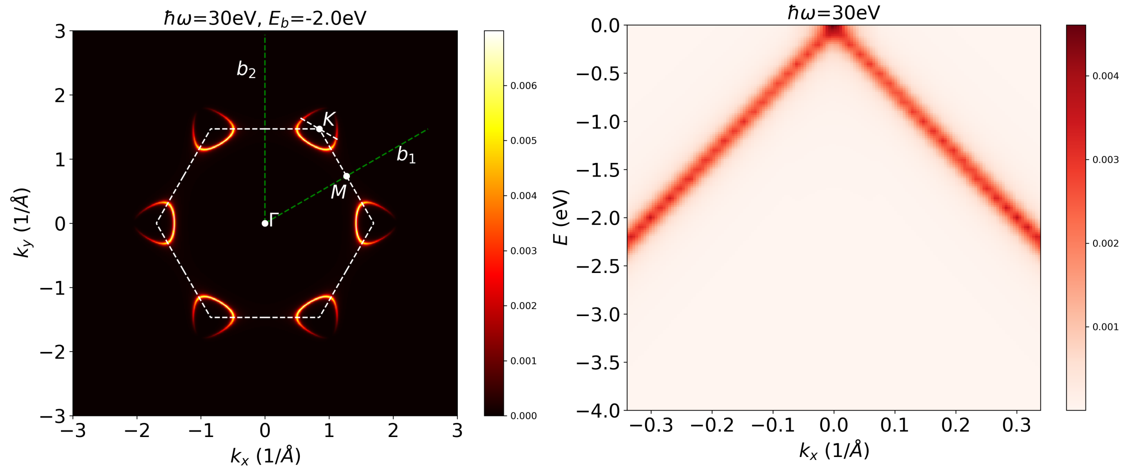

Figure 4.18: Left panel: Momentum map of graphene for E=-2.0 eV with dashed yellow line indicating the k-path of the bandmap in the right panel. Right panel: Bandmap for a cut through the Dirac cone below the Fermi level. The polarization is $\mathbf{A}_2 = [1, i, 0]$ marking right-handed polarized light.

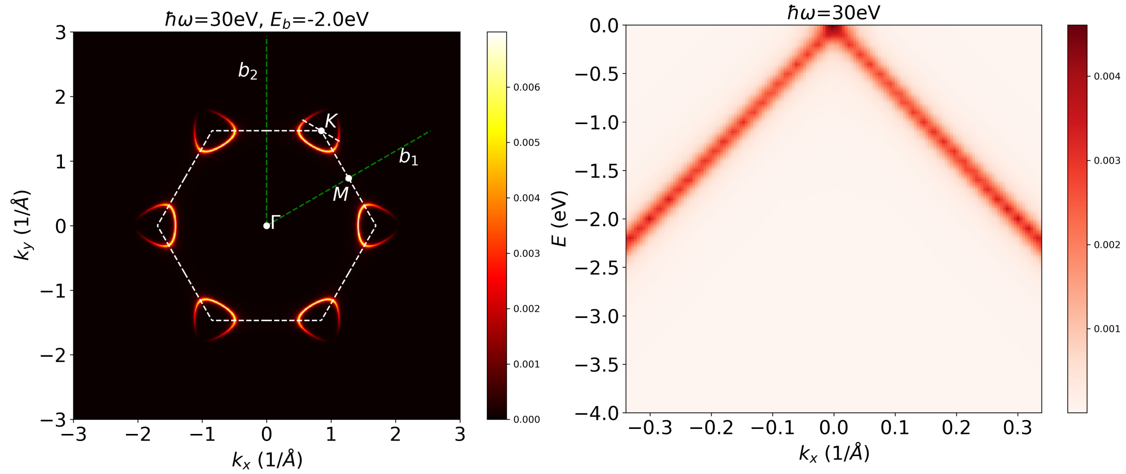

Figure 4.19: Left panel: Momentum map of graphene for E=-2.0 eV with dashed yellow line indicating the k-path of the bandmap in the right panel. Right panel: Bandmap for a cut through the Dirac cone below the Fermi level. The polarization is $\mathbf{A}_2 = [1, -i, 0]$ marking right-handed polarized light.

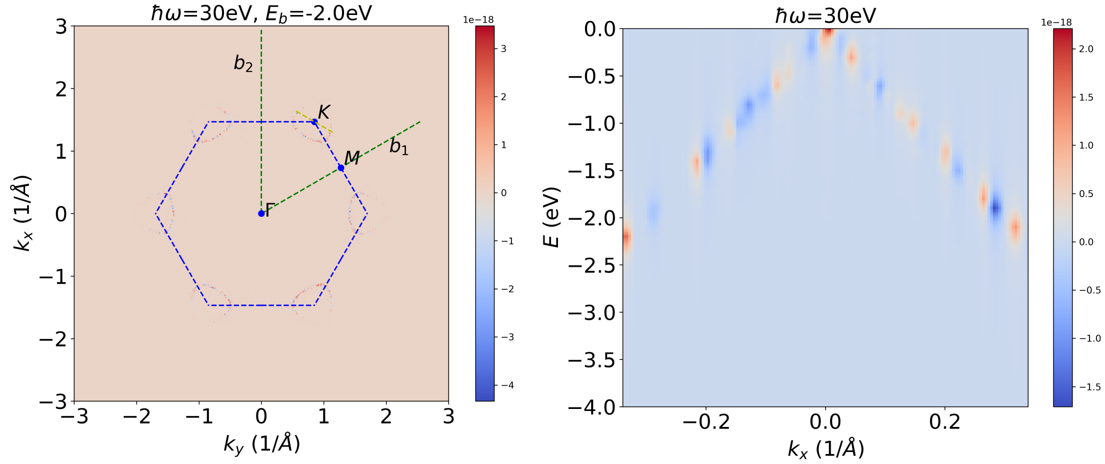

Figure 4.20: Left panel: Dichroism momentum map of graphene for E=-2.0 eV with dashed yellow line indicating the k-path of the bandstructure in the right panel. Right panel: Dichroism band map of a cut through the Dirac cone below the Fermi level. The polarization of the two simulations is at $\mathbf{A}_1 = [1, i, 0]$ and $\mathbf{A}_2 = [1, -i, 0]$.

One thing to notice here is the low intensity of 10^{-18}. Thus, the observed dichroism must rather be interpreted as only numerical noise. In Section 2.5 it was already shown that circular dichroism can not be observed in velocity gauge. Since chinook uses the length gauge in order to evaluate the matrix element, one would conclude from the above simulation that the CDAD effect vanishes for graphene. Schönhense in his paper [1] states that introducing a phase factor to the different angular momentum parts of the final state free wave reintroduces this circular dichroism effect. This will be discussed in the later chapter 5.3

In summary, the above presented results for linear polarizations look reasonable, while the results for circular dichroism are not satisfying. For a detailed qualitative analysis one however needs a reference to more accurate simulation, which is here done with the *octopus* code and presented in the next chapter.

4.4 TDDFT Calculation with Octopus

Octopus [12] is a very powerful TDDFT code, allowing a wide palette of applications. With the implemented t-surf method (see Section 2.7.1), it is possible to simulate ARPES experiments by applying a real-space, real-time approach instead of using Fermi's golden rule expression (see Section 2.1). The so-obtained photoemission angular distribution maps are potentially high accuracy since no assumption on the final state needs to be made and thus provides an ideal reference for the TB-model. Of course this method comes with a price, which is large computational effort. Even simple structures such as graphene require a considerable amount of time and resources.

Therefore only the photoemission intensity distribution of a k-path instead of the entire BZ is simulated. This section shows required input file used to run the simulation as well as the results. As an input *Octopus* receives a text file named **inp**. An example of this file is given below:

```
CalculationMode = TD ## first GS then TD
ExperimentalFeatures = yes
FromScratch = yes

## Paralellisation only enabled at TD-calculations, best is N=(
    states*(BZ K-points + Path KParKpoints= 12## auto
ParStates= 4##auto
#ParDomains=no

PeriodicDimensions = 2
Spacing=0.36
a = 4.651 # in bhor
BoxShape = parallelepiped

LL = 100 ## Relativly big nsized box in z-direction, at ca. 1/4/ bis
     1/2 the simualted "Detector" should be
%LatticeParameters
a | a | LL
%
%LatticeVectors
1    | 0         | 0.
-1/2 | sqrt(3)/2 | 0.
0.   | 0.        | 1.
%
%ReducedCoordinates
'C' |  0.  |    0. |   0.
'C' |  1/3 |   2/3 |   0.
%
%KpointsGrid
 12 | 12 | 1
%
%KpointsPath ## Pfad entlang dem die Bandstruktur ausgewertet wird
119          ## points of the k-path -> 120 K-points -> multiple of
    12 because of parallelisation
```

```
0.21786328 | 0.44880339 | 0 ## K'-point
0.44880339 | 0.21786328 | 0 ## K-point
%

wpr = 30 * eV ## Photon energy
tcpr=2*pi/wpr
II = 1.0E9    ## Intensity in W/cm^2
EE = sqrt(II/3.51e+16) ## Electric field
AApr = EE * 137/wpr   # Amplitude
TT = 50 * fs  ## Propagationtime
npr = TT/tcpr
Tpr = tcpr*npr

%TDExternalFields
  vector_potential | 0 | 1  | i | wpr |"probe" ## Vektorfield in x-direction
%
%TDFunctions
  "probe"  | tdf_from_expr | 'AApr*sin(wpr*t/(2*npr))^2*step(Tpr-t)*step(t)' ## Sin^2 envelope
%
TDTimeStep = 0.08 ##hbar\hartree
TDPropagationTime = Tpr

Lmin = LL / 4 ## start CAP at detector
AbsorbingBoundaries = cap
ABCapHeight = -1.0
%ABShape
 Lmin | LL | "abs(z)" ## absorbing boundary after detector
%

PhotoElectronSpectrum = pes_flux ## enable this method
PES_Flux_Lsize = Lmin ## distance to detector = start of CAP

Emin =  wpr - 25. * eV
Emax =  wpr
DE   = 0.01 * eV
%PES_Flux_EnergyGrid
Emin | Emax | DE ## energy window and resolution for ARPES band struktur
%

## set default of 50 to 500
OutputInterval = 500
RestartWriteInterval = 500
```

While many of the parameters are self-explanatory, a few points must be noted. The TDDFT calculation starts from an already converged ground state calculation. So before running the above script, one needs to do a DFT calculation by altering the parameter **CalculationMode** to **GS**. The lattice parameters where chosen described in Chapter 2.3. The photon energy was set to 30 eV with an intensity of 1 MW/cm^2. The probe pulse should be switched on adiabatically, thus an envelope sine function was used to slowly rise and decrease the amplitude of the carrier frequency.

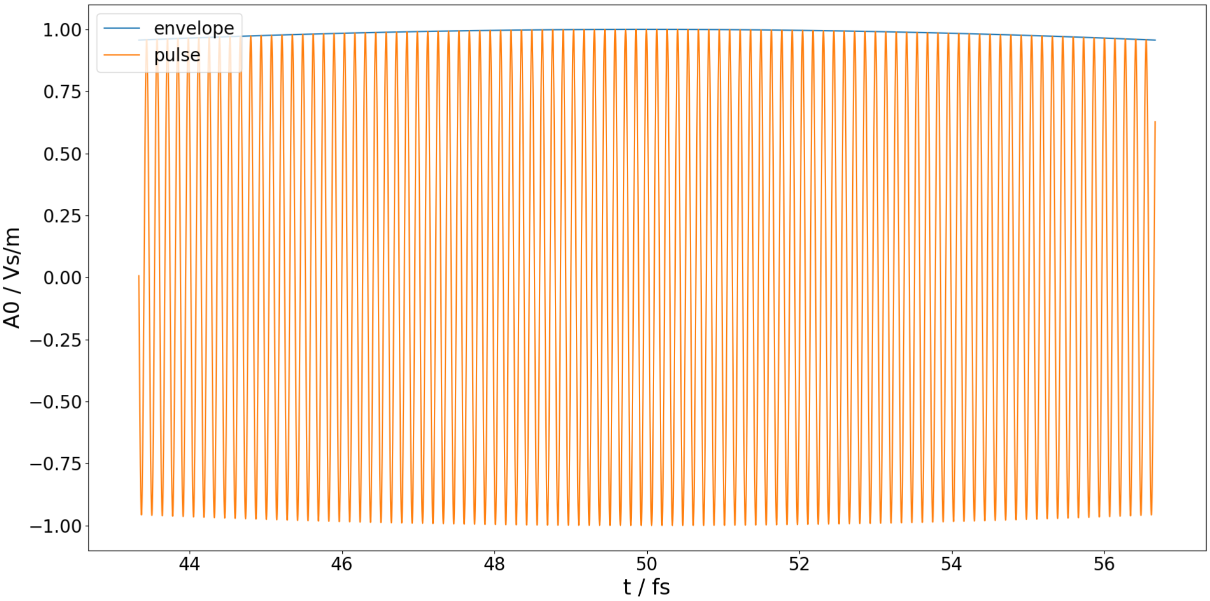

Figure 4.21: Example figure of an external vector field with envelope function (blue) $\sin^2(\omega_{env} t)$ and a laser pulse (orange) $\cos(\omega t)$ with frequencies of $\omega_{env} = 0.057 \frac{1}{fs}$ and $\omega = 46 \frac{1}{fs}$

The maximal amplitude of the probe pulse corresponds to a maximal intensity of 1 MW/cm^2 of the light. The total simulation time was set to 50 fs. The time step was chosen as 0.08 $\frac{\hbar}{H}$ which is $dt \approx 0.0024$ fs and gives a total of 25838 time steps. One should really think about choosing the parameters of the probe pulse correctly in order to get the desired energy and intensity for the simulation (A detailed discussion can be found in Section 2.7.2).

Let us take a look at an ARPES simulation of linear polarized light. Choosing a k-path trough the K points of the BZ, the path was chosen as a line connecting the two points

$$\mathbf{K}_1 = (0.2179, 0.4488, 0) \ , \mathbf{K}_2 = (0.4488, 0.2179, 0) \tag{4.13}$$

given in reduced coordinates, sampled along 120 points. The path was chosen to be perpendicular to the vector pointing from Γ to the K-point. It is indicated in Figure 4.9. It is also indicated in the Figures 4.17 to 4.20 of Section 4.3 as dashed yellow lines through the K-point.

The polarization can be adjusted in the input file above via the `TDExternalFields` parameter. As already discussed in Section 4.3.2, choosing the polarization vectors to be oriented ±45° to the K-point, should provide a well comparable linear dichroism map. The polarizations were chosen as $\mathbf{A}_1 = [\cos(15^\circ), \sin(15^\circ), 0]$ and $\mathbf{A}_2 = [\cos(105^\circ), \sin(105^\circ), 0]$.

With the T-SURF method described in Section 2.7.1, one can generate an output file consisting of a table of the k_x, k_y, k_{path}, E and the $P(E, k_{path})$ values. The values k_x, k_y define the corresponding point in the k-space. The k_{path} values account for the distance between K_1 and K_2 defined as the k-path. E accounts for the corresponding energy and $P(E, k_{path})$ is the electron photoemission probability. The electron photoemission probability is directly proportional to the intensity of the ARPES simulation. Often [23] the units and absolute values of $P(E, k_{path})$ are therefore not shown in plots. Because in the dichroism maps absolute differences are calculated, we will show these values.

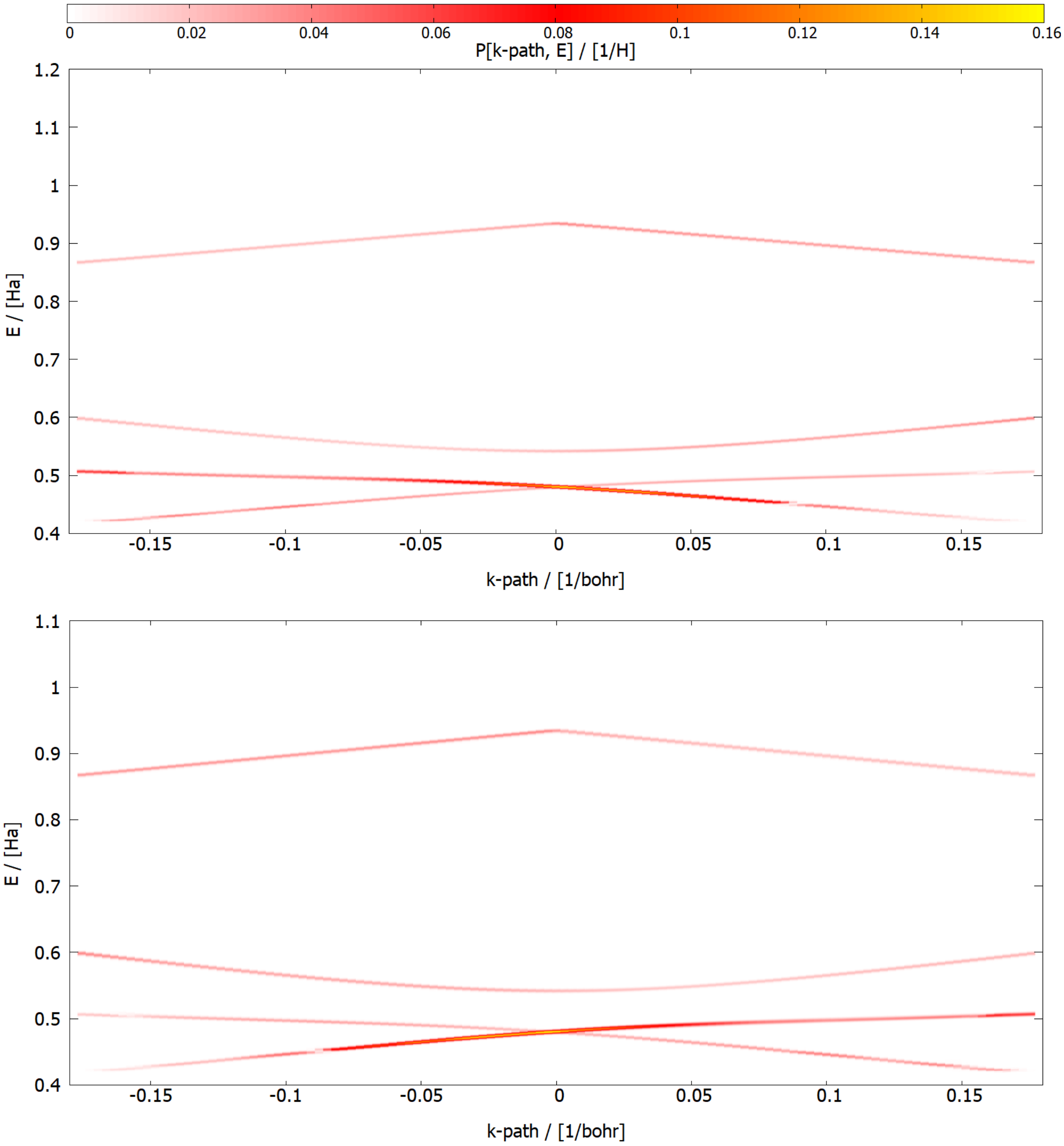

Figure 4.22: Octopus simulations of ARPES intensities of graphene with a linear polarized vector field of $\mathbf{A}_1 = [\cos(15°), \sin(15°), 0]$ (upper image) and $\mathbf{A}_2 = [\cos(105°), \sin(105°), 0]$ (lower image) for a time interval of 50 fs, an intensity of $I = 1$ MW/cm^2 and $\omega = 30$ eV along $K_1 - K - K_2$ where $K = 0 \rightarrow k_{path} = 0$. $P(\mathbf{k}, E)$ refers to the electron photoemission probability.

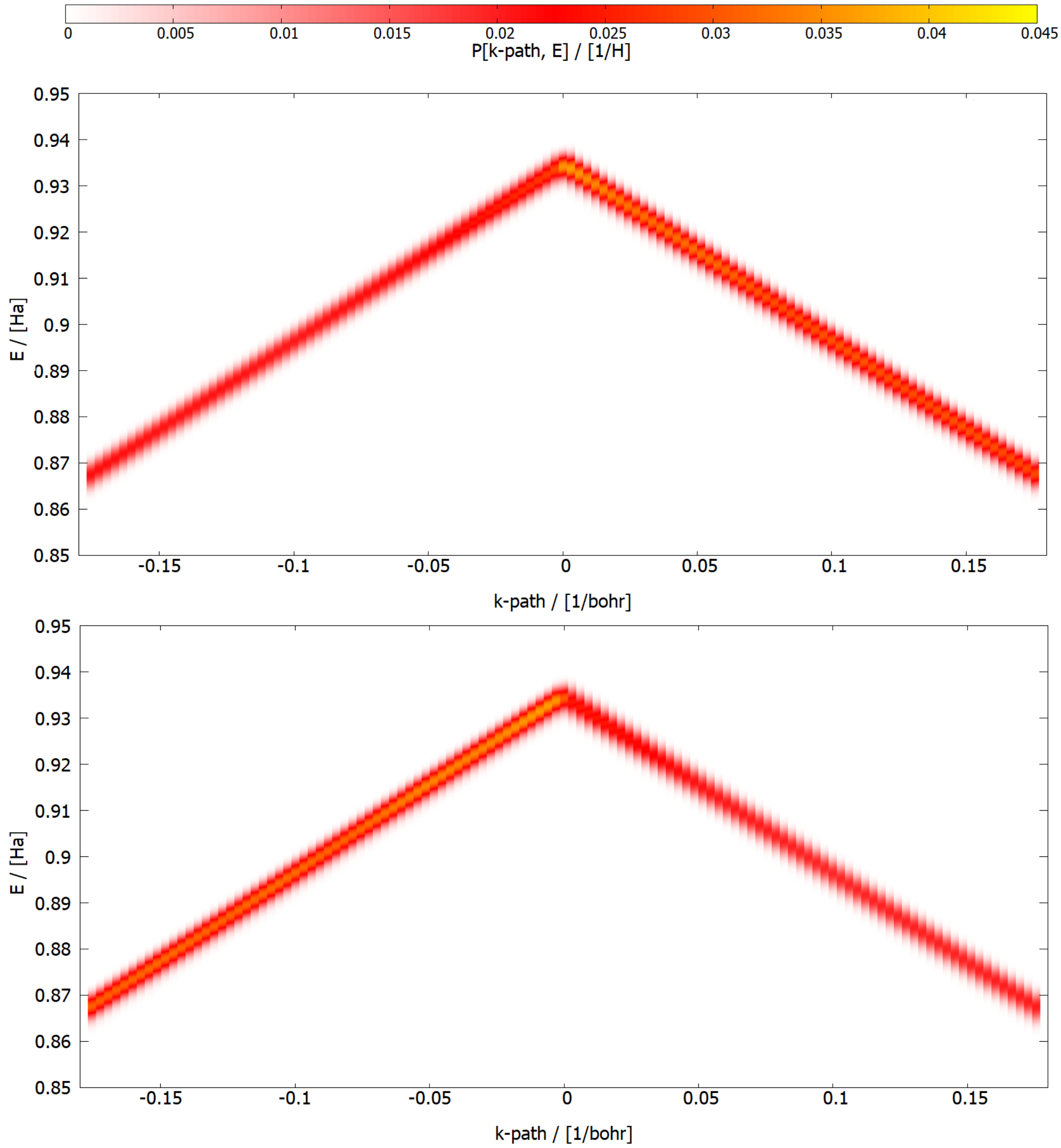

Figure 4.23: Octopus simulations of ARPES intensities of graphene with a linear polarized vector field of $\mathbf{A}_1 = [\cos(15°), \sin(15°), 0]$ (upper image) and $\mathbf{A}_2 = [\cos(105°), \sin(10°5), 0]$ (lower image) with focus on the $2p_z$ band for a time interval of 50 fs, an intensity of $I = 1$ MW/cm^2 and $\omega = 30$ eV along $K_1 - K - K_2$ where $K = 0 \rightarrow k_{path} = 0$. $P(\mathbf{k}, E)$ refers to the electron photoemission probability.

The graphene ARPES intensities sown in Figure 4.22 and 4.23 are in the range of $[0, 0.16]$ and the one of the $2p_z$ band in the range of $[0, 0.04]$. One can see the expected behavior of the intensity change along the k-path where the maximum intensity is on the side next to the K-point where the polarization points at. This is in agreement with the velocity gauge proportionality $|\mathbf{A} \cdot \mathbf{k}|^2$ of the one-step model discussed in Section 2.5. However the intensity here is peaked close to the K-point in opposite to the calculations done in chinook where the intensity rises steadily in the direction of the polarization.

Now we want to take a look at ARPES simulations with circularly polarized light. As already discussed in Section 4.3 this can be achieved with complex vectorfields of the form $\mathbf{A}_L = [1, i, 0]$ and $\mathbf{A}_R = [1, -i, 0]$. The same simulation properties as for the linear polarized ARPES intensity simulations above were used.

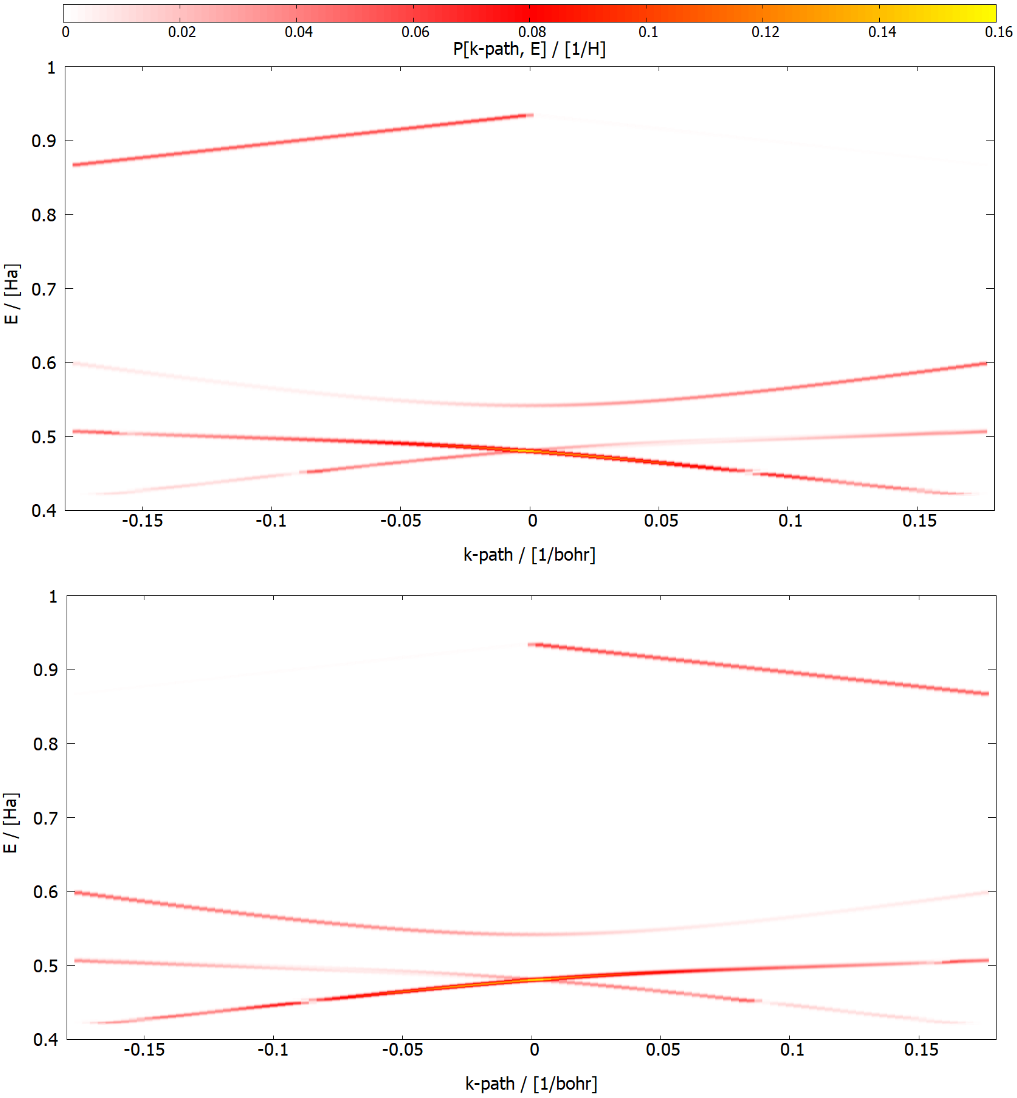

Figure 4.24: Octopus simulations of ARPES intensities of graphene with a linear polarized vector field of $\mathbf{A}_L = [1, i, 0]$ (upper image) and $\mathbf{A}_R = [1, -i, 0]$ (lower image) for a time interval of 50 fs, an intensity of $I = 1$ MW/cm^2 and $\omega = 30$ eV along $K_1 - K - K_2$ where $K = 0 \rightarrow k_{path} = 0$. $P(\mathbf{k}, E)$ refers to the electron photoemission probability.

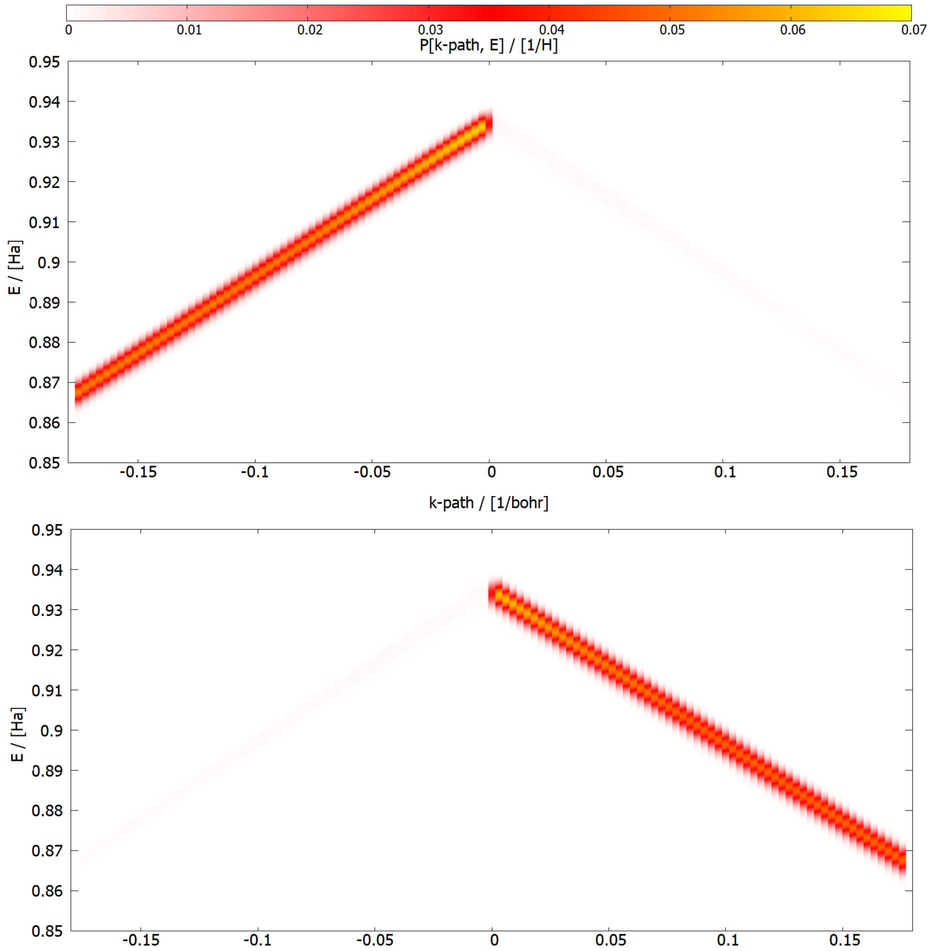

Figure 4.25: Octopus simulations of ARPES intensities of graphene with a linear polarized vector field of $\mathbf{A}_L = [1, i, 0]$ (upper image) and $\mathbf{A}_R = [1, -i, 0]$ (lower image) with focus on the $2p_z$ band for a time interval of 50 fs, an intensity of $I = 1\,\mathrm{MW}/cm^2$ and $\omega = 30$ eV along $K_1{-}K{-}K_2$ where $K = 0 \rightarrow k_{path} = 0$. $P(\mathbf{k}, E)$ refers to the electron photoemission probability.

The intensity of the ARPES simulated band structures for Figure 4.24 and 4.25 is in the range of $[0, 0.16]$ and the one of the $2p_z$ is in the range $[0, 0.07]$. One can see that in the $2p_z$ band the electron photoemission probability is strongly peaked on one side of the K-point. This is in disagreement with the one-step model discussed in Section 2.5 which predicts no difference between left- and right handed polarized light in the velocity gauge. The results of the chinook simulation for circularly polarized light conclude that there is also no dichroism in the length-gauge.

By a closer investigation of the ansatz of the chinook program [16] (Equation (9)) one notices that the final state of the matrix element is not a plane wave, but a set of plane waves emerging from each isolated atomic orbital.

$$M(\mathbf{k}) \propto \left\langle e^{i\mathbf{kr}} \left| \mathbf{A}\cdot\mathbf{r} \right| \Phi_i^\alpha(\mathbf{r}) \right\rangle \sum_\alpha n_\alpha \left\langle e^{i\mathbf{kr}} \left| \mathbf{A}\cdot\mathbf{r} \right| \phi_\alpha(\mathbf{r}) \right\rangle \tag{4.14}$$

This means for the $2p_z$ band of single layer graphene that the matrix element is a sum matrix elements of the $2p_z$ orbitals only. We have showed in Section 3 that the dichroism of a single $2p_z$ orbital vanishes. Thus it is no surprise that in chinook this effect can not be seen in this setup. We will discuss this in more detail in the next section.

5 Comparison and Analysis

5.1 Conclusions of the Chinook Simulations

In Section 4.3.2 it was shown that for single layer graphene, simulated with the chinook program, the CD effect cannot be seen. In equation (9) of Ref.[16] it is explained that chinook evaluates the photoemission matrix element

$$M(\mathbf{k}) \propto \left\langle e^{i\mathbf{kr}} \left| \mathbf{A}\cdot\mathbf{r} \right| \Phi_j(\mathbf{r}) \right\rangle \tag{5.1}$$

in length gauge. Chinook also uses an LCAO basis which was for the simulation in Section 4.3.2 limited to $2p_z$ atomic orbitals, where only nearest neighbor interactions were included in the TB model. One can therefore say that the photoemission matrix element was calculated within the Hückel approximation. In Section 3.2 we have derived a general expression (Equation 3.48) for planar hydrocarbons within the Hückel model.

To this end let us take a look, at the defining equations given in Ref.[16]. For consistency, we have adjusted the notation of Ref.[16] to match the notations used throughout this work. Using an LCAO ansatz of the form $\Phi_j = \sum_{n,\alpha} c^j_{n,\alpha}\phi_{n,\alpha}$, The photoemission matrix element as described in Ref.[16] is written as

$$M(\mathbf{k}) \propto \left\langle e^{i\mathbf{kr}} \left| \mathbf{A}\cdot\mathbf{r} \right| \Phi_j^\alpha(\mathbf{r}) \right\rangle = \sum_{n,\alpha} c^j_{n,\alpha} \int d^3r e^{i\mathbf{kr}}(\mathbf{A}\cdot\mathbf{r})\phi_{n,\alpha}(\mathbf{r}) e^{-\zeta_{\alpha,n}} = \tag{5.2}$$

and expanded with Equation 6.12, $(\mathbf{A}\cdot\mathbf{r}) = \sum_\mu A_\mu Y_{1,\mu}$ and
$\phi_{n,\alpha}(\mathbf{r}) = R_{n,\alpha}(r) Y_{l_\alpha,m_\alpha}(\Omega)$ into

$$\begin{aligned} M(\mathbf{k}) = \sum_{n,\alpha} c^j_{n,\alpha} e^{-\zeta_{\alpha,n}} \sum_{l=0}^{\infty} \sum_{m=-l}^{l} Y_{l,m}(\Omega_k)(i)^l \cdot \\ \cdot \left(\int dr j_l(kr) r^3 R_{\alpha,n}(r) \right) \sum_\mu A_\mu \left(\int d\Omega Y_{l,m} Y_{1,\mu} Y_{l_\alpha,m_\alpha} \right). \end{aligned} \tag{5.3}$$

Note that the additional term $e^{-\zeta_{\alpha,n}}$ defines an empirical extinction factor which is supposed to take into account the mean free path of a photoemitted electron. (note: The sum over m is not explicitly mentioned in Ref.[16] for some reason). One should also notice $\mathbf{A} \neq (A_{-1}, A_0, A_1)$. For some reason also complex conjugation of certain terms was not mentioned explicitly.

Apart from these small inconsistencies in the notation, there is one more important point to be noted in the transition from Equation 5.2 to 5.3. Each of the atomic orbitals $\phi_{n,\alpha}$, indicated by the index n, has a different coordinate frame (transformed by a shift $\mathbf{r} = \mathbf{r}_n - \mathbf{R}_n$). The plane wave final state, however, is referred to only one common $\mathbf{r}$. In the above derivation, however, each atomic orbital is paired with a plane wave at its origin. This means that the final state of the matrix element is actually not a single plane wave, but set of plane waves emerging from each isolated atomic orbital.

For an LCAO initial state, the photoemssion matrix element is of the form

$$M(\mathbf{k}) \propto \sum_{\alpha} n_{\alpha} \left\langle e^{i\mathbf{kr}} \left| \mathbf{A} \cdot \mathbf{r} \right| \phi_{\alpha}(\mathbf{r}) \right\rangle, \tag{5.4}$$

where n_{α} is some real constant.

For an initial state consisting of a linear combination of identical $2p_z$ orbitals this means that

$$M(\mathbf{k}) \propto \sum_{\alpha} n_{\alpha} \left\langle e^{i\mathbf{kr}} \left| \mathbf{A} \cdot \mathbf{r} \right| \phi_{2p_z}(\mathbf{r}) \right\rangle = \left\langle e^{i\mathbf{kr}} \left| \mathbf{A} \cdot \mathbf{r} \right| \phi_{2p_z}(\mathbf{r}) \right\rangle \sum_{\alpha} n_{\alpha}. \tag{5.5}$$

In Section 3.1.4 it has been shown that for left handed $\mathbf{A}_L$ and right handed $\mathbf{A}_R$ polarized light

$$\left|\langle \psi_f \left| \mathbf{A}_R \cdot \mathbf{r} \right| \psi_i \rangle\right|^2 - \left|\langle \psi_f \left| \mathbf{A}_L \cdot \mathbf{r} \right| \psi_i \rangle\right|^2 = 0, \tag{5.6}$$

which is exactly what has been shown by the chinook simulations of Section 4.3.2 for the vanishing CDAD map of single layer graphene.

Inspection of Equation 5.4 also reveals that the chinook program can show a non-vanishing CDAD if the atomic orbitals ϕ_{α} are not identical. In order to validate this hypothesis, we investigate hexagonal boron nitride (hbn) which also forms a honeycomb lattice similar to graphene, but in the case of hbn, the basis consists of two inequivalent atoms, namely boron and a nitrogen, respectively. Applying the Hückel model to hbn, the atomic orbitals, even if only $2p_z$ orbitals are included, are different due to a different nuclear charge. Thus one cannot proceed as in Equation 5.5 and pull the matrix element out of the sum. Figure 5.1 shows the CDAD map of $\mathbf{A}_L = [0, 1, i]$ and $\mathbf{A}_L = [0, 1, -i]$ polarized light as obtained from chinook, which is in fact clearly not vanishing.

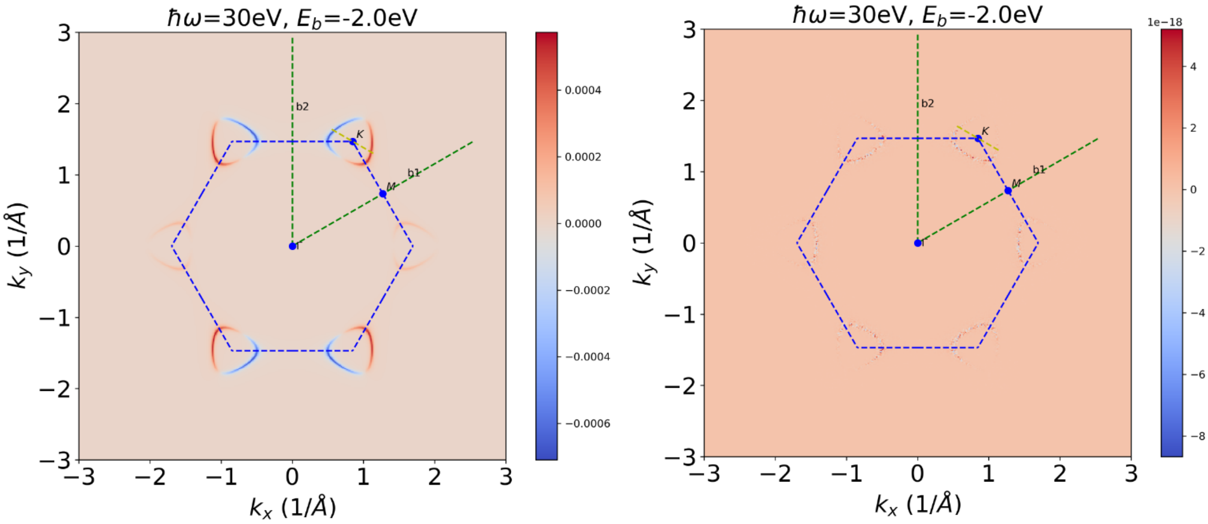

Figure 5.1: Constant binding energy CDAD map of hbn (left panel) and graphene (right panel) simulated in chinook. The polarizations where taken as $\mathbf{A}_{L/R} = [0, 1, \pm i]$.

For comparison, the result of a chinook simulation for graphene with the same polarizations is displayed in Figure 5.1. On the other hand, when choosing a polarization as $\mathbf{A}_{L/R} = [1, \pm i, 0]$, also for hbn the CDAD vanishes.

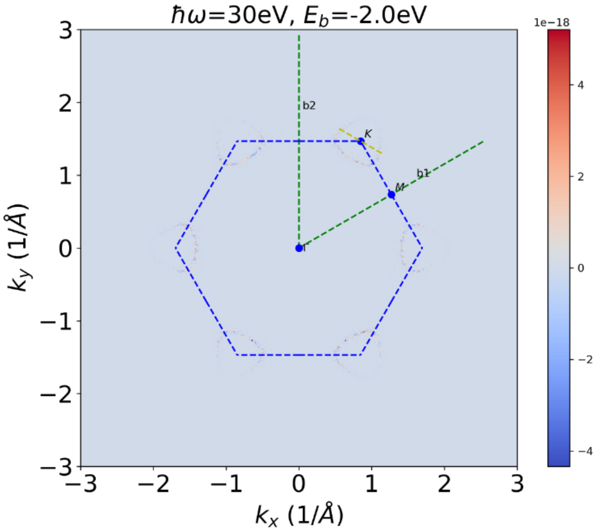

Figure 5.2: Constant binding energy CDAD map of hbn as simulated in chinook. The polarizations where taken as $\mathbf{A}_{L/R} = [1, \pm i, 0]$.

One can again explain why the CDAD map vanishes for this polarizations by looking at the corresponding matrix elements. At this point it should be clear that chinook does not provide a suitable framework to further investigate the CDAD effects in the tight binding approximation. Since the simulations in chinook of linear polarized photoemission intensities of graphene looked, as discussed in 4.3.2, reasonable, we will compare them to the TDDFT simulations of the octopus code.

5.2 Comparison of the Linear Dichroism

The linear dichroism maps of graphene simulated in chinook, presented in Section 4.3.2, show the expected $|\mathbf{A} \cdot \mathbf{k}|^2$ dependence, discussed in Section 2.5. To compare this to the octopus results, the corresponding dichroism map of the ARPES simulation presented in Section 4.4 is shown in Figure 5.4.

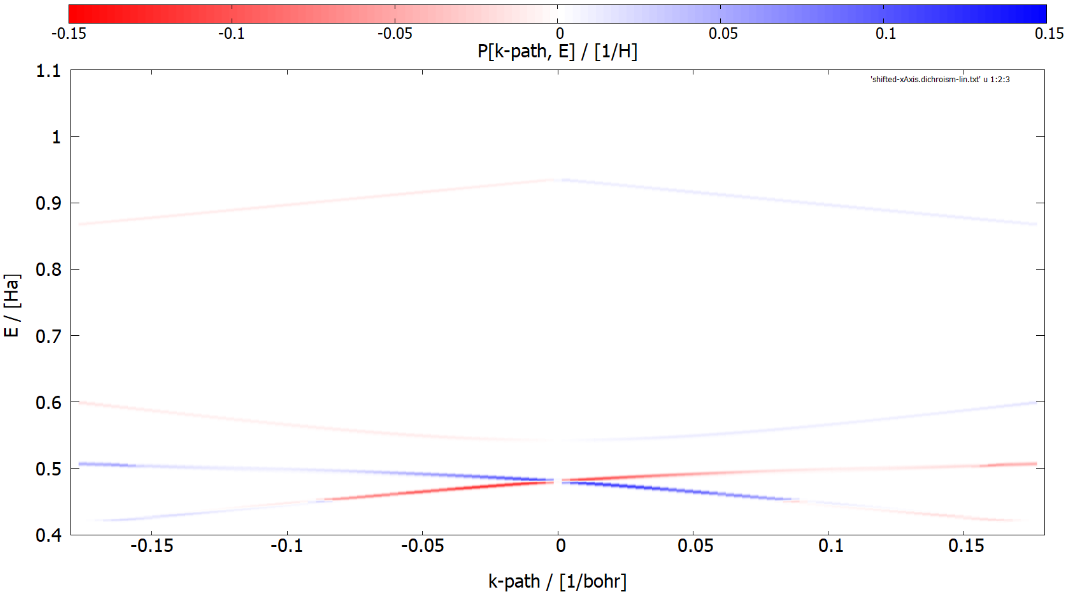

Figure 5.3: Linear dichroism map from the TDDFT simulation for graphene (compare Figure4.22). The linear polarizations were taken along $\mathbf{A}_1 = [\cos(15°), \sin(15°), 0]$ and $\mathbf{A}_2 = [\cos(105°), \sin(105°), 0]$ together with a time interval of 50 fs, an intensity of $I = 1$ MW/cm^2 and $\omega = 30$ eV along $K_1 - K - K_2$ where $K = 0 \rightarrow k_{path} = 0$. $P(\mathbf{k}, E)$ refers to the electron photoemission probability.

A direct comparison of the linear dichroism APRES intensity distribution simulated in chinook (shown in Figure 4.17) can be seen in Figure 5.4.

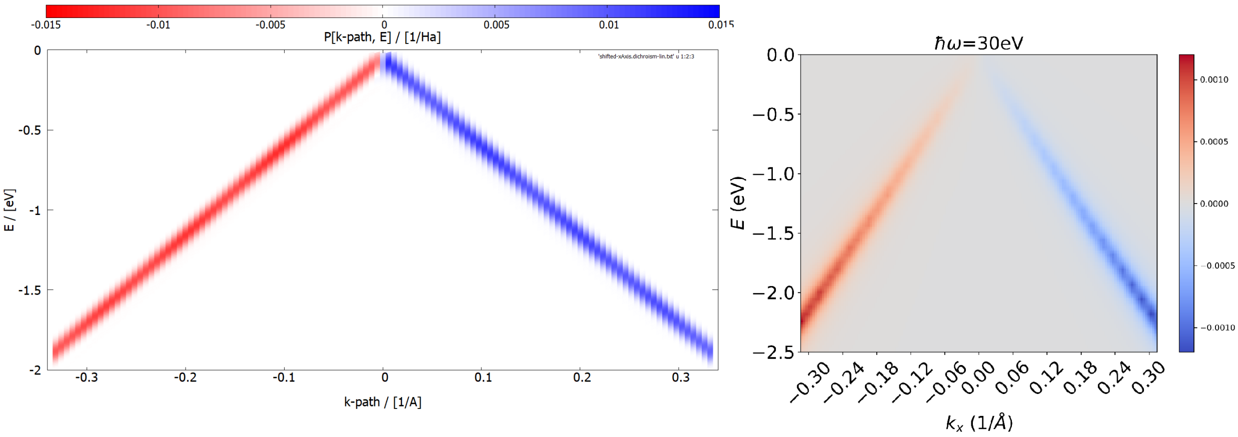

Figure 5.4: Left panel: Linear dichroism map of the TDDFT simulated graphene ARPES intensity distributions shown in Figure 5.3. Right panel: Linear dichroism map of the TB simulated graphene ARPES intensity distributions shown in Figure 4.17.

Note that the energy of the intensity distribution in the chinook simulation has a steeper slope. This could be explained by the fact that octopus utilized the LDA functional while the Hückel model of Section 4.1 was fitted to DFT energies calculated with the B3LYP functional. One can see that even though the chinook example resembles the effect, the LDAD effect gets weaker close to the Dirac point ($k_{path} = 0$). The intensity distribution of the chinook simulation is proportional to the factor $|\mathbf{A} \cdot \mathbf{k}|^2$ which describes the velocity gauge discussed in Section 2.5. For increasing $k_{path} > 0$ the scalar product $\mathbf{A}_1 \cdot \mathbf{k}$ rises while $\mathbf{A}_2 \cdot \mathbf{k}$ falls. It is possible that the octopus simulation also shows this proportionality, but the photo-electron emission probability generally rises when approaching the K-point thus the two effects cancel each other.

Even though it is not possible to make reasonable comparisons of the ARPES intensity maps of circularly polarized light with the chinook simulations, the circular dichroism intensity distribution of the TDDFT simulations done in octopus are shown in Figure 5.5 for completeness.

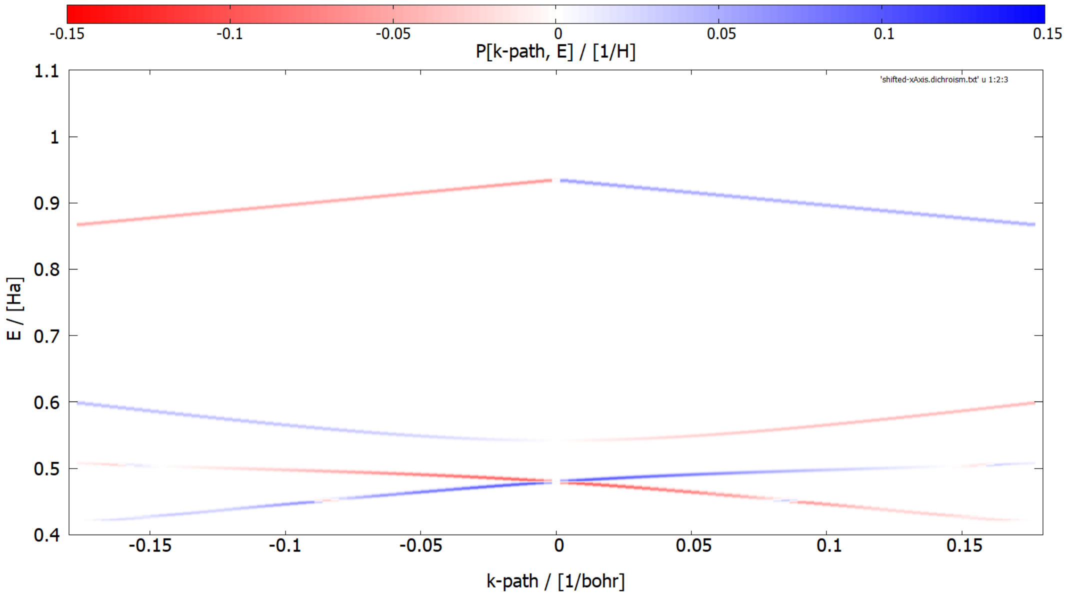

Figure 5.5: Circular dichroism map of the TDDFT simulated graphene ARPES intensity distributions shown in Figure 4.24. The circular polarizations were taken along $\mathbf{A}_L = [1, i, 0]$ and $\mathbf{A}_R = [1, -i, 0]$ together with a time interval of 50 fs, an intensity of $I = 1$ MW$/cm^2$ and $\omega = 30$ eV along $K_1 - K - K_2$ where $K = 0 \to k_{path} = 0$. $P(\mathbf{k}, E)$ refers to the electron photoemission probability.

5.3 Application of the LCAO Method

Since chinook has demonstrated problems in correctly accounting for CDAD effect in the tight binding approximation, the question whether the CDAD effect exists within the plane wave final state approximation in conjunction with the length gauge for the transition matrix element could not have been answered. We now want to make use of some of the results collected along the sections of this work to write a *python* script which calculates the photoemission intensity distribution of arbitrary 2p^2-hybridized hydrocarbons. By setting up a Hückel model for the molecule, and using the hopping parameter function from Section 4.1, one gets a set of coefficients c_n^j for a corresponding molecular orbital Φ^j. Using the LCAO ansatz from Section 3.2 one can evaluate the photo emission matrix element with Equation 3.48

$$\left\langle e^{i\mathbf{kr}} \left| \mathbf{A} \cdot \mathbf{r} \right| \Phi_j \right\rangle = \sum_n c_n^j e^{i\mathbf{k}\mathbf{R}_n} \left(\Lambda(\mathbf{k},\mathbf{A}) + (\mathbf{R}_n \cdot \mathbf{A}) \mathcal{F}(\phi_{n,\alpha})(\mathbf{k}) \right). \tag{5.7}$$

By evaluating the Λ function and subsequently computing the photoemission matrix element on a sphere with constant k value, one gets constant binding energy momentum maps. The CD map is then setup and normalized by

$$I_{CD} = \frac{I_L - I_R}{\max(I_R)} \tag{5.8}$$

As an example output, the constant binding energy momentum maps of the HOMO orbital of the tetracene molecule are shown in Figure 5.8. The polarizations were chosen as $A_L = [i, \cos(65°), \sin(65°)]$ and $A_L = [\cos(65°), i, \sin(65°)]$ to achieve an azimuthal angle of the incident light beam of 65°. This can be compared to a photoemission tomography experiment for the tetracene molecule adsorbed on a Ag(100) surface from [4]. In [4] the Figures (S6) and (S7) show experimental k-maps of the HOMO orbital of tetracene. The Hückel model gives an orbital energy of $E_{HOMO} = -2.06$ eV for the HOMO orbital of tetreacene.

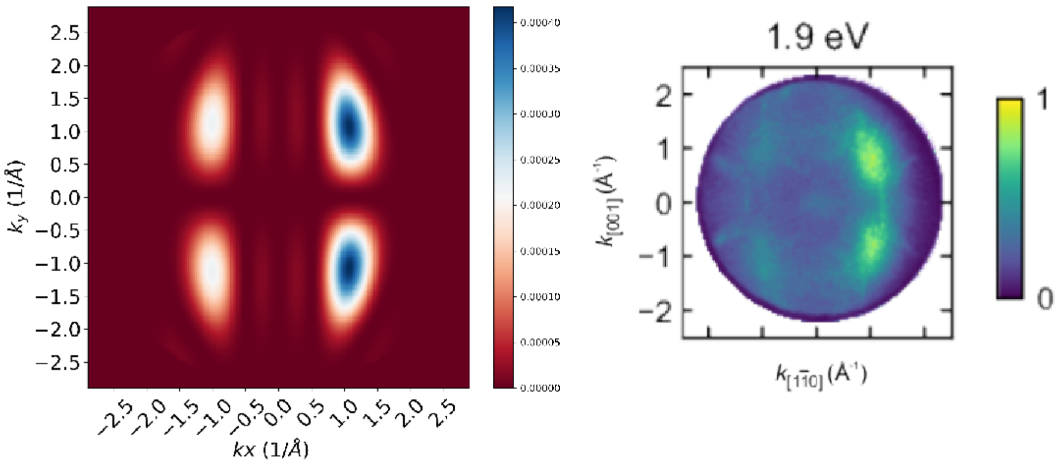

Figure 5.6: Right panel: Experimental k-maps of the HOMO orbital for the tetracene molecule from Figure (S6) of [4]. Left panel: Constant binding energy momentum of the HOMO orbital of the tetracene molecule simulated in the Hückel approximation with a photo-electron energy of 35 eV and polarization of $\mathbf{A}_1 = [i, \cos(65°), \sin(65°)]$.

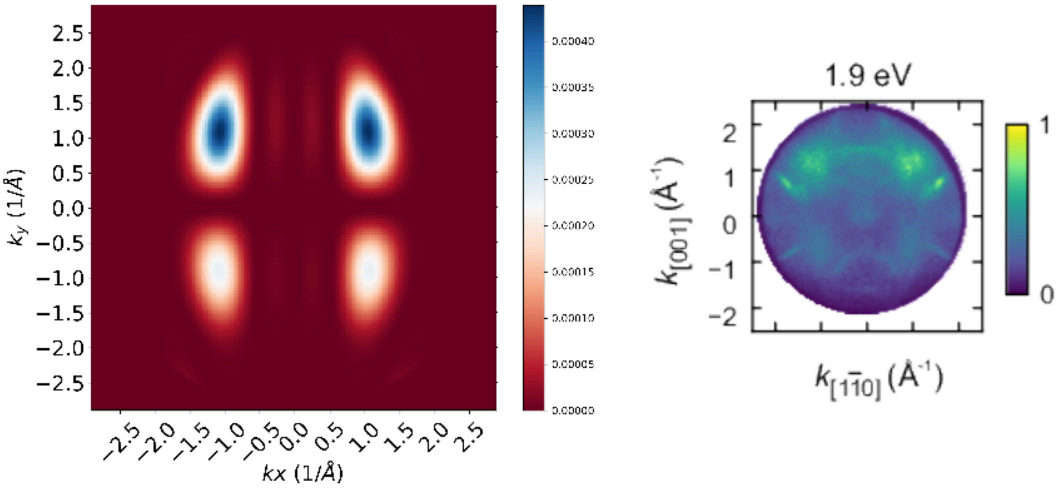

Figure 5.7: Right panel: Experimental k-maps of the HOMO orbital for the tetracene molecule from Figure (S7) of [4]. Left panel: Constant binding energy momentum of the HOMO orbital from the tetracene molecule simulated in the Hückel approximation with a photo-electron energy of 35 eV and a polarization of $\mathbf{A}_1 = [\cos(65°), i, \sin(65°)]$.

These momentum maps look reasonable compared to experimentally obtained momentum maps from Ref. [4]. The fact that the CDAD is clearly visible (shown in Figure 5.8), is a clear evidence that the length-gauge and the velocity gauge evaluated photoemission matrix elements are not equivalent.

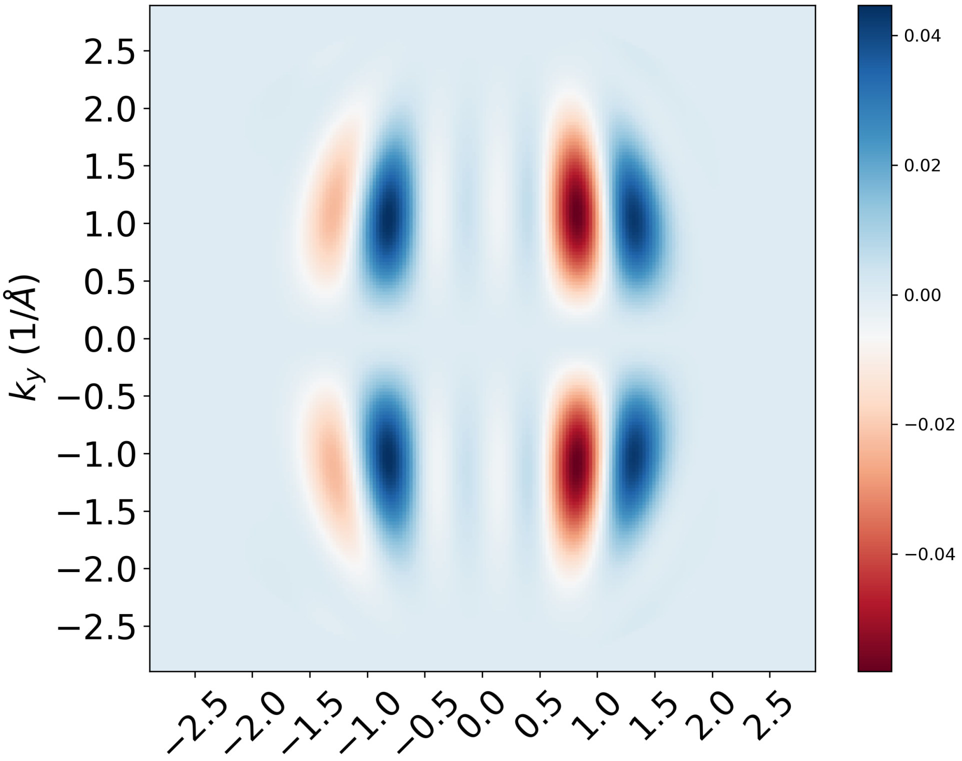

Figure 5.8: CDAD map of the HOMO orbital from the tetracene molecule simulated in the Hückel approximation with a photo-electron energy of 35 eV and polarizations of $\mathbf{A}_{L/R} = [\pm i, \cos(65°), \sin(65°)]$.

The CDAD is different for different polarizations. It would be interesting to see how well this method works in general. A detailed analysis of the quality of constant binding energy momentum maps simulated within this model is, however, beyond the scope of this work. In the next section we will try to apply this method to graphene to get an insight on the CDAD effect of the photoemission intensity distribution evaluated in length gauge within the Hückel approximation for periodic materials.

5.4 The LCAO Method for a Graphene like System

Here we will test the program discussed in Section 5.3 on a finite graphene like system consisting of a grphene disk (see Figure 5.9). To this end, we approximate the infinitely extended graphene lattice by a finite disc-shaped cluster which is cut out from grpahene. When the diameter of this finite cluster is large enough, the result should approximate those of the infinite layer. A question at hand is if CDAD within the length gauge expression of the photoemission matrix element for single layer graphene exists. If so, does it compare to the CDAD effect shown by the octopus code in Section 4.4. Does the introduction of an angular momentum-dependent phase factor to the final state plane wave changes the photoemission intensities such that they resemble the results from the TDDFT calculation of octopus in of Section 4.4? To answer these questions, let us jump right into the setup of the simulation.

Within the approach given by Equation 5.7, only finite systems without periodic boundary conditions can be treated. Therefore a circular molecule consisting of 3658 carbon atoms repeated the same way as in graphene was set up. The shape of a circle was chosen to minimize open bonds at its circumference. The corresponding geometry can be seen in Figure 5.9.

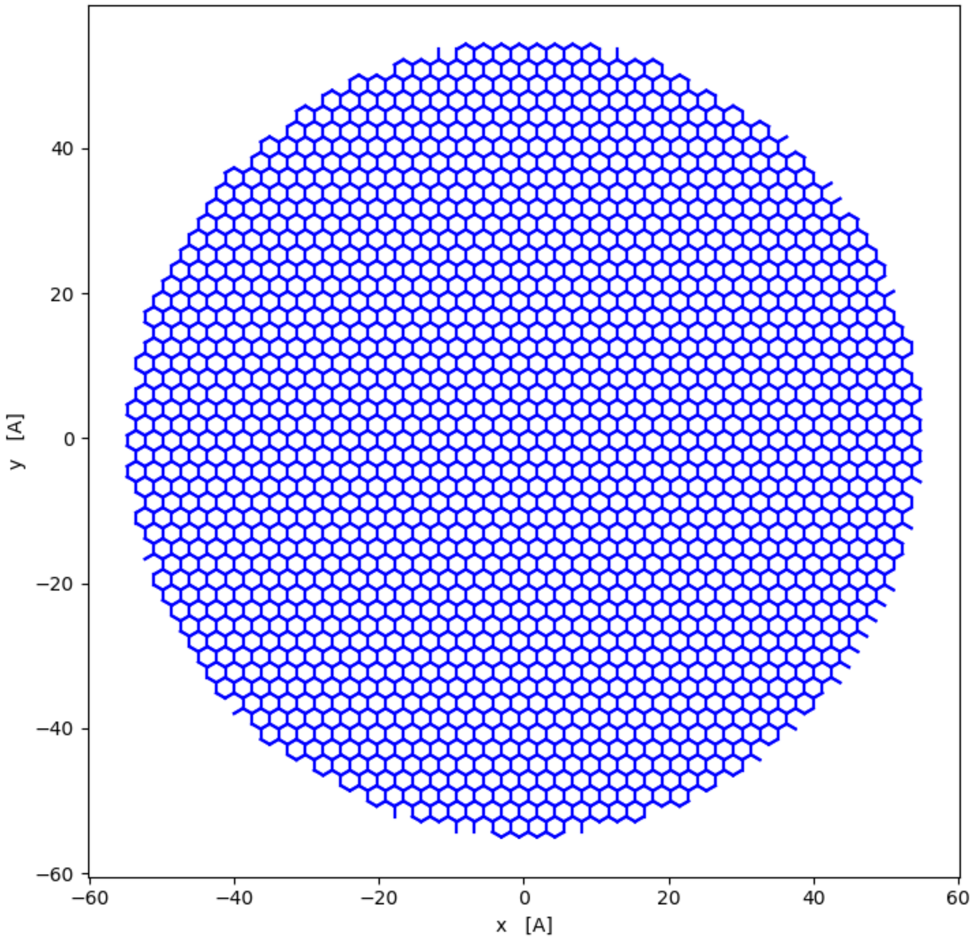

Figure 5.9: Geometry of the finite graphene-like cluster with 3658 carbon atoms in real space. Each blue line represents a carbon-carbon bond.

Calculating the eigenstates of this system can be done efficiently with the Hückel method from Section 4.1. For comparison the density of states can be visualized by adding up a sharp Gauß peak at each energy eigenvalue over the entire energy eigenvalue spectrum of the system. The eigenvalues of the Hückel matrix gives the energies ϵ_n. The DOS can be approximated as:

$$D(E) \approx \sum_n \frac{1}{\sqrt{2\pi\sigma^2}} e^{-\frac{(E-E_n)^2}{2\sigma^2}} \tag{5.9}$$

where σ was chosen as 0.1. The energy spectrum of this model is in $E \in [-12.97, 6.12]$ eV. In the Hückel matrix the the hopping parameter is chosen as $t(1.42) = -3.15$ eV and the onsite energy was set to $\epsilon = -3.42$ eV which also gives the Fermi edge. The DOS of this Hückel model is shown in Figure 5.10. Together with the dispersion relation of Section 2.4.5 given by Equation 2.70, the DOS, defined by

$$D(E) = \frac{1}{V}\sum_{i}^{N}\delta(E - E_i(\mathbf{k})), \tag{5.10}$$

can be evaluated for an infinite system. Choosing the same hopping parameter and on-site energy as in the Hückel model, and evaluating the dispersion relation of Equation 2.70 on a finite k-grid inside the first BZ, the resulting DOS is also included in Figure 5.10.

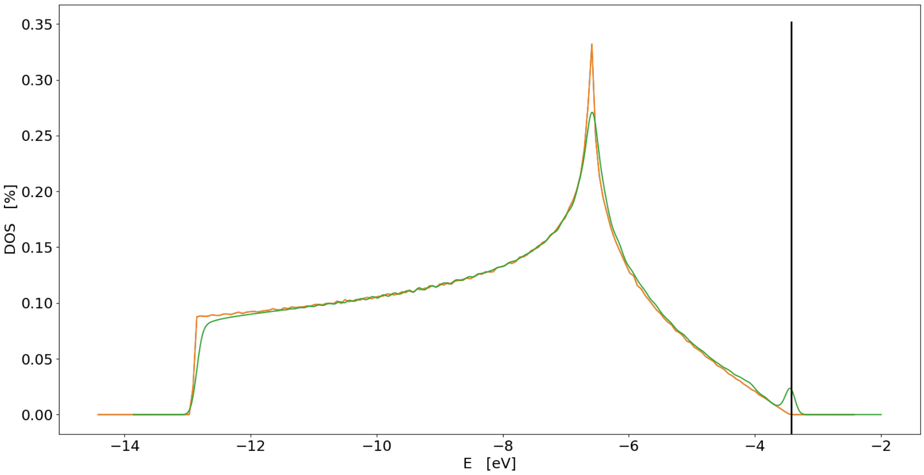

Figure 5.10: Density of states for the finite graphene cluster (green) and the ideal graphene (orange) with the dispersion given by Equation 2.70. The hopping parameter was chosen as $t = -3.15$ eV and the on-site energy $\epsilon = -3.42$ eV giving the Fermi edge (marked with black line).

This plot already gives a hint on the quality of the approximation to ideal graphene. It comes really close to the DOS of the periodic structure. The peak at the Fermi edge is an edge effect of the open borders of the molecule. To calculate the photoemssion intensity according to Equation 3.48, not just one eigenstate of the system, but several around the same energy have to be taken into account. To be precise, all momentum maps in an energy window of ±0.3 eV of the chosen energy of the DOS are summed up. So the photoemssion intensity is thus given by

$$I(\mathbf{k}) = \sum_i \omega(E_i)\left|\sum_n c_n^{E_i} e^{i\mathbf{k}\mathbf{R}_n}\left(\Lambda(\mathbf{k},\mathbf{A}) + (\mathbf{R}_n\cdot\mathbf{A})\mathcal{F}(\phi_n)(\mathbf{k})\right)\right|^2 \tag{5.11}$$

where $c_n^{E_i}$ is the eigenfunction of the Hückel matrix corresponding to the eigenvalue E_i and $\omega(E_i)$ is a weight factor. The weight factor is given by a Gauß function of the form

$$\omega(\epsilon_p) = \frac{1}{\sqrt{2\pi\sigma^2}} e^{-\frac{(E_b - E_i)^2}{2\sigma^2}} \tag{5.12}$$

Where E_b is the chosen constant binding energy. The shape of a Gauß function is motivated by the factor

$$\delta(\hbar\omega - E_i - \frac{\hbar^2 k^2}{2m} - \Phi) \tag{5.13}$$

in the general expression for the photocurrent of Equation 2.15. Choosing polarizations of $\mathbf{A} = [1, 0, 0]$ and $\mathbf{A} = [0, 1, 0]$ and including all states of ± 0.30 eV (by choosing $\sigma = 0.1$ eV) around the energy of $E_b = -4.92$ eV (-1.5 eV below Fermi edge) the result can be seen in Figure 5.11.

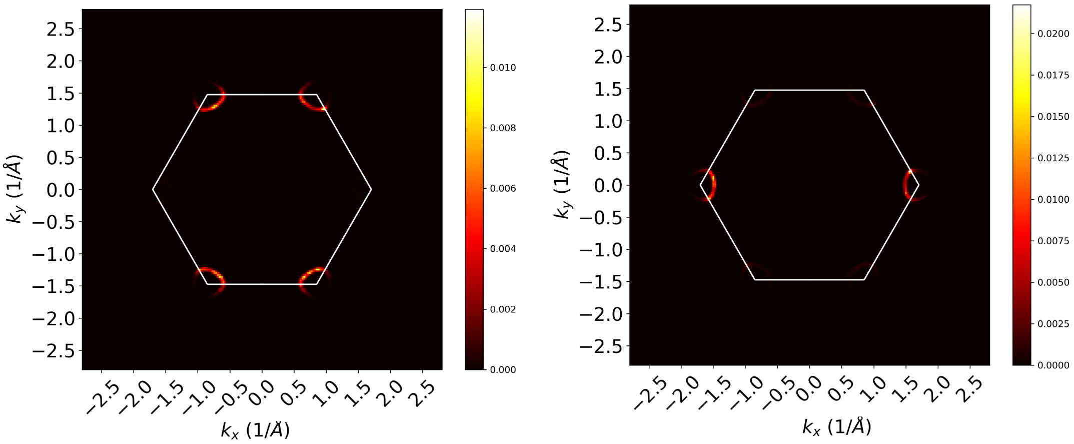

Figure 5.11: Constant binding energy momentum map for a binding energy of $E = -4.92$ eV, photoelectron energy of $E_{kin} = 30$ eV and a polarization of $\mathbf{A} = [1, 0, 0]$ (right panel) and $\mathbf{A} = [0, 1, 0]$ (left panel) of a finite graphene like molecule of 3658 atoms.

Note that the intensity here was evaluated for each k-point explicitly. Therefore no broadening of the k-space in order to smoothen the data has been applied. The convergence to the infinite extended graphene layer can be seen by a series of simulations with increasing size of the finite cluster.

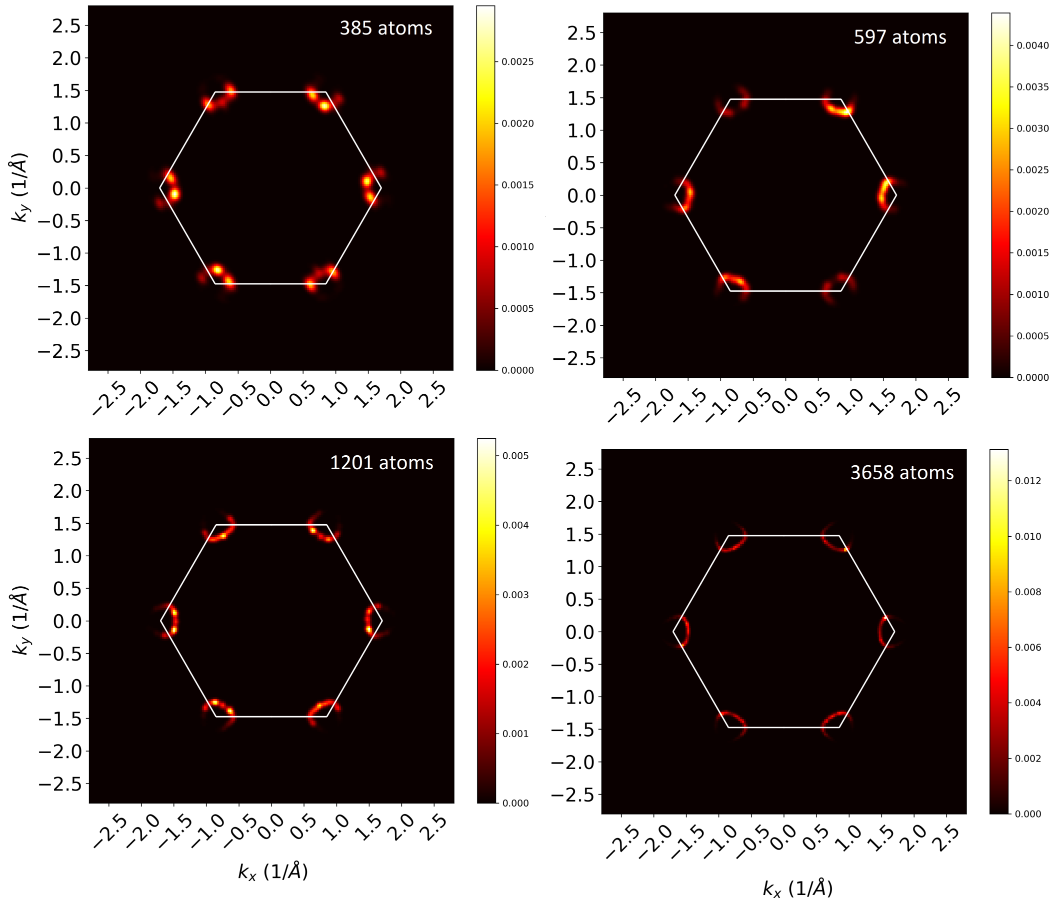

Figure 5.12: Constant binding energy momentum maps for a photoelectron energy of $E_{kin} = 30$ eV, a polarization of: $\mathbf{A} = [1, i, 0]$ and binding energy of -1.3 eV below the Fermi edge calculated with the LCAO method for 358, 835, 1444 and 3658 atoms sized clusters.

The constant binding energy momentum maps for linearly polarized light obtained within this finite cluster approximation compare relatively well to the chinook simulations of Section 4.3. For comparison both simulations are displayed for a polarization of $\mathbf{A} = [1, 0, 0]$ and a binding energy of -1.5 eV below the Fermi edge in Figure 5.13.

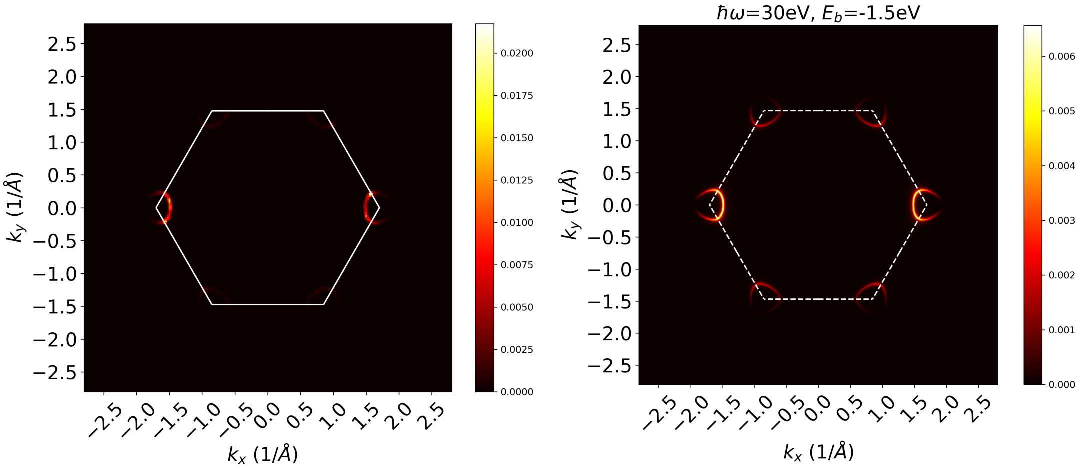

Figure 5.13: Constant binding energy momentum map for a photoelectron energy of $E_{kin} = 30$ eV and a polarization of $\mathbf{A} = [1, 0, 0]$ simulated with chinook (right panel) with a binding energy of -1.5 eV and with the LCAO method (left panel) for a cluster of 3658 atoms and a binding energy of $E = -4.92$ eV which is -1.5 eV below the Fermi edge.

The simulations for circularly polarized light of $\mathbf{A} = [1, i, 0]$ and $\mathbf{A} = [1, -i, 0]$ of the LCAO method leads to the result shown in Figure 5.14. The constant binding energy was set to -1.5 eV below the Fermi edge in order to make comparisons to the TDDFT simulations with circularly polarized light (shown in Figure 5.15) possible.

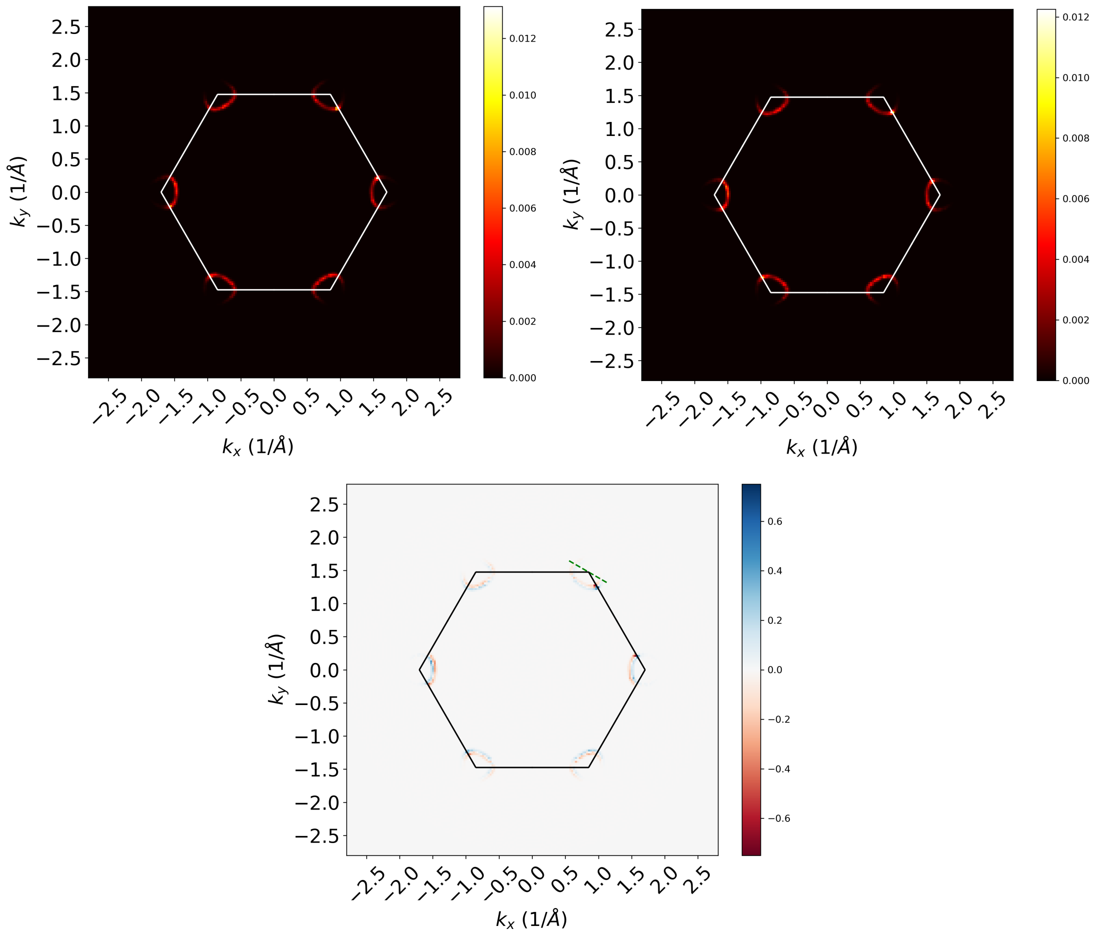

Figure 5.14: Constant binding energy momentum map for a binding energy of $E = -1.5$ eV below the Fermi edge, a photoelectron energy of $E_{kin} = 30$ eV and polarizations of $\mathbf{A} = [1, i, 0]$ (upper left panel) and $\mathbf{A} = [1, -i, 0]$ (upper right panel) as well as the CD map (lower panel) of a finite graphene like molecule of 3658 atoms.

The magnitude of the CD map was normed by

$$I_{CD} = \frac{I_R - I_L}{max(I_R)}. \tag{5.14}$$

This way the CD intensity map displays the absolute value of the CD effect. The differences of the CD effect in Figure 5.14 are at about 60 percent of the maximum of the two separated momentum maps. The CDAD effect is visible and can due to the noticeable intensity of the CD map not be interpreted as numerical noise.

Comparing this dichroism to the one obtained in the TDDFT simulations shown in Figure 5.15 one can see that, along the k-path marked with a green line in both Figure 5.14 and 5.15, they show no similarity. The Octopus calculations reveal an antisymmetric CDAD intensity distribution changing sign at the k-point while the intensity distribution of the dichroism map of the finite cluster changes sign multiple times along the k-path.

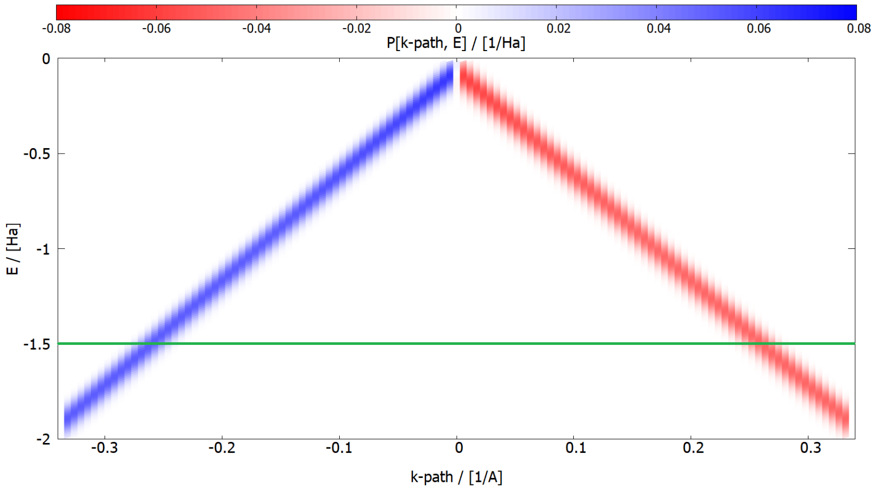

Figure 5.15: Circular dichroism intensity distribution of graphene simulated in the octopus code with a time interval of 50 fs, an intensity of $I = 1$ MW/cm^2 and $\omega = 30$ eV along $K_1 - K - K_2$ (shown in Figure 4.9) where $K = 0 \rightarrow k_{path} = 0$ for polarizations of $\mathbf{A}_{L/R} = [1, \pm i, 0]$. $P(\mathbf{k}, E)$ refers to the electron photoemission probability. The green line indicates the k-path at a constant binding energy of -1.5 eV.

As shown in Figure 5.12, the size of the finite cluster has a direct effect on the quality of the corresponding momentum map. It is possible that an antisymmetric behavior of the intensity distribution of the CD map is visible in the limit of an infinite cluster. It is also possible that the CDAD effect vanishes within this limit. Due to the similarity of the cone size and the DOS of the finite cluster of 3658 atoms to the ideal graphene, it is likely that the displayed CDAD of Figure 5.15 is also shown in the limit. Instead of further increasing the finite cluster size, using a Bloch wave ansatz would enable us to directly evaluate the CD map of the limit. Possibly this difficulty can be overcome by the use of the already discussed angular-momentum dependent phase factor.

One can include an angular-momentum dependent phase factor in the plane wave expansion as in Section 3.1.5 relatively easy in the Expression 5.11 by simply multiplying each of the radial integrals $R_l(k)$ with a corresponding phase factor $e^{-i\delta_l}$. This results in a change of the CDAD shown in Figure 5.15. In Section 3.1.5 the CDAD of a single $2p_z$ orbital was shown to be proportional to the factor

$\sin(\delta_0 - \delta_2)$. We will thus choose $\delta_0 = -\frac{\pi}{2}$ and $\delta_2 = \frac{\pi}{2}$ to maximize this factor. The corresponding constant binding energy momentum maps for $\mathbf{A} = [1, i, 0]$ and $\mathbf{A} = [1, -i, 0]$ polarizations are shown in Figure 5.16

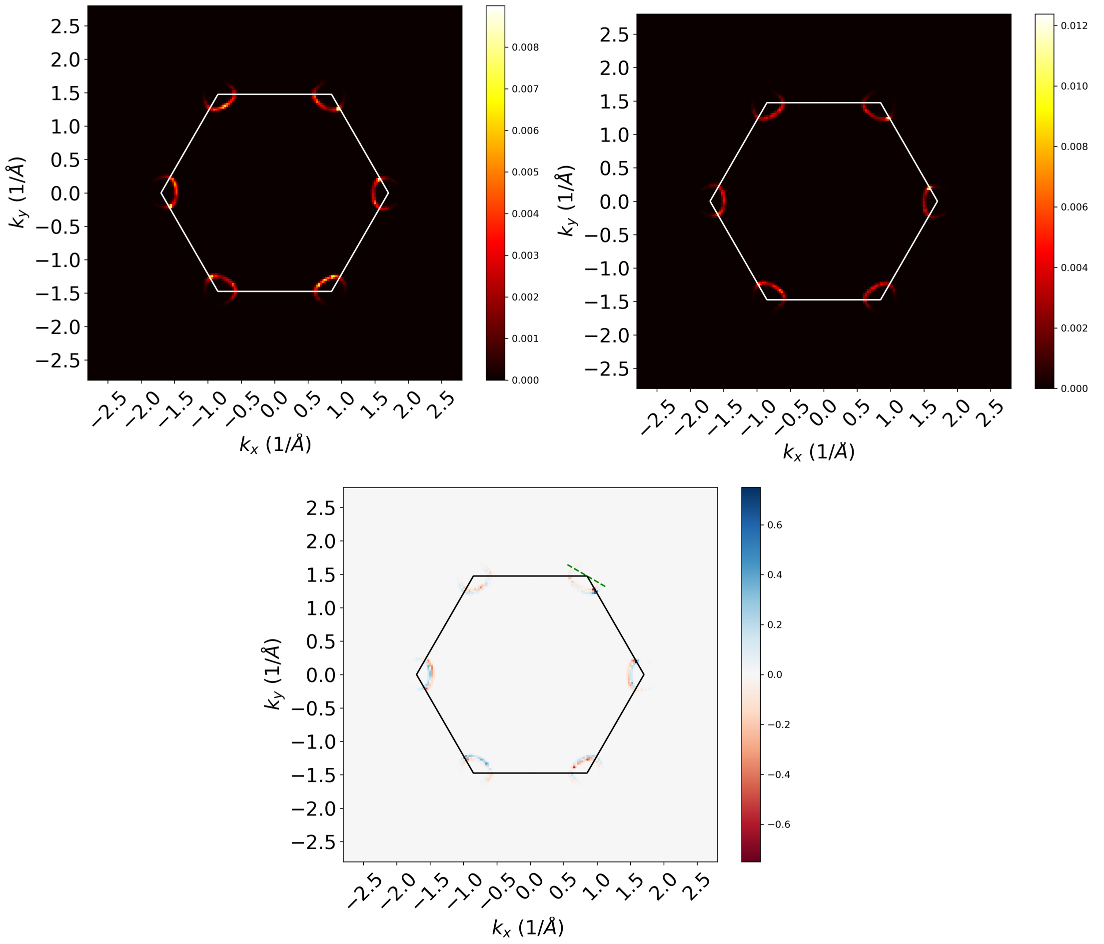

Figure 5.16: Constant binding energy momentum maps of a finite graphene like molecule of 3658 atoms. for constant energy of $E = -1.5eV$ below the Fermi edge for polarizations of $\mathbf{A} = [1, i, 0]$ (upper left panel), $\mathbf{A} = [1, -i, 0]$ (upper right panel) and the corresponding CD map (lower panel) with an included l-dependent phase factor as described above ($\delta_0 = -\pi/4, \delta_2 = \pi/4$). The photoelectron energy was set to 30 eV.

The simulated dichroism here has about the same magnitude as the one in Figure 5.14 without the l-dependent phase factor. When looking at the upper right K-point of the CD map (lower panel of Figure 5.16), one can actually see a change of the intensity distribution along the indicated k-path. It appears that the intensity difference has shifted more to the side of the left handed polarized photoemission. However there is no similarity to the CD intensity distribution of Figure 5.15. Also it is not possible to see a CDAD right away in the momentum maps of Figure 5.16. The octopus calculations of Section 4.4 using circularly polarized light shows a very strong CDAD around the K-points as can be seen in Figure 4.25. In the TDDFT simulations the CDAD can be seen directly and the intensity difference of the left and right handed polarized light is at about the same intensity as the intensity of each one of them. One can conclude that the the l-dependent phase factor does improve the quality of the ARPES simulation of circularly polarized light for graphene. These observations lead us to the conclusion.

6 Conclusion

In order to simulate ARPES intensities, the one-step model of photoemission is utilized which treats the photoexcitation from an initial state to a final unbound state, as a single coherent process. The associated photocurrent is proportional to the photo-emission matrix element given by Fermi's golden rule expression as

$$M(\mathbf{k}) = \langle \Psi_f \left| \mathbf{A} \cdot \mathbf{p} \right| \Psi_i \rangle . \tag{6.1}$$

Here, the final state is often approximated as a free electron and thus as a plane wave [2; 3].

Two seemingly equivalent ways of evaluating $M(\mathbf{k})$ are the velocity gauge and the length gauge. They both derive from Fermi's golden rule. By choosing a plane wave final state and inserting the position representation of the momentum operator, one obtains the velocity gauge

$$M_v(\mathbf{k}) = -i\hbar \left\langle e^{i\mathbf{kr}} \left| \mathbf{A} \cdot \nabla \right| \Psi_i \right\rangle . \tag{6.2}$$

The length gauge is then obtained by the use of the canonical commutation relation. By assuming $\left\langle e^{i\mathbf{kr}} \right|$ and $|\Psi_i\rangle$ to be eigenfunctions of the Hamilton operator with eigenvalues E_f and E_i, the length gauge expression of the matrix element can be expressed as

$$M_l(\mathbf{k}) = m(E_i - E_\mathrm{f}) \left\langle e^{i\mathbf{kr}} \left| \mathbf{A} \cdot \mathbf{r} \right| \Psi_i \right\rangle . \tag{6.3}$$

These expressions for the matrix element are evaluated further by specializing on planar hydrocarbons with sp^2 hybridization. Here, the initial state $|\Psi_i\rangle$ was assumed as molecular orbitals obtained by the Hückel model. The efficiency of this model makes the calculation of even very large molecules possible. Within this approximation, the molecular orbitals are constructed as a linear combination of atomic $2p_z$ orbitals of the carbon atoms. Due to the symmetry of the $2p_z$ orbital and the fact that the molecule is planar, the hopping parameter, giving the Hamilton matrix its form, is a function of the distance of the corresponding atomic $2p_z$ orbital only. By fitting the eigenvalues of the Hamilton matrix of the Hückel model of a given molecule to corresponding eigenvalues obtained by DFT calculations, the hopping parameter t was fitted as a quadratic polynomial function of the interatomic carbon-carbon distance r to

$$t(r) = -48.0r^2 + 146.7r - 114.7, \tag{6.4}$$

where t is given in eV and r is in Å. The standard deviation is given in Section 4.1.

Even though the Hückel model is quite simple and makes several crude approximations, the comparison to DFT calculations in Section 4.2 together with the reproduced density of states and the momentum maps in Section 5.3 show that it is indeed a justified choice as an initial state of the one-step model of photoemission.

As can be seen from Equation 6.1, the absolute value of the photoemission matrix element depends, not only on the initial and final state, but additionally on the polarization of the incident light beam. Further evaluating Equation 6.2, the polarization dependency of the photocurrent in the velocity gauge is proportional to

$$|M_v(\mathbf{k})|^2 \propto |\mathbf{A}\cdot\mathbf{k}|^2 \, |\mathcal{F}(\Psi_i)(\mathbf{k})|^2 \,. \tag{6.5}$$

On the other hand, the photoemission matrix element, evaluated in length gauge with a plane wave final state and choosing the initial state as a linear combination of $2p_z$ orbitals (following the Hückel approximation), can be expressed as

$$M(\mathbf{k}) = \sum_{n,\alpha} c_{n,\alpha} e^{i\mathbf{k}\mathbf{R}_n} \left(\Lambda(\mathbf{k},\mathbf{A}) + (\mathbf{R}_n\cdot\mathbf{A})\mathcal{F}(\phi_{n,\alpha})(\mathbf{k})\right). \tag{6.6}$$

Note that in the derivation of Equation 6.6 the Rayleigh expansion

$$e^{i\mathbf{k}\mathbf{r}} = 4\pi \sum_{l=0}^{\infty} \sum_{m=-l}^{l} i^l j_l(kr) Y^*_{lm}(\phi_k,\theta_k) Y_{lm}(\phi,\theta). \tag{6.7}$$

has been used, and that $\mathcal{F}(\phi_{n,\alpha})(\mathbf{k})$ in Equation 6.6 refers to the Fourier transformation of the $2p_z$ orbital. The term $\Lambda(\mathbf{k},\mathbf{A})$ is defined as follows

$$\Lambda(\mathbf{k},\mathbf{A}) = A_x\lambda_x(\mathbf{k}) + A_y\lambda_y(\mathbf{k}) + A_z\lambda_z(\mathbf{k}), \tag{6.8}$$

with

$$\lambda_x(\mathbf{k}) = -f_2(k)\sqrt{3\cdot 8\pi}\cos(\theta_k)\sin(\theta_k)\sin(\phi_k), \tag{6.9}$$

$$\lambda_y(\mathbf{k}) = -f_2(k)\sqrt{3\cdot 8\pi}\cos(\theta_k)\sin(\theta_k)\cos(\phi_k), \tag{6.10}$$

$$\lambda_z(\mathbf{k}) = \sqrt{4\pi}\left(f_0(k) - f_2(k)(3\cos^2(\theta_k) - 1)\right). \tag{6.11}$$

As shown in Section 3.2, the difference in the angular distribution of the photocurrent of the right and left handed circularly polarized light, called circular dichroism in the angular distribution (CDAD), vanishes for a plane wave final state in the velocity gauge. However, this is not the case for the length gauge expression in general.

To test this hypothesis, two types of simulations have been performed. First, we used the chinook [16] program where the length gauge is implemented in conjunction with a TB initial state. It was shown that simplifications, on the photoemssion matrix element, applied in chinook make it an inappropriate tool to further investigate CDAD effects, which is demonstrated for graphene.

Second, the photoemission intensity is evaluated with the help of Equation 6.6.

Here, for a tetracene molecule we find a non-vanishing CDAD effect. Thus, in contrast to the velocity gauge, the CDAD effect of the length gauge formalism of the photoemission matrix element with a plane wave final state does not vanish in general. The photoemission matrix element, simulated with Equation 6.6, shows for tetracene, in comparison to the experimental data from [4], reasonable results. Further investigations on how well Equation 6.6 together with the Hückel model simulates circular dichroism for molecules in general could possibly lead to a better understanding of the CDAD effect.

To make further progress, we have investigated how a simple modification of the final state modifies the result. To this end, we include an l-dependent phase factor in the final state, which modifies Equation 6.7 to

$$\Psi_f(\mathbf{r}, \mathbf{k}) = 4\pi \sum_{l=0}^{\infty} \sum_{m=-l}^{l} i^l j_l(kr) e^{-i\delta_l} Y_{lm}^*(\phi_k, \theta_k) Y_{lm}(\phi, \theta). \tag{6.12}$$

This is motivated by the fact that a vanishing CDAD effect of a single $2p_z$ orbital can be cured with such a phase factor [1].

In Section 5.3 the photoemission intensity distribution of single layer graphene was approximated by a large graphene like planar hydrocarbon molecule. Even though a CDAD effect was shown, comparisons to TDDFT calculations, performed with the octopus code, (see Section 4.4) show only few similarities.

The introduction of an angular momentum dependent phase factor in the final state as suggested by Schönhense in [1] does not provide a solution to this problem. A Hückel modeled large graphene like molecule is not an ideal framework to analyze this problem. In order to investigate this, a Bloch-wave initial state would provide a better model. Fully covering the CDAD effect in periodic systems may also be beyond the plane wave final state.

In Figure 5.4 it was shown that the linear dichroism effect of graphene near the K-point of the TDDFT result is slightly different to the one obtained within the one step model of photoemission. However in principle they shows the same properties. The predicted dependence of $|\mathbf{A} \cdot \mathbf{k}|^2$ is shown in the one-step model (in chinook as well as with the use of Equation 6.5). It is possible that the TDDFT simulation performed with the octopus code also shows this proportionality, but the electron photo-emission probability generally rises when approaching the K-point and thus the two effects cancel each other. Resembling this effect could possibly also go beyond the plane wave final state.

7 Appendix

Table 1: Molecules used for the fitting process described in Section 4.1.

Molecule	Short name	Chemical formula	Database index [28]
benzene	1P	C_6H_6	1
biphenyl	2P	$C_{12}H_{10}$	2
terhenyl	3P	$C_{18}H_{14}$	3
quaterphenyl	4P	$C_{24}H_{18}$	4
quinquephenyl	5P	$C_{30}H_{22}$	5
sexiphenyl	6P	$C_{36}H_{26}$	6
septiphenyl	7P	$C_{42}H_{30}$	7
naphthalene	2A	$C_{10}H_8$	8
anthracene	3A	$C_{14}H_{10}$	9
tetracene	4A	$C_{18}H_{12}$	10
pentacene	5A	$C_{22}H_{14}$	11
hexacene	6A	$C_{26}H_{16}$	12
heptacene	7A	$C_{30}H_{18}$	13
phenanthrene	3phenacene	$C_{14}H_{10}$	17
chrysene	5phenacene	$C_{18}H_{12}$	18
picene	4phenacene	$C_{22}H_{14}$	19
7phenacene	7phenacene	$C_{30}H_{18}$	21
bisanthene	bisanthene	$C_{28}H_{14}$	22
coronene	coronene	$C_{24}H_{12}$	23
hexabenzocoronene	hexabenzocoronene	$C_{42}H_{18}$	24
decapentaene	t-10A	$C_{10}H_{12}$	237
trans-12-acetylene	t-12A	$C_{12}H_{14}$	238
trans-14-acetylene	t-14A	$C_{14}H_{16}$	239
trans-16-acetylene	t-16A	$C_{16}H_{18}$	240
trans-18-acetylene	t-18A	$C_{18}H_{20}$	241
trans-20-acetylene	t-20A	$C_{20}H_{22}$	242
annulene-C18	annulene1	$C_{18}H_{18}$	287
annulene-C30	annulene2	$C_{30}H_{30}$	288
kekulene-equal	kekulene-equal	$C_{48}H_{24}$	289
annulene-C18-equal	annulene-inner	$C_{18}H_{18}$	290
annulene-C30-equal	annulene-outer	$C_{30}H_{30}$	291
kekulene-superaromatic	kekulene-super	$C_{48}H_{24}$	292
2P-1.38	2P-1.38	$C_{12}H_{10}$	312
2P-1.40	2P-1.40	$C_{12}H_{10}$	313
2P-1.42	2P-1.42	$C_{12}H_{10}$	314
2P-1.44	2P-1.44	$C_{12}H_{10}$	315
2P-1.46	2P-1.46	$C_{12}H_{10}$	316
2P-1.48	2P-1.48	$C_{12}H_{10}$	317
perylene	perylene	$C_{20}H_{12}$	266

References

[1] Gerd Schönhense. Circular dichroism and spin polarization in photoemission from adsorbates and non-magnetic solids. *Physica Scripta* **T31**, 255–275 (1990).

[2] Dominik Brandstetter, Xiaosheng Yang, Daniel Lüftner, F. Stefan Tautz, and Peter Puschnig. kmap.py: A python program for simulation and data analysis in photoemission tomography. *Comp. Phys. Commun.* **263**, 107905 (2021).

[3] C. Metzger, M. Graus, M. Grimm, G. Zamborlini, V. Feyer, M. Schwendt, D. Lüftner, P. Puschnig, A. Schöll, and F. Reinert. Plane-wave final state for photoemission from nonplanar molecules at a metal-organic interface. *Phys. Rev. B* **101**, 165421 (2020).

[4] Xiaosheng Yang, Larissa Egger, Jana Fuchsberger, Martin Unzog, Daniel Lüftner, Felix Hajek, Philipp Hurdax, Matteo Jugovac, Giovanni Zamborlini, Vitaliy Feyer, Georg Koller, Peter Puschnig, Frank Stefan Tautz, Michael G. Ramsey, and Serguei Soubatch. Coexisting charge states in a unary organic monolayer film on a metal. *The Journal of Physical Chemistry Letters* **10**, 6438–6445 (2019).

[5] P. Hohenberg and W. Kohn. Inhomogeneous electron gas. *Phys. Rev.* **136**, B864 (1964).

[6] P. J. Feibelman and D. E. Eastman. Photoemission spectroscopy - correspondence between quantum theory and experimental phenomenology. *Phys. Rev. B* **10**, 4932 (1974).

[7] Hückel E. Quantentheoretische Beiträge zum Benzolproblem. I. Die Elektronenkonfiguration des Benzols und verwandter Beziehungen. *Zeitschrift für Physik* **70**, 204–286 (1931).

[8] P. A. M. Dirac. The quantum theory of the emission and absorption of radiation. *Royal Society* **114**, 767 (1927).

[9] Daniel Lüfter. Orbital tomography: Understanding photoemission of organic molecular films. *PhD thesis, University of Graz* (2015).

[10] P. Puschnig and M.G. Ramsey. Photoemission tomography: Valence band photoemission as a quantitative method for investigating molecular films. *Encyclopedia of Interfacial Chemistry, Elsevier* , 380 – 391 (2018).

[11] F. Bloch. Über die Quantenmechanik der Elektronen in Kristallgittern. *Z. Phys.* **12**, 47–88 (1928).

[12] Tancogne-Dejean N , M. J. T. Oliveira and X. Andrade, H. Appel , C. H. Borca , G. Le Breton , F. Buchholz , A. Castro , S. Corni , A. A. Correa ,

U. De Giovannini , A. Delgado , F. G. Eich , J. Flick , G. Gil , A. Gomez , N. Helbig , H. Hubener , R. Jestädt , J. Jornet-Somoza , A. H. Larsen , I. V. Lebedeva , M. Luders, M. A. L. Marques, S. T. Ohlmann , S. Pipolo , M. Rampp , C. A. Rozzi , D. A. Strubbe , S. A. Sato , C. Schafer , I. Theophilou , A. Welden, A. Rubio. Octopus, a computational framework for exploring light-driven phenomena and quantum dynamics in extended and finite systems. *The Journal of Chemical Physics* **152**, 124119 (2020).

[13] Jinying Wang, Shibin Deng, Zhongfan Liu and Zhirong Liu. The Rare Two-Dimensional Materials with Dirac Cones. *National Science Review* **2**, 22–39 (2015).

[14] Simon Moser. An experimentalist's guide to the matrix element in angle resolved photoemission. *Journal of Electron Spectroscopy and Related Phenomena* **214**, 29–52 (2017).

[15] Per-Olov Löwdin. On the non-orthogonality problem connected with the use of atomic wave functions in the theory of molecules and crystals. *The Journal of Chemical Physics* **18**, 365 (1949).

[16] R. P. Day, B. Zwartsenberg, I. S. Elfimov, and A. Damascelli. Computational framework chinook for angle-resolved photoemission spectroscopy. *npj Quantum Materials* **4**, 54 (2019).

[17] Anthony T. Paxton. *An Introduction to the Tight Binding Approximation* volume 42. John von Neumann Institute for Computing Jülich, Contribution to a book: Multiscale Simulation Methods in Molecular Sciences, NIC Series **42**, 145–176 (2009).

[18] J. C. Slater and G. F. Koster. Simplified LCAO method for the periodic potential problem. *Phys. Rev.* **94**, 1498 (1954).

[19] Roald Hoffmann. An Extended Hückel Theory. I. Hydrocarbons. *J. Chem. Phys.* **39**, 1397 (1963).

[20] D A Papaconstantopoulos and M J Mehl. The Slater Koster tight-binding method: a computationally efficient and accurate approach. *Journal of Physics: Condensed Matter* **15**, R413 (2003).

[21] D. S. Sholl and J. A. Steckel. *Density Functional Theory: A Practical Introduction.* Wiley (2009).

[22] M. Born and R. Oppenheimer. Zur Quantentheorie der Moleküle. *Ann. Physik* **84**, 457 (1927).

[23] Eberhard K. U. Gross and Neepa T. Maitra. *Introduction to TDDFT, Chapter 4.* Springer-Verlag Berlin Heidelberg (2012).

[24] E. Runge and E. K. U. Gross. Density-functional theory for time-dependent systems. *Phys. Rev. Lett.* **52**, 997 (1984).

[25] Umberto De Giovannini, Hannes Hübener, and Angel Rubio. A first-principles time-dependent density functional theory framework for spin and time-resolved angular-resolved photoelectron spectroscopy in periodic systems. *J. Chem. Theory Comput.* **13**, 265–273 (2017).

[26] Kevin Cahill. *Expansion of plane waves in spherical harmonics, from Physical Mathematics.* Cambridge University Press (2013).

[27] Ask Hjorth Larsen, Jens Jorgen Mortensen, Jakob Blomqvist, Ivano E Castelli, Rune Christensen, Marcin Dulak, Jesper Friis, Michael N Groves, Bjork Hammer, Cory Hargus, Eric D Hermes, Paul C Jennings, Peter Bjerre Jensen, James Kermode, John R Kitchin, Esben Leonhard Kolsbjerg, Joseph Kubal, Kristen Kaasbjerg, Steen Lysgaard, Jon Bergmann Maronsson, Tristan Maxson, Thomas Olsen, Lars Pastewka, Andrew Peterson, Carsten Rostgaard, Jakob Schiotz, Ole Schütt, Mikkel Strange, Kristian S Thygesen, Tejs Vegge, Lasse Vilhelmsen, Michael Walter, Zhenhua Zeng, and Karsten W Jacobsen. The atomic simulation environment - a python library for working with atoms. *Journal of Physics: Condensed Matter* **29**, 273002 (2017).

[28] *Organic Molecule Database, url: https://homepage.uni-graz.at/de/peter.puschnig/research/online-databases/.* .

[29] Koichi Momma and Fujio Izumi. Vesta: a three-dimensional visualization system for electronic and structural analysis. *Journal of Applied Crystallography* **41**, 653–658 (2008).